The Role of Strain in the Surface Structures of III-V Alloyed Semiconductor Films

by

Jessica E. Bickel

A dissertation submitted in partial fulfillment
of the requirements for the degree of
Doctor of Philosophy
(Materials Science and Engineering)
in The University of Michigan
2010

Doctoral Committee:

Associate Professor Joanna Mirecki-Millunchick, Chair
Associate Professor Jamie D. Phillips
Assistant Professor Anton Van der Ven
Associate Professor Christopher A. Pearson, University of Michigan-Flint
Normand A. Modine, Sandia National Laboratories

Acknowledgements

I would like to thank all of the people who have guided me over the years and helped me to reach this point. First and foremost, I must thank my advisor, Joanna Mirecki Millunchick, who asked me to take on a project that I was not sure I wanted (and had already turned down twice), but which, ultimately, allowed me to grow and to spread my wings scientifically in a way I could not have foreseen. I also want to thank her for her time and patience, her willingness to take "pedagogical moments," her interest in outreach and teaching young girls about the "Materials Science of Food," and for reminding me to leave the lab and have a cup of tea when things go wrong because it will be better when you come back. I would also like to thank my labmates for their friendship, their knowledge and their willingness to teach me, to be taught by me, and to learn with me. Thank you to Anton Van der Ven for his patience and willingness to answer silly questions (that may or may not have been answered already…), for helping me learn how to bring things back to the fundamental thermodynamics even when I did not always see the connection, and for his willingness to learn about semiconductors while I learned about DFT. Thank you to Normand Modine, for his willingness to teach me all he knows about computation, semiconductors, and bonding, topics about which he carries a wealth of knowledge; and thank you for random discussions at conferences, support at talks, and for being a friend. Thank you to Chris Pearson for teaching me how to grow a sample on the MBE, how to STM, and for all the times he was able to help me out over the telephone when the STM was acting up again. And thanks also to Jamie Phillips, my final committee member, who made me think and ponder the forks in the road when he asked questions at my first presentation in

graduate school. I also want to thank Jonah Erlebacher, for his time and patience with a young undergraduate, both in the classroom and in the lab, and for his guidance and knowledge. Thank you to Joseph Turner, for supporting an oboist who also enjoyed playing in the laboratory. And thanks also to Jim Voigt and Diana Moore, who gave me my first laboratory experience as an intern at SNL, who taught me so much over the four years I worked with them, and who still support me today.

I also want to thank my family and friends. Thank you to my friends, who put up with my craziness when I get stressed and who support me wherever I am and wherever I go. Thank you to my sisters whom I love, and who always make me smile. And of course, thank you to my parents who have always supported me, whatever path I choose to follow. Thank you for the late night paper critiques and the elementary school science projects. Who would have thought that building a "calculator" in third grade would lead to a PhD in Materials Science?

Table of Contents

List of Figures

Abstract

As length scales continue to decrease, it is vital to understand the fundamental physical parameters governing surfaces and surface interactions. In semiconductors particularly, surface reconstructions are known to impact film growth, bulk atomic ordering and the development of interfacial structure, all of which can drastically impact device growth. While the parameters that determine surface reconstructions in homoepitaxially grown films are well known and understood, those that impact alloy film growth are less studied. This work examines the impact of strain on alloy surface reconstructions, using the III-V semiconductors as a model system for any covalently bonded crystal structure. The presence of surface reconstruction *coexistence* in both mixed cation and mixed anion systems suggests that localized strain fields on alloy surfaces stabilize elastic relaxation at boundaries, resulting in more complex surface structures than those seen on binary, unstrained films. Atomic size mismatch strain is shown to induce an ordering in alloyed surface reconstructions that is not seen in the non-alloyed constituent surfaces. Lattice mismatch strain is shown to both stabilize new reconstructions not common to the homoepitaxial system and to induce surface reconstruction coexistence on alloy surfaces. The supplied flux of material is shown to affect the kinetics of transformation between the two coexisting surface reconstructions and an incorporation model for material on the alloy surface is developed. The effects of strained surface reconstructions on subsequent film growth is explored and it is shown that identical films grown on two different surfaces have very different strain relaxation profiles, surface topographies and defect structures. The strain fields of surface reconstructions and defects are also shown to interact which may have an impact on the insertion of dislocations in these films. Combined together, this deep understanding of the role that alloy induced strain plays in surface reconstructions will lead to a more complete understanding of the properties

which govern reconstructions in general, and also create the possibility of engineering specific reconstructions which will form more abrupt interfaces, inject specific types of defects, or act as surfaces for subsequent self-assembly.

Chapter I

Introduction and Background

As the length scale of devices continues to decrease, it becomes increasingly important to understand the fundamental physics governing nanoscale interactions. As size decreases, the ratio of surface area to volume increases, meaning that *surface energy* and *surface structure* play an increasingly large role in determining material properties such as magnetism [1] or in governing interactions between non-adjacent layers in multi-layer nm thick films that affect wetting [2].

Surfaces are relatively high energy structures compared to bulk atomic crystals. This is due to the high number of unsaturated bonds on the surface resulting from the interface between the surface and air. In many crystals, surface reconstructions develop where atoms either rearrange on the surface or relax inward towards the bulk in order to lower the surface energy. The resulting pattern is the lowest energy surface configuration and is repeated periodically across the crystal surface. Surface reconstructions are important because they can greatly affect material properties such as catalysis [3] and magnetic domain orientation [4] and they also affect film growth inducing atomic bulk ordering [5] and impacting interfacial abruptness [6]. Surface reconstructions are seen in many different materials systems including metals, but they are particularly prominent in covalently bonded materials such as semiconductors.

Semiconductors are of great technological importance and are being used in lasers, LEDs, RFIDs, computing, and a plethora of other applications. The III-V semiconductors are particularly useful due to the ability to "tune" their bandgaps for specific applications by alloying with another III-V material. In this way a wide variety of bandgaps are accessible for device applications. As the length scales of these devices are continually reduced, it is increasingly necessary that the semiconducting layers be defect free and exhibit abrupt interfaces. These factors can be greatly impacted by strain within the system which may induced by alloying, including lattice mismatch strain which results from the difference in lattice parameters between a chosen substrate and a film or between two subsequent film layers, and atomic size mismatch strain which occurs due to size differences between atomic species during alloyed film growth.

Strain and surface reconstructions are both known to impact epitaxial thin film growth [7] [8]. Strain may also impact the creation of dislocations [9], and interfacial development [5] in the semiconductor system, while surface reconstructions are also known to impact interfacial abruptness [6], atomic bulk ordering [5], and self assembly at the micro- and nanoscales [10]. However, while both of these effects are important in semiconductor film growth, the resulting effect of strain on the surface reconstructions of these materials is not well understood.

This dissertation examines the impact of global lattice mismatch strain and point atomic size mismatch strain on the surface reconstructions of III-V semiconductor alloys. The III-V semiconductors are chosen both as a materials system of technological importance and as a model system for other covalently bonded, alloyed systems. The impacts of strained surface reconstructions on the incorporation of defects and the subsequent film growth are also examined. Understanding the fundamental physical factors governing surface reconstructions and how these reconstructions alter atomic incorporation on the surface and impact subsequent film growth is an important step towards designing better devices with sharper interfaces. This knowledge has the potential to lead to new self-assembly pathways for complex nanostructure development.

i. Model System: III-V Semiconductors

Semiconductors are important technologically because of the bandgap between electronic states that determines their electronic properties. These properties are exploited in applications such as lasers, light emitting diodes (LEDs), and solar cells. Si is an intrinsic semiconductor from Group IV of the periodic table and is the most commonly used semiconductor because it is relatively cheap to produce and process. However, the applications Si can be used for are limited due to the inability to alter the bandgap and the fact that the bandgap is indirect.

The III-V semiconductors are composed of elements from Groups III and V on the periodic table and are typically more expensive to produce, but they are used for a number of different applications due to the ability to "tune" the bandgap to a particular desired wavelength. Bulk III-V semiconductors, with the exception of Bi and N, form a Zinc Blende structure that consists of two interpenetrating FCC unit cells, as is seen in Figure 1.1. These two interpenetrating FCC cells form two sublattices in the Zinc Blende crystal structure, one of the Group III cations and one of the Group V anions. This class of materials has the same crystal structure across a variety of compositions. This makes it an ideal material system to examine the effects of alloying on surface structure because changes in alloying will not change the bulk crystal structure. This is important because changes in the bulk structure would impart drastic changes on the surface structure due not to strain but to structural changes. These materials are also ideal because the effects of mixed cation and mixed anion alloying can be studied independently due to the two sublattices.

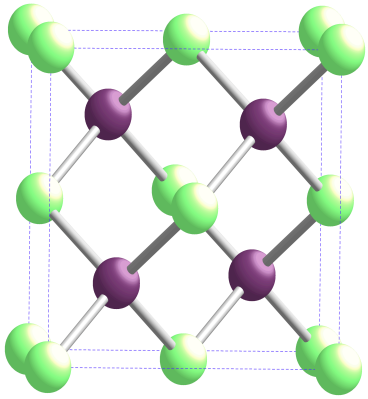

***Figure 1.1**: Zinc Blende structure with two distinct FCC sublattices.*

The range of distinct bandgaps which are accessible for III-V ternary alloys is shown in Fig. 1.2. When an alloy is formed of two of the III-V binary compounds, the bandgap of the alloy changes according to the tie-lines on the graph. However, as the bandgap is altered, the lattice constant of the material is also altered, which may result in the introduction of strain into the material.

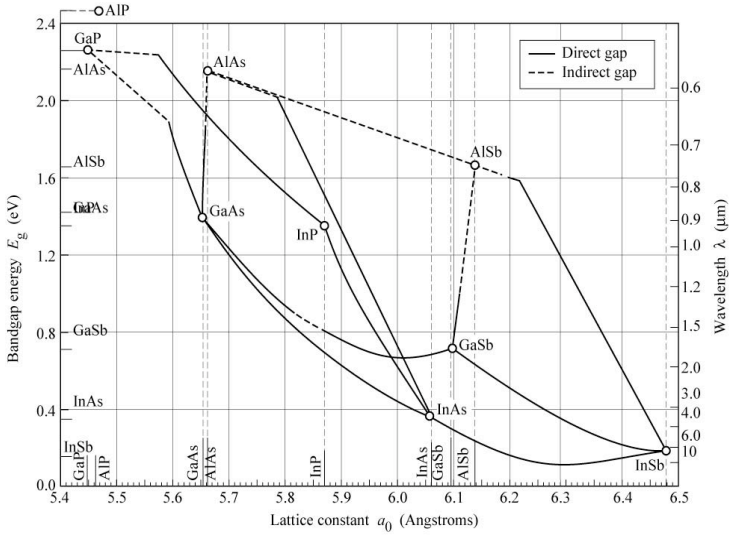

Figure 1.2: Bandgap vs. Lattice parameter diagram [11].

ii. Alloy Induced Strain in Thin Films

Thin films do not exist by themselves, but instead are grown on substrates and integrated into multi-layer devices. Unfortunately, there are not an infinite number of substrates with an infinite number of lattice parameters available for growth. Even if this were the case, sometimes the device itself dictates the necessity of a particular substrate – for example an insulating substrate or a Si

substrate for lithographic processing steps. This means that while it is possible to engineer a wide variety of band gaps, as was seen in Fig. 1.4, it is typically not possible to avoid the introduction of strain into the material.

Lattice mismatch strain is well known in the thin film industry because it drastically impacts film growth, not only for semiconductors but also for metal films, oxides, and polymers. Lattice mismatch strain is due to the difference in lattice parameter between the substrate and the deposited film and can be described by:

$$f = \frac{a_s - a_f}{a_s} \tag{1.1}$$

where f is the misfit strain, and a_s and a_f are the substrate and film lattice parameters, respectively. Strain within the film increases the energy of the system and must be released when it reaches some critical value. Typically this is done in one of two ways: (1) a change from two dimensional to three dimensional growth and surface roughening, or (2) through the insertion of dislocations as is seen in Fig. 1.3.

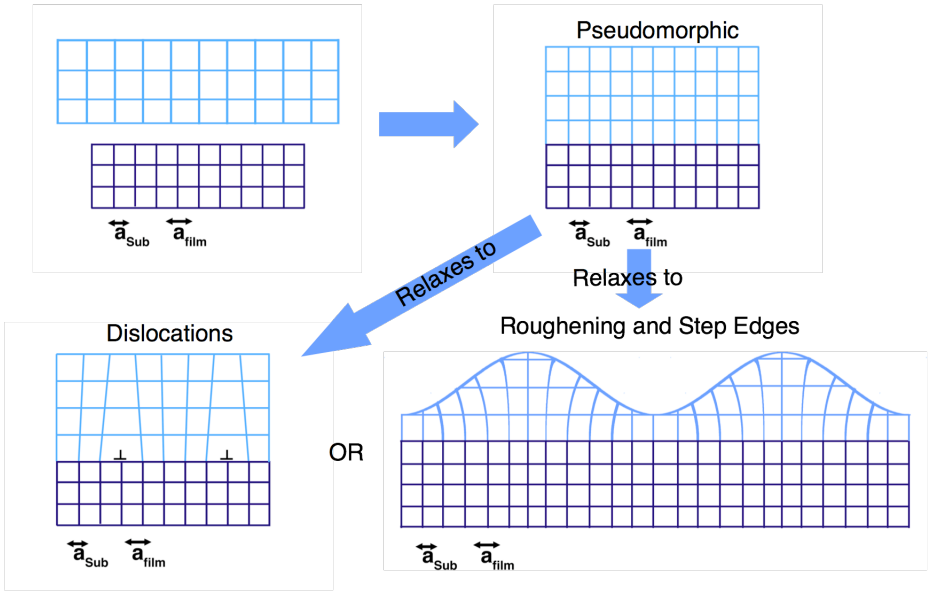

***Figure 1.3**: Schematic of lattice mismatch strain. A film with lattice parameter $a_{film}>a_{substrate}$ is grown on a substrate. The film can either be pseudomorphic, or relax through dislocations or surface roughening.*

There are three growth modes for epitaxially grown films: (1) layer-by-layer growth, (2) Volmer-Weber (VW) growth [7], and (3) Stranski-Krastinov (SK) growth [7]. The first case occurs typically in homoepitaxy or in cases of

lattice-matched or low lattice mismatch systems. This is ideal because the film is either unstrained or is only slightly strained and can grow pseudomorphically. In pseudomorphic growth, the in-plane lattice parameter of the film strains to match that of the substrate, and the out of plane lattice parameter deforms slightly according to Poisson's ratio. In this case, the film grows flat with no introduction of defects which may degrade device properties. In VW growth there is no pseudomorphic 2D film growth. Instead the material immediately forms 3D islands on the surface as seen in Fig. 1.4. VW growth occurs for highly lattice mismatched materials. SK growth is the most interesting growth mode and one of the most common in III-V material growth. In this case, the film begins growing pseudomorphically. However, due to the lattice mismatch, the strain energy of the system increases with the incorporation of additional material into the film. When the energy of the system reaches a critical value at some critical thickness, h_c, the film growth transitions from 2D to 3D growth, resulting in a film with 3D islands on a 2D wetting layer as seen in Fig. 1.4.

***Figure 1.4**: Schematic of VW (left) and SK (right) growth modes.*

The critical thickness of these films is related to the amount of lattice mismatch between the film and substrate [12]. However, the relation is not simple, as the energy to introduce and move dislocations can also impact the critical thickness [13]. In both VW and SK growth the strain is relieved through a combination of 3D growth and the insertion of dislocations. Sometimes this is ideal, such as the growth of 3D islands for quantum dot applications or the introduction of misfit dislocations at the device interface, which relieves strain without propagating through the film. However, typically the introduction of film roughness and dislocations is deleterious for device properties. Often, dislocations are threading dislocations that propagate through the film and act as non-radiative recombination points, which greatly decrease the efficiency of the device. The lattice mismatch strain can be mitigated through specific growth techniques. One such technique is the use of graded buffer layers where the composition of a buffer layer is slowly altered during growth resulting in a film

that changes composition and lattice parameter slowly through its thickness. This can reduce the number of dislocations in the film; however, it does not get rid of them entirely [14].

Lattice mismatch strain is not always deleterious to semiconductor electronic devices. In fact, strain may be used to alter the band structure of a semiconductor. The curvature of the band structure at Γ, the origin of the crystal, is related to the effective mass of the holes (valence band) and electrons (conduction band). The effective mass is related to the energy of a charge carrier in a particular band and impacts the ability of the charge carrier to conduct. Typical band diagrams have a single curve for the conduction band and two curves which are degenerate at Γ in the valence band. When a biaxial stress is applied, there is some change in the shape of the conduction curve [15]. This shape change also causes a shift in the bandedge. However, there is a much more drastic change in the valence curve, as is shown in Fig. 1.5. When a biaxial strain is applied, the degeneracy in the valence band disappears, resulting in a splitting of the "heavy" and "light" hole curves. This is important because it changes the effective mass of the holes populating the band and can lead to a drastic change in the density of states that may be exploited for lasing devices [15].

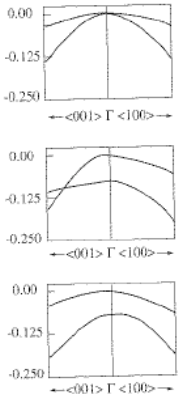

***Figure 1.5**: Valance band images for unstrained GaAs, 1% tensile biaxially strained GaAs, and 1% compressively strained GaAs. Taken from [15].*

Alloying in compound semiconductors may also induce a second type of strain due to distortion within the sublattices. Alloying the cation or anion species may result in a point strain, known as atomic size mismatch strain, due to the different size of the atoms on the respective sublattice. Atomic size mismatch

strain is well known within metals. In this case, an atom of type B is placed in a lattice of atoms of type A. If there is a size difference between atoms A and B, a compressive or tensile strain is projected into the lattice within a fixed radius, as is seen in Fig. 1.6. This type of strain has not been explored with respect to semiconductors before. However, the strained nature of the surface reconstruction suggests that this type of strain may be important in determining surface alloying.

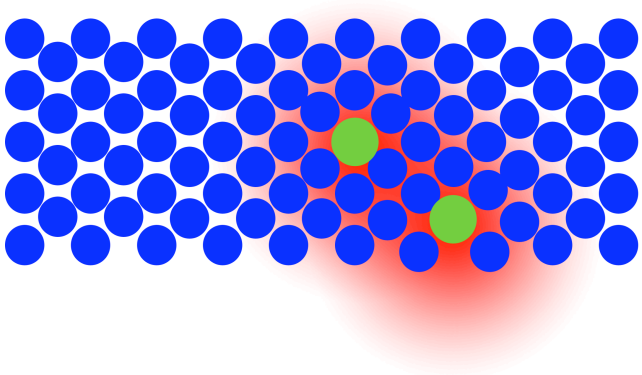

***Figure 1.6**: Schematic of atomic size mismatch strain. Atoms of Element B are 7% larger than those of Element A, resulting in a strain field when they are substitutionally added to the lattice.*

iii. Surface Reconstructions

Surface reconstructions are seen in a multitude of materials systems including metals, oxides, and semiconductors. Some well-known examples are the herringbone reconstructions Au-(111) [16] and the Si-(7x7) reconstruction [17]. As stated earlier, surface reconstructions form in order to lower the surface energy, resulting from the high number of unsaturated bonds that exist when a surface is cleaved. A schematic of the unsaturated bonds is shown in Fig. 1.7 (top). The resulting pattern repeats periodically across the surface and is named according to its periodicity (nxm) where n and m are the number of bulk spacing along crystallographic directions. An example of a GaAs-β2(2x4) reconstruction is shown in Fig. 1.7 (bottom). The β2 term simply refers to a specific GaAs-(2x4) reconstruction. In this case, and for all III-V-(001) surfaces, n and m are the $[1\bar{1}0]$ and [110] directions, respectively. Surface reconstructions can be characterized using scanning tunneling microscopy (STM) to image the repeating unit cells. An STM image of the β2(2x4) surface is shown in Figure 1.8. The straight rows in

this image are the surface As-As bonds, or dimers, which appear in the β2(2x4) reconstruction.

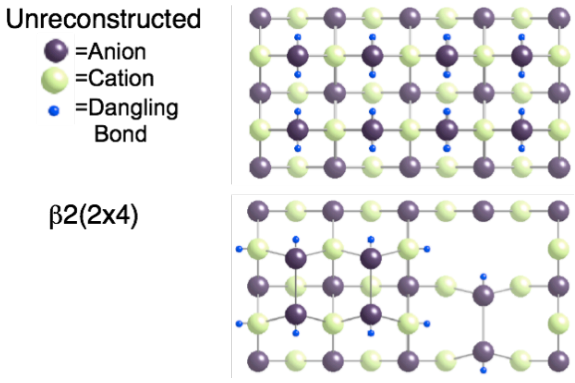

***Figure 1.7**: Unreconstructed and β2(2x4) reconstructed surface. Anion = As, Cation = Ga. Horizontal = [110], Vertical = [1 $\bar{1}$ 0].*

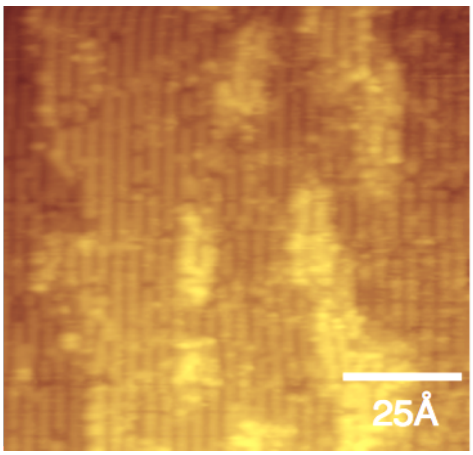

***Figure 1.8**: STM image of a GaAs β2(2x4) surface. Horizontal = [110], Vertical = [1 $\bar{1}$ 0].*

In metals, surface reconstructions are typically the result of the surface atoms relaxing inwards towards the bulk material due to the fact that there are no atoms above the surface to exert force in the opposite direction [18]. This relaxation inward is often about 5% of the bulk lattice parameter and affects the top two layers of atoms [19]. As such, these unit cells are often small and can even be simple (1x1) reconstructions. However, this is not always true, as is evidenced by the Au-(111) herringbone reconstruction. In this case, the surface forms a mixed HCP-FCC packing due to the influence of the interatomic potentials forcing different bondlengths on the surface [20]. Surface adsorbates also form surface reconstructions which are often driven by the competing interactions of the adsorbates with the surface and each other. This

chemisorption can drive the metallic atoms to reconstruct, changing their height relative to the surface normal and forming local maxima and minima, creating a somewhat larger unit cell [19]. One such example is $CH_3C/Rh(110)$, which forms a (2x2) reconstruction [19]. Ionic solids also reconstruct with the cations and anions appearing to lie at slightly different heights [19].

In each of the above cases, the periodicity is driven predominately by atomic packing because ionic and metallic bonds are not directional. Covalently bonded systems, such as the III-V semiconductors, exhibit a vast variety of surface reconstructions due to the directionality of the hybridized atomic orbitals which require directionalized dimerization of atoms on the surface. One example of a III-V surface reconstruction is the GaAs-β2(2x4) reconstruction shown in Fig. 1.7. In this case, the directionality of bonding controls the direction of the surface As-As dimer bond, and the chemistry of the system results in an As rich surface. Generally, the stable reconstruction of a homoepitaxially grown binary semiconductors is determined by competition between three competing interactions: (1) the reduction in chemical energy due to the formation of new covalent bonds, (2) the electrostatic energy associated with the rearrangement of electrons within the atomic bonds and dangling bonds of the surface, and (3) the strain energy introduced by displacing atoms from their bulk lattice positions. The second point requires that the surface remain charge neutral as is dictated by the Electron Counting Rule (ECR). For this to occur, the anion dangling bonds are filled with two electrons, while cation dangling bonds are empty [21]. Surface reconstructions for GaAs [22], InAs [23], and GaSb [24] have been determined experimentally through the use of reflection high energy electron diffraction (RHEED) and *in situ* STM. These surfaces exhibit a single reconstruction across the entire surface of the semiconductor that changes as a function of chemical potential, μ, where μ is a function of material flux and growth temperature. *Ab initio* calculations based on density functional theory (DFT) capture the principal factors influencing reconstruction stability in these systems and have reproduced the experimentally observed sequence of reconstructions with varying chemical potential for the GaAs [25], InAs [23], and GaSb [26] (001) surfaces.

Yet, while the binary semiconductor systems are well understood, the surface structures of ternary, alloyed structures are less well known. Some particular questions remain. Specifically:

- What are the roles of chemistry, lattice mismatch strain and atomic size mismatch strain in determining the stability, and structure of alloyed surface reconstructions?
- What roles do alloyed surface reconstructions play in subsequent film growth?

While this dissertation focuses on the III-V semiconductor system, these questions are applicable to any alloy surface which exhibits a surface reconstruction.

iv. Impacts of Strain on Surface reconstructions

Surface reconstructions are known to have inherent stress fields due to the displacement of atoms from their bulk atomic positions which create localized points of compressive and tensile strain in and just below the surface as bonds are stretched in order to accommodate surface atomic movement. The effect of surface reconstructions on bulk ordering has examined this. In GaInP, local strain due to the surface reconstruction has been shown to induce preferential placement of the cations just below the surface, resulting in bulk CuPt-type ordering [5, 27]. However, the impact of strain on the surface reconstructions of alloys remains relatively unstudied.

Cantilever experiments are a good way to measure the amount of strain in a thin film because the amount of cantilever deflection is directly related to the amount of strain in the film. Some work has been done to examine surface reconstruction strain using this method, though this work has been limited to metal reconstructions. One example is the examination of O_2 adsorption onto a clean Cu(001). At low temperatures, this surface exhibits a c(2x2)-O reconstruction. At high temperatures the reconstruction changes to a missing row $(\sqrt{2} \times 2\sqrt{2})R45°$ reconstruction [28]. The structure of the reconstruction depends on O adsorption, which breaks surface bonds and forms new bonds between the Cu and O. The two resulting reconstructions have very different

structures and exhibit very different strain fields. The amount missing row reconstruction exhibits less stress [28], presumably due to the ability of the missing row to relieve compressive strain.

In the III-V semiconductor system there is one study on the effect of lattice mismatch strain on the stability of surface reconstructions. However, this is a computational study which has not been paired with experimental evidence. Figure 1.9 shows the effect of straining InAs in both compression and tension. The x-axis describes chemical potential of As relative to its bulk value, $\mu_{As}-\mu_{As(bulk)}$, with right being an As-rich environment and left being an As-poor environment. The y-axis describes energy, with the lowest curve representing the stable reconstruction for a given μ_{As}. This graph shows the expected stability for InAs at the InAs lattice parameter, with the β2(4x2) stable for Ga rich environments and the α2(2x4) and β2(2x4) stable for increasingly As rich environments. This work also highlights the anisotropic effect of strain due to the anisotropy of the surface reconstruction. The orientation of surface dimers has a dramatic impact on the relief of strain along different crystallographic direction, as does the relative tensile or compressive nature of the bonds themselves [29]. As most surface dimers are under tensile strain, compressive strain often stabilizes these surface dimers by relieving strain energy. However, it is not possible to strain pure InAs, and thin films of InAs/GaAs form a (4x3) reconstruction that is unique to the alloy system [30], so while this work is very suggestive of the role lattice mismatch strain may play in the stability of surface reconstructions, it is not conclusive.

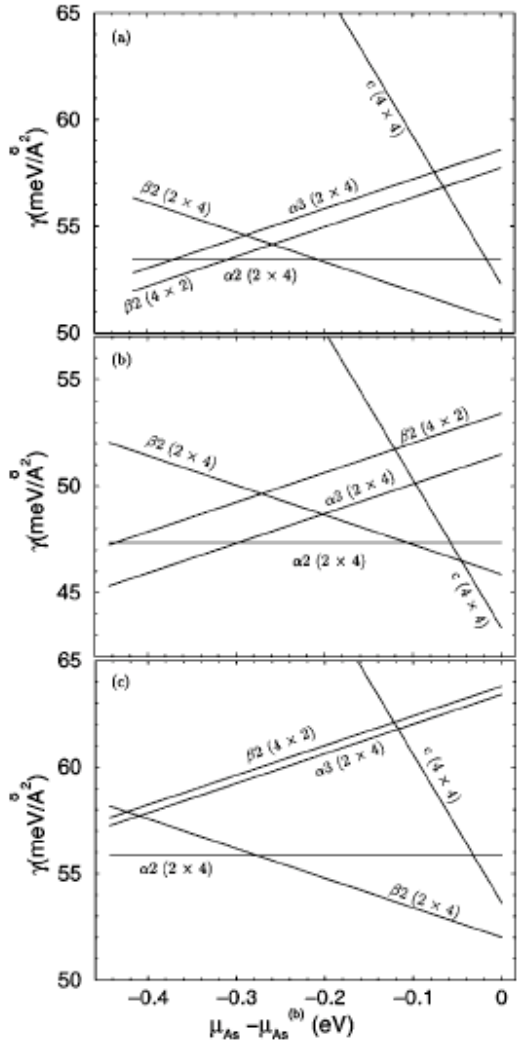

***Figure 1.9**: Energy vs. chemical potential of As, μ_{As}-$\mu_{As(bulk)}$ for InAs at (top) the InAs lattice parameter, (center) 4% biaxial tensile strain, and (bottom) 4% compressive biaxial strain. From [29].*

Strain has also been suggested to stabilize surface reconstruction *coexistence* in both Group IV and III-V semiconductors. Si has a transition temperature at ~860°C where it changes from a (1x1) reconstruction to a (7x7) reconstruction. During this transition, triangular domains of (7x7) reconstruction nucleate and coexist with the background (1x1) reconstruction [31]. Dramatic differences in the surface reconstruction in the form of dimers and other strain inducing features lead to an inward force on these triangular domains. These domains were studied by Tromp and Hannon, who developed a thermodynamic model that accurately describes these islands during the coexistence. Specifically, they showed that size of the islands is controlled by the competing

interactions of boundary energy, the difference in surface energy between the two reconstructions, the elastic relaxation energy of the reconstructions, and a corner energy. The competing interactions try to minimize the surface energy while maximizing the elastic relaxation on the surface. This same model was adapted to describe reconstruction coexistence in the III-V semiconductor alloy $In_{0.89}Ga_{0.21}As/InP$. $In_{0.89}Ga_{0.21}As/InP$ has a 2% compressive lattice mismatch strain. It also exhibits a *coexistence* of two reconstructions on the surface. This is significant for two reasons: (1) this coexistence is not seen in the binary III-V semiconductors and is unique to the alloy system, and (2) the coexistence is between a (4x3) and β2(2x4) reconstruction, and while the β2(2x4) is seen in both InAs and GaAs, the (4x3) reconstruction is unique to the alloy system. By adapting the model for triangular domains developed by Tromp, Sears was able to model the β2(2x4) domains in this InGaAs system [32]. In this system, the islands are typically rectangles elongated along the $[1\bar{1}0]$ as seen in Fig. 1.10 (left). For these rectangular domains the equation becomes:

$$\Delta G = 2(s+t)\beta + st\Delta\gamma + U(s,t) + E_c \qquad (1.2)$$

where ΔG is the system free energy, s and t are the lengths of the two edges and β is the boundary energy, Δγ is the difference in surface free energy, U is the elastic relaxation function, and E_c is the corner energy. The adapted model can be simplified down to a single independent variable Bx/By where Bx and By are the boundary energy in the horizontal and vertical directions, respectively. The data can then be fitted to the model and an approximate Bx/By ratio determined, as seen in Fig. 1.10 (right). This finding demonstrates that lattice mismatch strain may induce a *coexistence* of multiple reconstructions in the III-V semiconductor alloys that is not seen in the binary systems. However, this model does not take into account differences in composition which may occur in the (4x3) and β2(2x4) domains, nor fully determine the thermodynamic coefficients in the model. Thus, while it shows the importance of strain within the system, it does not fully explain the impact of strain on III-V semiconductor alloys.

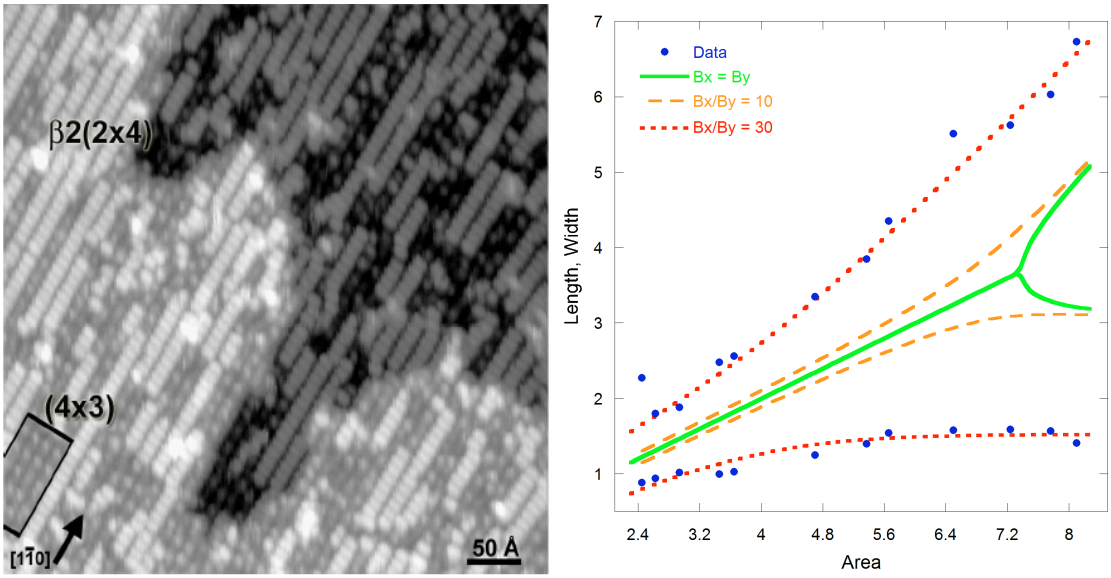

***Figure 1.10**: (left) STM image of $In_{0.79}Ga_{0.21}As/InP$ showing a coexistence of (4x3) and β2(2x4) reconstructions [33] (right) Fitting of the thermodynamic model to β2(2x4) domains [34].*

v. Objectives and Organization

This dissertation examines the impacts of strain on the surface reconstructions of III-V semiconductor alloys. The III-V semiconductors are used as a model system representative of any covalently bonded system. Specifically, this dissertation will examine: the two questions posed in section I.iii:

- What are the roles of chemistry, lattice mismatch strain and atomic size mismatch strain in determining the stability, and structure of alloyed surface reconstructions?
- What roles do alloyed surface reconstructions play in subsequent film growth?

These two questions will lead to a better understanding of the impact of strain on the surface structure of surface reconstructions and understand the impact of these alloyed surface reconstructions on subsequent alloyed film growth.

In order to do this, this study combines experimental and computational methods. Experimentally, the alloying and lattice parameter are coupled in the III-V semiconductor system. In order to examine the separate roles of strain and composition, computational tools will be used which can independently vary the lattice parameter and the surface composition. This will be closely paired with

experiment to keep the simulations as close to the actual physical system as possible. Allowing the simulations to inform the experiments and the experiments to inform the simulations will allow for a deeper understanding of the individual roles of alloying and strain in surface reconstruction stability.

Two semiconductor model systems were chosen for this study: InGaAs/GaAs and GaSb/GaAs. These two systems were chosen for their technological importance in devices, their similarities, and their differences. By examining these two systems, multiple facets of alloying and strain can be examined:

- Two types of strain
  - Atomic Size Mismatch Strain
  - Lattice Mismatch Strain
- Two types of alloying
  - Growth of alloyed films
  - Growth of films which may alloy at interface
- Two types of semiconductor alloys
  - Mixed cation system
  - Mixed anion system

Certain similarities between these two systems make them ideal model systems for this study. One such similarity is the fact that there is a 7% lattice mismatch strain between GaSb/GaAs and a 7% size mismatch between Ga and In allowing examination of lattice strains and atomic strains on the same magnitude. A second is that both In and Sb are known surface segregants. The surface segregation of these species will, ideally, limit intermixing of the substrate material and deposited film on the surface. Also, in both cases, unique reconstructions exist for the strained film that are not seen in the unstrained film.

Prior work suggests that strain may have a dramatic impact on both the stability and the coexistence of reconstructions in alloyed systems, but it remains a largely unstudied area. The ultimate goal of this work is to understand the fundamental physical parameter of stress and how it impacts the surface structure/bonding/reconstruction in order to better predict surface structures in other systems and to better understand film growth in alloyed systems. A more complete understanding will facilitate growth of better devices, and may open

up new avenues of fabrication by atomic self-assembly on strained surface reconstructions.

This work is divided into six chapters, each addressing different aspects of the impact and interaction between strain and surface reconstructions.

Chapter II: Describes the experimental and computational methods utilized in this work. This chapter also details the growth parameters of experimental samples and the parameters of the computational studies.

Chapter III: Describes the mixed cation system InGaAs/As. In this system there is a surface reconstruction coexistence that is unique to the alloy system. Also, atomic mismatch strain induces a dimer ordering in the α2(2x4) that is not seen in the binary constituents. The structure of the (4x3) reconstruction is examined as a function of lattice mismatch strain and atomic size mismatch strain.

Chapter IV: Describes the mixed anion system GaSb/GaAs. This chapter shows the dramatic role that lattice mismatch strain can have on an alloy surface, impacting both the stability of individual surface reconstructions as was postulated by Ratsch [29] and also inducing a surface reconstruction coexistence due to elastic relaxation of the lattice parameter at 2D island edges.

Chapter V: Examines subsequent film growth in the GaSb/GaAs system. This chapter shows the dramatic impact the surface reconstruction has on the subsequent film growth and insertion of defects into the interface. It also examines the profound coupling of the strain field of the surface reconstruction with a 90° edge dislocation.

Chapter VI: Summarizes the major findings of this work, offers conclusions, and suggests possible future work in this area.

vi. References

1. A. Kubetzka, P. Ferriani, M. Bode, S. Heinze, G. Bihlmayer, K. von Bergmann, O. Pietzsch, S. Blugel, and R. Wiesendanger. *Phys. Rev. Lett.* **94**, 087204 (2005).
2. F. Brochard-Wyart, R. Fondecave, and M. Boudoussier. *Int. J. of Eng. Sci.* **38**, 1033 (2000).
3. G. A. Somorjai. *Annual Rev. Phys. Chem.* **45**, 721 (1994).
4. U. Welp, V. K. Vlasko-Vlasov, X. Liu, J. K. Furdyna, and T. Wojtowicz. *Phys. Rev. Lett.* **90**, 167206 (2003).
5. S. Froyen, and A. Zunger. *Phys. Rev. B* **53**, 4570 (1996).
6. R. G. Dandrea, C. B. Duke, and A. Zunger. *J. Vac. Sci. and Tech. B* **10**, 1744 (1992).
7. E. Bauer. *Zeitschrift für Kristallographie* **110**, 372 (1958).
8. P. Kratzer, E. Penev, and M. Scheffler. *Appl. Surf. Sci.* **216**, 436 (2003).
9. W. Qian, M. Skowronski, R. Kaspi, M. De Graef, and V. P. Dravid. *J. Appl. Phys.* **81**, 7268 (1997).
10. Z. X. Xie, X. Xu, J. Tang, and B. W. Mao. *J. Phys. Chem. B* **104**, 11719 (2000).
11. E. F. Schubert. "Bandgap Energy vs. Lattice Parameter" *<http://www.ecse.rpi.edu/~schubert/Light-Emitting-Diodes-dot-org/chap12/F12-06%20III-V%20bandgap%20energie.jpg>*
12. D. E. Jesson, T. P. Munt, and C. Lou. *Jap. J. Appl. Phys.* **43**, 7230 (2004).
13. J. W. Matthews, and A. E. Blakeslee. *J. Cryst. Growth* **27**, 118 (1974).
14. B. P. Rodriguez. "Alloys Containing Antimony as Metamoprhic Buffer Layer for Device Applications," University of Michigan, Ann Arbor, 2006.
15. P. Bhattacharya. *Semiconductor Optoelectronic Devices (2nd Edition),* 1998.
16. S. Narasimhan, and D. Vanderbilt. *Phys. Rev. Lett.* **66**, 1721 (1991).
17. Y. L. Wang, H.-J. Gao, H. M. Guo, H. W. Liu, I. G. Batyrev, W. E. McMahon, and S. B. Zhang. *Phys. Rev. B* **70**, 073312 (2004).
18. K. Ouara, V. G. Lifshits, A. A. Saranin, A. V. Zotov, and M. Katayama. *Surface Science: An Introduction,* Springer-Verlag, Berlin, 2003.
19. P. Atkins, and J. de Paula. *Physical Chemistry, 7th ed,* W. H. Freeman and Company, New York, 2002.
20. H. Bulou, and C. Goyhenex. *Phys. Rev. B* **65**, 045407 (2002).
21. M. D. Pashley. *Phys. Rev. B* **40**, 10481 (1989).
22. V. Bresslerhill, M. Wassermeier, K. Pond, R. Maboudian, G. A. D. Briggs, P. M. Petroff, and W. H. Weinberg. *J. Vac. Sci. and Tech. B* **10**, 1992 (1992).

23. W. Barvosa-Carter, R. S. Ross, C. Ratsch, F. Grosse, J. H. G. Owen, and J. J. Zinck. *Surf. Sci.* **499**, L129 (2002).

24. A. S. Bracker, M. J. Yang, B. R. Bennett, J. C. Culbertson, and W. J. Moore. *J. Cryst. Growth* **220**, 1492 (2000).

25. S. B. Zhang, and A. Zunger. *Phys. Rev. B* **53**, 1343 (1996).

26. M. C. Righi, R. Magri, and C. M. Bertoni. *Phys. Rev. B* **71**, 75323 (2005).

27. R. R. Wixom, L. W. Rieth, and G. B. Stringfellow. *J. Cryst. Growth* **265**, 367 (2004).

28. D. Sander, Z. Tian, and J. Kirschner. *Sensors* **8**, 4466 (2008).

29. C. Ratsch. *Phys. Rev. B* **63**, 161306 (2001).

30. F. Patella, A. Sgarlata, F. Arciprete, S. Nufris, P. D. Szkutnik, E. Placidi, M. Fanfoni, N. Motta, and A. Balzarotti. *J. Phys. Condens. Matter* **16**, S1503 (2004).

31. R. M. Tromp, and J. B. Hannon. *Surf. Rev. and Lett.* **9**, 1565 (2002).

32. L. E. Sears, J. M. Millunchick, and C. Pearson. *J. Vac. Sci. Techol. B* **26**, 1948 (2008).

33. A. Riposan. "Surface Reconstructions and Morphology of InGaAs Compound Semiconductor Alloys," University of Michigan, Ann Arbor, 2004.

34. L. E. Sears. "Investigations of Surface Reconstructions and Inverse Stranski Krastanov Growth in InGaAs Films," University of Michigan, Ann Arbor, 2009.

Chapter II

Experimental and Computational Methods

This study combines experimental and computational techniques to determine the fundamental impact of strain on covalently bonded alloy structures. A number of different experimental and computational techniques were used during the course of the study. This chapter describes the different techniques used, specifically molecular beam epitaxy (MBE), reflection high energy electron diffraction (RHEED), multi-beam optical stress sensor (MOS), scanning tunneling microscopy (STM), transmission electron microscopy (TEM), atomic force microscopy (AFM), Density Functional Theory (DFT), and monte carlo (MC). This chapter is by no means an extensive description of these tools, which are common to the field, but strives to provide a fundamental overview for scientists not familiar with the individual techniques. This chapter also describes the experimental and computational parameters for the studies described in the following chapters.

i. Experimental Methods

Samples were grown on an EPI930 MBE chamber with solid source In and Ga and valved-cracker Sb and As at temperatures determined by an optical pyrometer. Growth rates were determined through RHEED oscillations, and samples were characterized *in situ* with RHEED and *in vacuo* with STM. Other characterization techniques such as MOS, AFM, and TEM were performed as needed.

a. *Molecular Beam Epitaxy (MBE)*

Molecular Beam Epitaxy is one of a handful of thin film growth techniques. Other thin film growth techniques include, but are not limited to, metal-organic chemical vapor deposition (MOCVD), pulsed laser deposition (PLD), vapor liquid solid growth (VLS). One advantage that MBE has over these other methods is the quality of films grown and the ability to control the growth parameters. However, relative to some of these growth methods, MBE is a slower growth technique, which is a disadvantage for scale up from a single laboratory setting to large-scale industrial production.

Epitaxy is defined as the growth of monocrystalline films on a monocrystalline surface. MBE is an epitaxial technique performed at ultra-high vacuum where a source flux of gaseous atoms is directed via line of sight towards a crystalline substrate where the atoms adsorb and incorporate into a crystalline film. The crystalline substrates are initially mounted onto a Mo puck using a thin layer of liquid In which wets both the back of the substrate and the front of the Mo puck. The puck is loaded into the Intro chamber where it is heated to 150°C to desorb any contaminants, including water, from the sample. The sample is then moved into the Buffer chamber, which is attached to the Growth chamber, the STM chamber, and the FIB chamber (which was not used for this study). The Growth chamber consists of a heated, rotating manipulator that holds the sample, an optical pyrometer, a Staib RHEED gun and phosphorous screen, and eight effusion cells. The kinetics of the growth are controlled by the temperature at which the growth is carried out and by the number and magnitude of the fluxes directed at the substrate. Atoms adsorb on the surface and then may either desorb or diffuse along the surface. In III-V growths, Group V materials tend to be particularly volatile because of their high vapor pressure. As a result, III-V growths often take place under an excess Group V overpressure. Group III materials have a lower vapor pressure and therefore have a sticking probability of ~1. As such, since all the Group III flux arriving at the sample surface sticks and is incorporated, the Group III material

controls the incorporation of new monolayers (ML) of material onto the surface and is used to determine the growth rate of III-V films.

The fluxes of incoming material are controlled in two ways. The start and stop of the flux is controlled by air driven shutters between each of the cells and the growth chamber, which actuate in a fraction of a second to regulate the exposure of the substrate to flux. The magnitude of the flux is controlled by the temperature of the effusion cell which heats source material in a ceramic crucible until the materials evaporates or sublimates (Group III and Group V respectively). The magnitude of flux is then altered by increasing or decreasing the temperature of the cell and thus controlling the rate at which material becomes gaseous (Group III) or by holding the cell at a constant temperature and altering the flux via a valved cracker which opens and closes the neck of the effusion cell (Group V). The fluxes, or growth rates, are characterized using a Beam Flux Monitor (BFM)–an ion gauge placed directly in the line of site of the flux–or through RHEED oscillations.

b. *Reflection High Energy Electron Diffraction (RHEED)*

Reflection High Energy Electron Diffraction (RHEED) is a common *in situ* characterization tool used in MBE to monitor the surface structure during growth and to calibrate the growth rates of different materials before growth. RHEED is a diffraction technique, which means that the results show reciprocal space mapping of the volume being probed. In this case, a 15kV electron beam is brought into the sample at a very glancing incidence angle of only 1-3°. The small angle of incidence means that the electron beam only interacts with the top few surface layers, resulting in a very surface sensitive technique that gives information about surface structure and surface roughness. The beam both reflects and diffracts off the sample surface and then impacts a phosphorous screen on the opposite side of the chamber. The resulting RHEED pattern is the result of the intersection of the Ewold sphere and the screen, which satisfies the Laue diffraction conditions as seen in Fig. 2.1. The relationship between real space and reciprocal space coupled with the limited penetration of the electron beam results in a line pattern rather than the spot pattern typically associated

with diffraction. The resulting RHEED pattern has lines that are associated with both the bulk crystal and the surface reconstruction. The bulk crystal results in periodic lines, which correspond to the lattice parameter of the crystal. The surface reconstruction has periodicities larger than the underlying bulk crystal, resulting in superlattice rods between the bulk periodicity rods. An example of a typical RHEED image is shown in Fig. 2.2. The RHEED pattern displays the intersection of the beam with the rods of the reciprocal lattice, i.e. the crystallographic periodicity *normal* to the beam direction. By rotating the sample, the surface periodicity along all surface crystallographic directions can be probed.

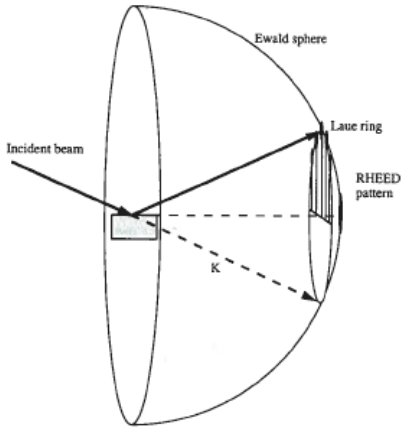

***Figure 2.1**: Image showing incident electron beam, reflected/diffracted beam, and intersection of this beam with the Laue ring and Ewold sphere. Image taken from [1].*

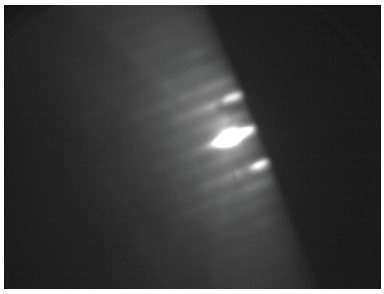

***Figure 2.2**: Typical RHEED image showing primary lines (arrows) and secondary lines (lines) due to the surface reconstruction. This is a x2 periodicity pattern because of the single superlattice line.*

The RHEED pattern is also impacted by surface roughness. This is of great use in calibration of flux rates. As the surface roughens, the intensity of the RHEED pattern dims, and as the surface smoothens, the intensity of the RHEED pattern increases. Thus, as a single monolayer of materials is put down, initially

the surface roughens, forming 2D islands, until 0.5ML has been deposited. Then, the next 0.5ML acts to fill in the holes on the surface and allows the islands to coalesce, smoothing the surface. Thus, by analyzing the intensity of the RHEED pattern, or more specifically the specular spot, which is the reflected component of the electron beam, the incorporation of material into the surface as a function of time can be determined in ML/s. A schematic of how RHEED oscillation intensity correlates to surface roughness is shown in Figure 2.3.

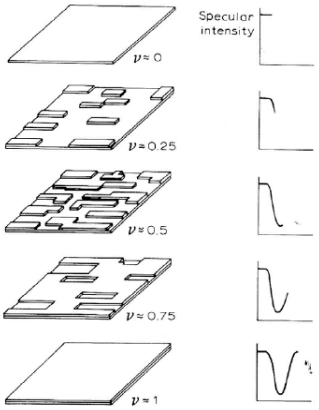

***Figure 2.3**: Model of growth surface and intensity of specular spot as a function of surface coverage, n. From [1].*

c. *Multi-Beam Optical Stress Sensor (MOS)*

Multi-Beam Optical Sensor (MOS or MOSS) is an *in situ* characterization technique to measure stresses during film growth. The initial idea for MOS came from deposition of thin films on cantilevers. Due to the compressive or tensile stress of the film, the cantilever would bend concave or convex in order to relieve the strain. The amount of displacement could be measured and used to back calculate the stress in the film. The MOS works in much the same way but can be used to characterize full wafers during MBE growth. A 3" wafer is freely mounted in a Mo ring and only secured at the edges, leaving the wafer free to curve in either the convex or concave direction. A singe HeNe laser is directed through two etalons and then onto the sample surface. Each etalon is angled at ~45° from the laser beam direction. Gratings on the etalon surface break the beam into a row of parallel beams. Placing the etalon at 90° from one another results in an array of beam spots in the horizontal and vertical directions. The array of laser spots are reflected from the surface of the sample wafer back to a

CCD camera mounted external to the chamber and the results are fed into MOS software developed by K-space. A schematic of the MOS is shown in Fig. 2.4. The distance between spots in both the horizontal and vertical direction is recorded as a function of time. This curvature is directly related to the strain on the surface by:

$$\kappa(t) = \frac{\cos(\alpha)}{2L}\left(1 - \left\langle \frac{D(t)}{D_0} \right\rangle\right) \tag{2.1}$$

where k(t) is the curvature as a function of time, α is the angle of incidence of the beam, L is the distance traveled from the sample to the CCD camera, and $\langle D(t)/D_0 \rangle$ is the average spacing between adjacent beam spots. The curvature is then related to strain, ε, and stress thickness, S(t) through:

$$\varepsilon(t) = \frac{M_s h_s^2}{6 M_f h_f}\kappa(t) \tag{2.2}$$

$$S(t) = \frac{M_s h_s^2}{6}\kappa(t) \tag{2.3}$$

where M_s and M_f are the biaxial moduli of the substrate and film respectively, and h_s and h_f are the thickness of the substrate and film respectively. These results can be used to analyze the stress evolution in the film as a function of time and also to examine the amount of strain relieved within the film and the residual strain within the film. These results describe the impacts on stress due to the film surface stress as well as the interfacial surface stress between the film and substrate. Analysis of the stress thickness, which describes the stress evolution of the film as a function of time can sometimes be used to determine surface segregation values in films as well as pseudomorphic growth regimes.

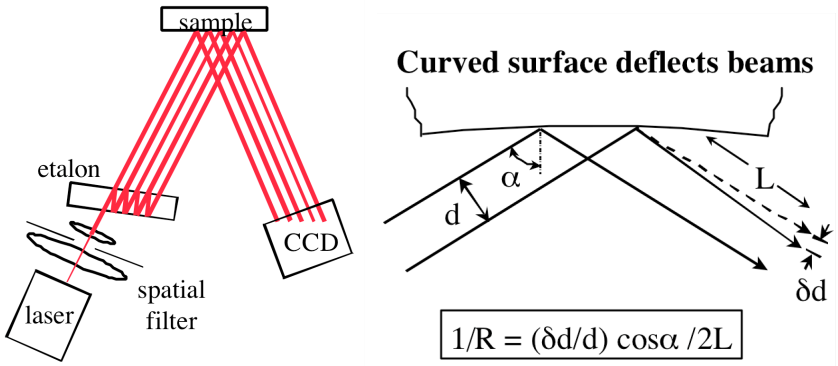

***Figure 2.4**: (left) Schematic of MOS system and (right) schematic of laser deflection due to wafer curvature. Images from [2].*

d. *Scanning Tunneling Microscopy (STM)*

Scanning Tunneling Microscopy (STM) is a technique commonly used to more closely characterize the surface of epitaxially grown materials. In the chamber used for this work, the STM, which was designed by RHK, is connected *in vacuo* to the growth chamber. This is so that surfaces can be examined without taking them out of vacuum so surfaces can be examined without oxidizing or adsorbing other material. The STM works by bringing an "atomically sharp tip" within a tunneling junction of the surface and applying a voltage. The applied voltage induces electrons to tunnel across the gap either from the tip to the surface (negative bias, filled state image) or from the surface to the tip (positive bias, empty state image). A piezoelectric keeps the current constant as the tip is rastered across the surface resulting in a map of "z-height" as a function of position. In actuality, the height is a combination of both the height and the density of electrons on the surface. The result is an image of atomic positions and relative heights as a function of position. By imaging under both positive and negative bias, some information about surface chemistry can be gleaned. According to the electron counting rule (ECR) for III-V semiconductors, Group III atoms have empty dangling bonds and Group V atoms have filled dangling bonds. The result is that Group V atoms appear more brightly in filled state images and Group III atoms appear more brightly in empty state images.

Typical images within this work were taken at 100pA with a tunneling voltage of -4V. This is higher than commonly seen for As containing compounds such as InAs and InGaAs which are better imaged at lower voltages. However,

the higher work functions of Ga (over In) and Sb (over As) require a higher voltage to result in a stable imaging tip. Ultra sharp tips were either purchased or prepared in house. The purchased tips were PtIr and the in house tips were prepared by etching Tungsten wire in a NaOH solution.

e. *Atomic Force Microscopy (AFM)*

Atomic Force Microscopy (AFM) is an *ex situ* surface characterization tool that, while it does not resolve individual atoms, can resolve atomic steps and is a useful tool for large area surface characterization. While typical STM images are only 500-1000Å, the AFM can take large scale images of 5-20μm allowing for characterization of surface roughness, step edge density, QD and pit size. Generally AFM works by rastering a pointed tip at the end of a cantilever across the sample surface to determine a height profile of the sample surface as a function of position on the sample. Many different varieties of AFM can be performed by varying the contact method (contact or tapping mode), the cantilever (magnetic force AFM), or the medium in which the sample is examined (liquid or gaseous media). In each of these cases a laser beam is reflected from the back of the cantilever to a photodiode with four quadrants. The deviation of the reflected laser beam from the center of the photodiode array allows accurate determination of the cantilever deflection by the AFM software. The cantilever is rastered across the sample surface by means of two piezoelectric actuators. A third piezoelectic moves the cantilever in the direction normal to the surface. This piezoelectric is on a feedback loop keeps the force constant by raising and lowering the cantilever according to parameters defined by the user. These parameters are generally material specific depending on the hardness of the sample being examined. The resulting data is a map of height or oscillation phase as a function of position on the surface is developed. Either of these can be determined for forward or reverse scanning of the surface, and as a result artifacts may be determined.

The samples in this study were examined using tapping mode AFM. It is a good method for softer surface materials since it taps the cantilever tip across the surface rather than dragging the tip across the surface. This mode also

allows for "phase" determination. In tapping mode AFM the cantilever, typically Si, is set to oscillate at a resonant frequency which is specific to the particular cantilever. When the cantilever is brought to the sample surface it continues to oscillate, tapping with light force on the sample surface as it is rastered across. In this mode the deviation of the reflected laser beam from the center of the photodiode array gives information not only on the cantilever deflection but also on the oscillation frequency. Changes in frequency are mapped as "phase" and give information on the relative hardness of different features on the sample surface. Comparison of the height and phase images can also be used to determine the presence of scan artifacts. A diginal nanoprobe IIIa was used to take the images presented.

f. *Transmission Electron Microscopy (TEM)*

Transmission Electron Microscopy (TEM) is a difficult technique with many subtleties. For this reason, and the relatively small number of TEM images present in this dissertation, a detailed description of this technique is not included here. Instead, for further information, some suggested resources are [3] and [4]. In general, TEM focuses a high energy electron beam onto a sample either as an array of parallel beams (bright field imaging) or as a single spot (diffraction patterns). Images were taken on a JOEL 3011 microscope at 300kV at angles close to a crystallographic axis in order to allow for high resolution imaging.

Sample preparation was done by mechanically grinding samples attached in cross-section to sacrificial Si pieces. They were polished on 600 grit and 1200 grit paper to a mirror finish and then wedged in on one end to create an ultra thin tip. Finally they were ion-milled using a "Precision Ion Polisher" at 6° with 4kV beam then 4° with a 2kV beam.

g. *Material Growth: InGaAs/GaAs*

The InGaAs/GaAs samples were grown by a colleague, Alex Riposan. The growth parameters are described here because these samples are

characterized within this dissertation due to their unique surface structure, which was hypothesized to result from strain.

The oxide of a GaAs(001) wafer was desorbed at T=630°C according to a pyrometer, followed by the deposition of a 600nm GaAs buffer layer at a rate of R_{Ga}=0.55 monolayers per second (ML/s) and an As_4 overpressure of ~$8x10^{-6}$ torr. Next, the temperature was dropped to 490°C and films of $In_{0.27}Ga_{0.73}As$ were grown to thicknesses between $5 \leq h \leq 25$ ML followed by annealing at the growth temperature for $0 \leq t \leq 40$ minutes. The samples were quenched to T=300°C under an As_4 overpressure of $8x10^{-6}$ torr and then cooled to room temperature under no As overpressure, maintaining a (2x3) reconstruction according to RHEED. The samples were transferred to the *in vaccuo* STM where they were characterized using a scanning current of 100pA and a bias voltage of $-3.36 \leq V \leq -2.25$V.

h. *Material Growth: Determination of Sb and GaSb growth rates*

Growth rates for all samples were determined through reflection high energy electron diffraction (RHEED) oscillations. Group III oscillations were taken in the typical method used by III-V MBE growers by opening and closing the Group III shutter in III-As homoepitaxy under a high As_4 overpressure. The sticking coefficient of Group III material is assumed to be one for the sake of these oscillations. This assumes that all Group II material landing on the surface incorporates into the surface. As the Group V sticking coefficient is lower due to the high volatility of the Group V species, the growth rate of the film can be assumed to be that of R_{III}. Ga oscillations were taken at T~600°C, and In oscillations were taken at T~460°C.

Arsenic oscillations were taken as "uptake" oscillations. A GaAs surface was prepared at T=585°C. This is followed by depositing ~10ML Ga onto a GaAs surface under no As_4 flux, then opening the shutter and examining the incorporation of As into the Ga rich surface.

Sb oscillations were also taken as "uptake" oscillations but require more extensive sample preparation. These were taken using a method developed by a colleague, Catalina Dorin, with some small modifications. A GaAs substrate was

desorbed and a GaAs buffer layer was grown under normal growth conditions (T~600°C according to the pyrometer). The temperature was then dropped to T=450°C according to the substrate heater because the Pyrometer is inaccurate at these low temperatures due to background blackbody radiation. One ML of In was deposited at R_{In}~0.45ML/s followed by the deposition of a single ML of Sb. The V/III ratio is very important to the sample preparation for Sb uptake oscillations with low ratios resulting in very poor sample surfaces which gave poor or no oscillations. A V/III value of ~1.8 gave good results, with the R_{Sb} estimated through a combination of prior growth rates and Beam Flux Measurments (BFM). The optimal BFM value of Sb was found to be ~$4e^{-6}$ torr for R_{In}~0.45ML/s. In order to accurately control the deposition of 1ML Sb, the Sb valve was opened behind a closed shutter. Then the shutter actuation was used to accurately determine growth times. After deposition of 1ML Sb, ~200ML of InSb was grown and then annealed under no Group V overpressure. From there, the oscillations closely resemble As oscillations where a few ML of In are deposited under no Sb flux. Then the Sb incorporation is measured using RHEED. There are three main differences which should be noted: (1) the sample should be annealed under *NO* Group V flux between oscillations, (2) the specular spot is rather streaky and dim, and (3) it is important to always blank the RHEED during anneals of InSb because the intensity of the beam may degrade the oscillation surface.

Typically, Group III oscillations are taken on III-As substrates because these substrates are readily available and significantly cheaper than their III-Sb counterparts. Oscillations describe *incorporation* of the atoms into the surface and there is some differences between As and Sb, so some care must be taken when reporting growth rates. In order to determine the role of the anions in Ga incorporation, Ga rates were taken at the same temperatures on GaAs and GaSb substrates in a single day. As can be seen in Fig. 2.5, at higher growth rates there is a significant difference in the measured Ga rates on the GaAs and GaSb substrates for high growth rates, which plateaus at about 0.115ML/s. This difference becomes much smaller at lower growth rates. Growth rates of III-V films are determined by the Group III material due to the lower vapor pressure of these materials. Utilizing this graph, accurate growth rates for R_{GaSb} were

determined from taking Ga oscillations on GaAs substrates. For the typical growth rate of 0.1ML/s this correction term is small, ~0.04ML/s.

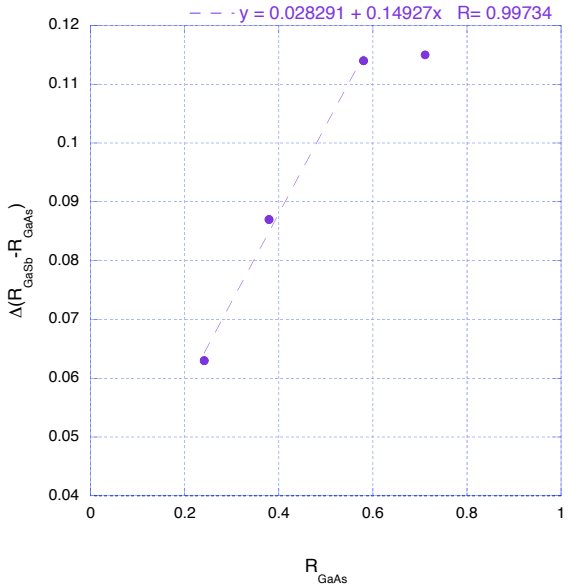

Figure 2.5: *Difference in growth rate of Ga taken on GaSb and GaAs vs. GaAs growth rate.*

i. *Material Growth: GaSb/GaAs*

Samples were grown on GaAs(001) wafers which were prepared by heating under an As_4 overpressure until the surface oxide desorbed between T=600-620°C. A 0.5μm buffer layer was grown at R_{Ga}=0.3 Monolayers per second (ML/s) with a V/III ratio of ~3 to 4.

After growth of the buffer layer, the temperature was dropped 75°C to T=525°C and three different sample types were grown.

(1) *Sb/GaAs* was grown by exposing the GaAs to an Sb flux of R_{Sb}=0.36ML/s. The exposure time was controlled by opening the Sb needle-valve behind a closed shutter and timing the growth with the shutter actuations. Films were grown for exposure times of $0.7 \leq t \leq 28$s, corresponding to estimated thickness of $0.25 \leq h \leq 10$ML (assuming all material deposited is incorporated into the films). A few samples were grown at alternate Sb growth rates and will be identified in the text as needed.

(2) *GaSb/GaAs* was grown by exposing the GaAs substrate to both a Ga flux at R_{Ga}=0.13ML/s (according to the correction factor described

above) and Sb flux at R_{Sb}=0.36ML/s. GaSb films were grown to thicknesses of 0.25 ≤ h ≤ 100ML.

(3) *GaSb/GaSb-(2x8)/GaAs* samples were grown by turning off the As overpressure to form a GaAs (2x4) reconstruction at the completion of the buffer layer at T=600°C. After the (2x4) reconstruction became a Ga rich (4x2) reconstruction the sample was exposed to an Sb overpressure of R_{Sb}=0.36ML/s and then cooled to T=525°C obtaining a GaSb(2x8) reconstruction. Subsequent growth proceeded as for the GaSb/GaAs samples growth to a film thickness of 100ML.

After growth, all samples were then immediately quenched to T=200°C and removed to the Buffer chamber where they were allowed to cool to room temperature under ultra-high-vacuum conditions. Subsequent characterization was performed using the tools described above.

ii. Computational Methods

a. <u>*Density Functional Theory*</u>

The electronic structure of any atom or molecule can be exactly described by the time independent Schrödinger's equation:

$$E\Psi = \hat{H}\Psi = \frac{-\hbar^2}{2m}\nabla^2\Psi + V\Psi \qquad (2.4)$$

where E is the energy, Ψ is the wavefunction of the electronic structure, and $\hat{H}$ is the Hamiltonian which describes the system. The Hamiltonian has two terms. The first, differential term describes the kinetic energy of the particles in the system. The second term describes the potential, V, acting on the particles in the system. Due to the complexity of this equation for multibody systems, particularly the fact that Coulombic interactions between electrons affect the placement of the electrons, the Schrödinger equation can only be solved *exactly* for single-electron systems [5]. A number of approximations such as Hartree-Fock, may be used in *ab initio* calculations to solve for Ψ and E in more complex systems. The Hartree-Fock equations use the variational principal [6] which states:

$$E_0 \le \langle \Psi_t | H | \Psi_t \rangle \qquad (2.5)$$

This equation simply states that the energy of a trial wavefunction is greater than or equal to that of the actual ground state energy. This principal allows for the determination of the Hartree-Fock equations that replace the potential term in the Hamiltonian with the Fock operator which depends on the wave functions of *all* electrons in the system rather than a single electron, allowing the equations to be solved for many-body problems [6]. This allows for many systems to be solved, however, for large systems this method is still prohibitively inefficient.

Density Functional Theory (DFT) takes a slightly different approach. The Hohenberg-Kohn Theorems uniquely describe the energy of a system in terms of the electron density, i.e. a ground-state density uniquely determines the Hamiltonian for the system which uniquely determines the ground-state energy [6]. Unfortunately, there are still two terms which are not exactly known within this formalism and so the equations cannot be solved exactly. The Kohn-Sham approach is based on the Hohenberg-Kohn theorems and utilizes Slater determinants (which are used in the Hartree-Fock formalism) to solve for one of the missing pieces. The rest of the unknown values are placed into a term known as the "exchange correlation" term. This term is small and non-classical arising out of the Pauli Exclusion principal and non-local correlations between electrons and is typically solved within DFT with two approximations, LDA and GGA, which describe the potential field seen by the electrons. LDA is the Localized Density Approximation and describes the field as a single electron in an electron gas of constant density [7]. This approach works well when there are few inhomogeneities in the ground state electronic structure. GGA is the Generalized Gradient Approach and describes the field as the localized slope of the electron density [6]. This approach is typically better when inhomogeneities are present in the electronic structure. With these approximations in place, DFT is a computationally faster tool than the original *ab initio* codes such as Hartree-Fock and allows for accurate determination of the electronic structure of materials allowing the ground state atomic positions and electronic structure to be determined for a wide variety of materials.

b. Computational Parameters

All DFT calculations were performed using the Vienna *ab Initio* Simulation Package, VASP [8-10], using ultrasoft LDA pseudopotentials [11], unless otherwise stated. Typical submission structures consisted of a layer of partially charged H to passivate the bottom surface, surmounted by a frozen bi-layer of III-V material to simulate a bulk substrate of a fixed lattice parameter, three bi-layers of material which were free to relax, and terminated with the surface to be studied. These configurations are termed "slabs". VASP repeats the image infinitely in 3D in order to minimize/eliminate errors due to edges. Thus, to avoid interactions between the pseudo-Hydrogen and the surface, slabs were separated by at least 10Å of vacuum. A k-point convergence test was performed and slabs were relaxed with 6x3, 3x3, 3x4, 6x2, and 6x2 k-point meshes for (2x4), (4x4), (4x3), (2x8), and (2x16) reconstructions repectively. The plane-wave energy cutoff was set at 203.1 eV for all calculations unless otherwise stated, the electronic temperature (kT) was set to 0.025eV, and slabs were relaxed with a VASP relaxation tolerance of 0.1meV. Lattice parameters for InAs, GaAs, GaSb, and InP were determined by volume relaxing the cell, and then statically relaxing the cell for the energy and determined to be 6.018Å, 5.592Å, 6.035Å, and 5.828Å respectively. These values are all within 1% less of their experimentally determined values, as expected for the LDA determination.

c. Simulating STM Images Using VASP

The atomic structure of surface reconstructions is typically determined experimentally using STM. A combination of filled and empty state images is used to determine the placement of atoms on the surface and the composition of atoms within the structure. When examining surface structures using computational methods, it is helpful to be able to simulate STM images of the computational structures examined in order to directly compare the computational and experimental results. STM images were simulated based on the method described by Tersoff and Hamann [12].

This method of simulating STM images has two embedded assumptions: (1) the STM tip is a point charge and (2) there are no interactions between the

STM tip and the surface. In reality, the STM tip is not a point charge. Even if the tip is atomically sharp, the resulting wavefunction is not a perfect sphere. And there are certainly interactions between the wavefunctions of the tip and the surface, making small alterations to the STM image. However, the impacts of both of these effects are minimal, and STM simulations using the partial charge density have been shown to accurately reproduce experimental STM [13, 14].

The partial charge density of the surface is determined computationally using VASP. The electron density is calculated from the Fermi Energy to an input number of volts above or below, and approximately corresponds to the experimental voltage used. Once the partial charge density is calculated using this voltage, the STM image is simulated. A file of height (z) vs. position (x, y) is plotted for different "isosurfaces," or constant current surface in the density file. The "isosurfaces" correlate to the experimental STM current, but while a relatively higher isosurface value corresponds to a relatively higher current, it is impossible to directly relate the value of different isosurfaces to the current. These x, y, z files are then plotted in gnuplot, though any 3D plotting tool can be used. A detailed methodology including how to determine the partial charge density in VASP, the code to determine the isosurfaces, and the code to plot the STM images in gnuplot is included in Appendix A.

iii. References

1. Z. L. Wang. *Reflection Electron Microscopy and Spectroscopy for Surface Analysis,* University Press, Cambridge, 1996.
2. E. Chason. *Use of kSA MOS System for Stress and Thickness Monitoring during CVD Growth,* White Paper at: <http://www.k-space.com/Products/MOSinfo.html#notes>, 2000.
3. D. B. Williams, and C. B. Carter. *Transmission Electron Microscopy,* Plenum Press, New York, 1996.
4. B. Fultz, and J. M. Howe. *Transmission Electron Microscopy and Diffractometry of Materials, 2nd ed,* Springer-Verlag, New York, 2002.
5. S. T. Thornton, and A. Rex. *Modern Physics for Scientists and Engineers, 3rd ed,* Thomson Brooks/Cole, Belmont, CA, 2006.
6. R. G. Parr, and W. Yang. *Density-Functional Theory of Atoms and Molecules,* Oxford University Press, New York, NY, 1989.
7. A. Antons, Y. Cao, B. Voigtländer, K. Schroeder, R. Berger, and S. Blugel. *Europhys. Lett.* **62**, 547 (2003).
8. G. Kresse, and J. Furthmuller. *Phys. Rev. B* **54**, 11169 (1996).
9. G. Kresse, and J. Hafner. *Phys. Rev. B* **47**, 558 (1993).
10. G. Kresse, and J. Hafner. *J. Phys. Condens. Matter* **6**, 8245 (1994).
11. D. Vanderbilt. *Phys. Rev. B* **41**, 7892 (1990).
12. J. Tersoff, and D. R. Hamann. *Phys. Rev. B* **50**, 1998 (1983).
13. W. Barvosa-Carter, R. S. Ross, C. Ratsch, F. Grosse, J. H. G. Owen, and J. J. Zinck. *Surf. Sci.* **499**, L129 (2002).
14. S. B. Zhang, and A. Zunger. *Phys. Rev. B* **53**, 1343 (1996).

Chapter III

Atomic Size Mismatch Strain Stabilization of Ordering

Surface reconstructions can vary from very simple (1x1) patterns to very complex patterns such as the Si-(7x7) reconstruction [1]. The stable reconstruction on binary III-V semiconductor surfaces is impacted by localized displacement strain incurred by moving atoms from their bulk lattice sites. However, the effect of alloy induced point strains on the surface is unstudied in these systems. Atomic size effects have been studied in metallic systems in order to understand lattice parameter changes and the effective radius of a point strain due to dilute alloying. Atomic size mismatch strain has also been computationally shown to have a great impact in bulk atomic ordering in III-V semiconductor systems, inducing a chalcopyrite ordering in III-V superlattice systems [2]. Yet, the understanding of how alloying induced strain affects surface reconstructions remains lacking. This chapter examines how atomic size mismatch strain affects surface ordering and stability, specifically examining the InGaAs model system.

i. Understanding the InGaAs Surface

InGaAs is used both for applications as a sensor for lidar [3] and as a strain-reducing layer for subsequent defect free growth [4]. The binary components, InAs and GaAs, are well studied and understood and their surface reconstructions have been determined and confirmed experimentally and computationally [5-7]. These surfaces are known to exhibit a single surface

reconstruction that changes as a function of chemical potential from a c(4x4) to a β2(2x4) to an α2(2x4) to a (4x2) reconstruction as the amount of As in the system is decreased or the temperature is increased.

The details of the InGaAs reconstructions are less well understood. A lot of experimental work has examined the $In_xGa_{1-x}As$ surface [8-10]. This surface is very interesting in that it exhibits a *coexistence* of two surface reconstructions over a wide compositional range. Moreover, this mixed reconstruction does not simply combine reconstructions known to the InAs and GaAs systems, but rather includes a reconstruction that is unique to the alloy system and unknown in either of the binary systems. Figure 3.1 shows STM images of three different compositions of $In_xGa_{1-x}As$ films grown on the MBE chamber described in Chap. II.i.a. From left to right they are lattice matched $In_{0.53}Ga_{0.47}As/InP$, 2% compressively strained $In_{0.27}Ga_{0.83}As/GaAs$, and 2% compressively strained $In_{0.81}Ga_{0.19}As/InP$. A (4x3) reconstruction is seen in all of these films. Disorder in the (4x3) leads to smaller domains of (nx3) and what is labeled a c(6x4) but is actually an oblique (3x2) [11]. In the compressively strained films, this new (4x3) reconstruction *coexists* with the known α2(2x4) and β2(2x4) reconstructions.

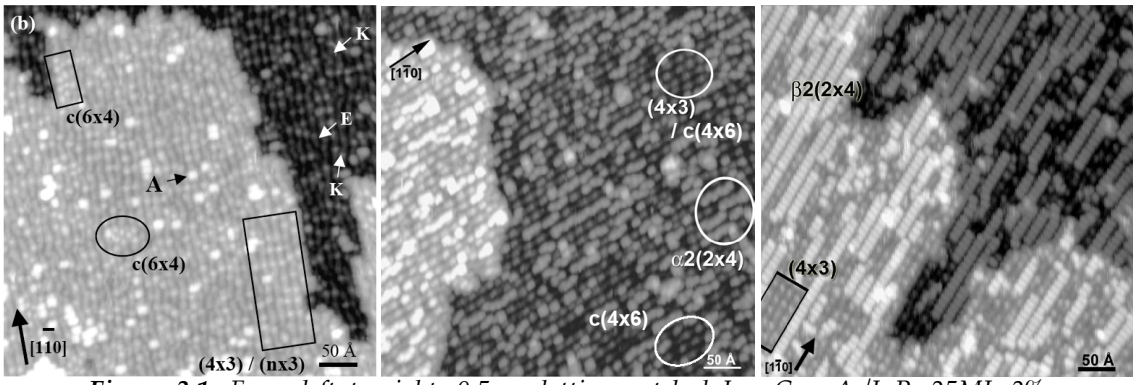

***Figure 3.1**: From left to right: 0.5μm lattice matched $In_{0.53}Ga_{0.47}As/InP$, 25ML 2% compressively strained $In_{0.27}Ga_{0.83}As/GaAs$, and 25ML 2% compressively strained $In_{0.81}Ga_{0.19}As/InP$. Images from [12].*

This reconstruction has been seen by multiple experimental groups, often in coexistence with other reconstructions known for binary III-As films. Placidi *et al*. also report a (4x3) reconstruction coexisting with an α2(2x4) reconstruction for low In content films grown on GaAs [13]. A RHEED/STM study done by Jones *et al.* shows the (nx3) reconstruction, see Fig. 3.2. In this study, the $In_xGa_{1-x}As$ was grown on InAs and GaAs substrates, but to minimize strain a ~0.2μm

buffer layer was grown between each compositional variation. Interestingly, at compositions near x=0.5 a solitary (nx3) reconstruction is seen, as for the lattice matched $In_{0.53}Ga_{0.47}As/InP$ reported by Riposan *et al.* [9]. However, Jones *et al*. do not report coexistence with a (2x4) reconstruction at high and low In composition, but rather report coexistence with a c(4x4) reconstruction at low In content films [10]. Analysis of the STM images of the (4x3) reconstructions in each these cases show the same morphology for the (4x3) reconstruction.

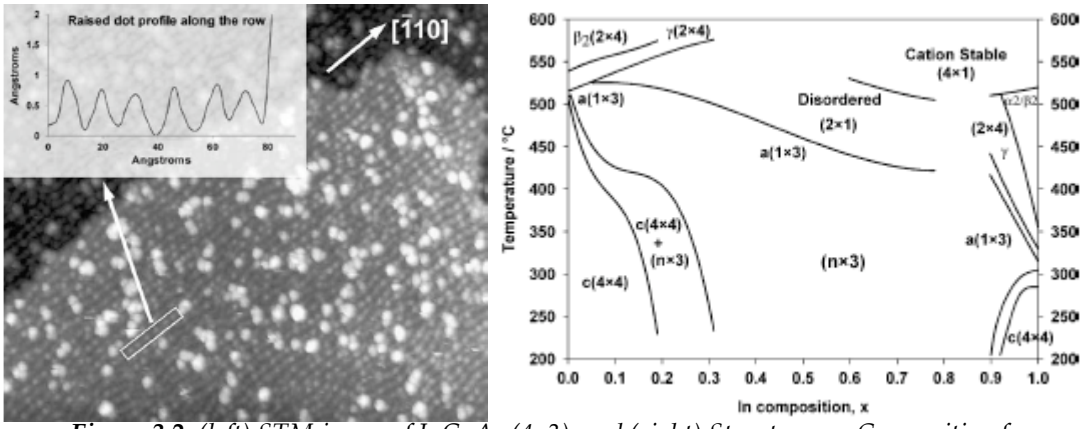

***Figure 3.2**: (left) STM image of InGaAs-(4x3), and (right) Structure vs. Composition for $In_xGa_{1-x}As$ films. Images from [10].*

The coexistence of multiple reconstructions on a semiconductor surface is very interesting as it is *unique* to the alloy system. This coexistence is stable over a wide range of growth conditions and compositions. In homoepitaxial films, the only time a coexistence *might* be seen is at the transition point, either in temperature or composition, between two surface reconstructions. In general, the surface reconstructions of III-V compound semiconductor alloys are more complicated, as the presence of multiple components introduces additional factors that can influence the surface structure including strain. Chemical effects of alloying are negligible in this case due to similarities in the valence structure of elements from the same column of the periodic table. Though, the effects of strain may not be negligible. It is possible that the (4x3) stabilization and the surface reconstruction coexistence may be driven by strain. Elastic relaxation is one of the parameters in the coexistence models for semiconductor surfaces [14, 15]. This is particularly true for alloy systems. In is known to surface segregate and often appears in concentrations higher than expected due to migration of In

with the growth front [16]. Once on the surface, the In may preferentially segregate to a single reconstruction, altering the stress state of the surface. It is also possible that strain impacts the stability of the different reconstructions present. As discussed in I.iv, theoretical work on InAs (001) suggests that reconstruction boundaries shift with lattice mismatch strain [17]. It is uncertain how many of these newly stable reconstruction areas are experimentally accessible. The effect of alloying, or atomic size mismatch strain, on the development of the surface reconstruction has not been explored, nor has either atomic size mismatch strain or lattice mismatch strain been experimentally shown to influence the surface structure.

ii. Understanding Dimer Ordering in the z(4x4) Reconstruction

In general, the InGaAs films exhibit a reconstruction coexistence of a (4x3) reconstruction unique to the alloy, and a reconstruction common to the III-As systems [9, 10]. Figure 3.3 (left) shows one such coexistence for a 25ML thick $In_{0.27}Ga_{0.73}As/GaAs$ film where a rectangle shows a region of α2(2x4) reconstruction and a circle highlights a region of (4x3) reconstruction. The (4x3) consists of bright spots connected by dim lines along the $[1\bar{1}0]$. The α2(2x4) reconstruction itself is very well documented [5] and consists of a row of As surface dimers along the $[1\bar{1}0]$ which sit in one of two positions in the unit cell. These two positions are shown Fig. 3.3 (right) which is a schematic of two α2(2x4) unit cells with dimers in different positions. The presence of multiple dimer positions within a single until cell means that the dimers may form ordered arrangements. The dimers in the α2(2x4) reconstruction can order in a straight row, a zigzag row, or may disorder with dimers distributed randomly in the two positions, as is typical for homoepitaxial IIIas films exhibiting this reconstruction [5]. In contrast, the α2(2x4) dimer arrangements observed in $In_{0.27}Ga_{0.73}As$ films such as the one in Fig. 3.3 display a regular zigzag configuration as the surface dimers alternate between the two possible surface positions. The alternating dimer has also been observed in mixed reconstructions of thin layers of InAs/GaAs(001) [13]. Statistical analysis of the dimer chains for 25ML thick $In_{0.27}Ga_{0.73}As$ films annealed for various times is

shown in Fig. 3.4 with an example chain shown in the inset. The chains were examined for length and for the number of "defects" in the chain, such as that marked in the inset or marked "R" in Fig. 3.3c. The results show the average α2(2x4) chain length is 5 dimers and the incidence of alternating dimers is 80%, i.e. the defects occur 20% of the time. This demonstrates a strong propensity for the alternating configuration, as a random configuration would result in an incidence of 50%. The resulting reconstruction will be termed the z(4x4) within this document due to its zigzag configuration and (4x4) repeat unit. The (4x4) periodicity is not observed in the RHEED which displays a (1x3) pattern. This is due to the low surface coverage and small domain size of the z(4x4).

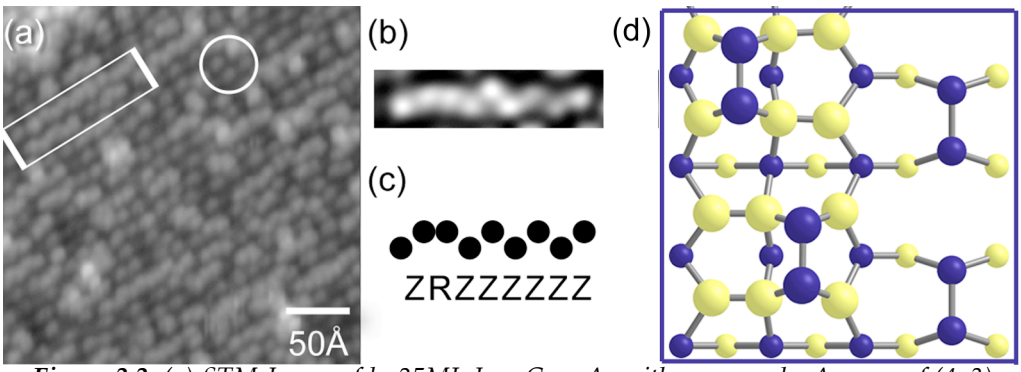

***Figure 3.3**: (a) STM Image of h=25ML $In_{0.27}Ga_{0.73}As$ with no anneal. An area of (4x3) common to the alloy is circled and one of α2(2x4) is outlined by a rectangle. I = 100pA, V = -3.13V. (b) zoomed image of α2(2x4) row showing alternating dimer. (c) schematic of the dimer position showing propensity to alternate position. (d) schematic of the α2(2x4) reconstruction showing the two possible dimer positions within a unit cell.*

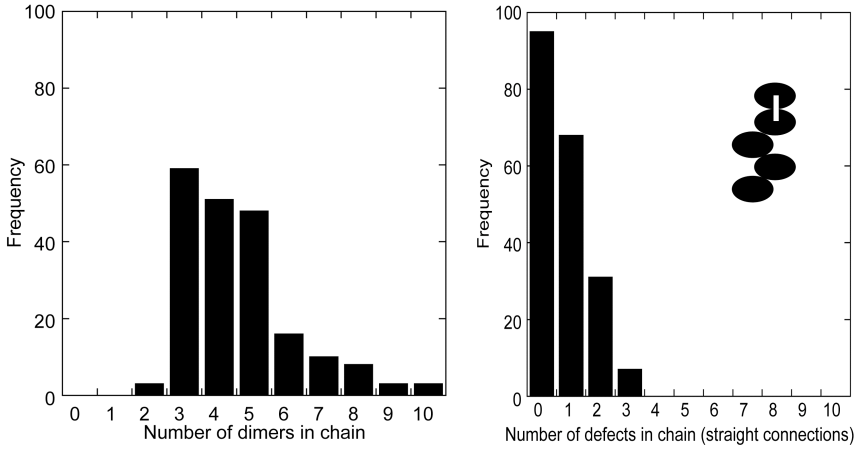

***Figure 3.4**: Statistics of the α2(2x4) reconstruction in $In_{0.27}Ga_{0.73}As/GaAs$ films. Average chain length is 5 dimers and average incidence to alternate position is 80%.*

The fact that the z(4x4) variant of the α2(2x4) reconstruction is observed in lattice mismatched heteroepitaxial films but not in homoepitaxial films or lattice matched heteroepitaxial films suggests that strain plays an important role in affecting the stability of z(4x4) compared to other dimer arrangements. In order to investigate the relative importance of lattice mismatch and atomic size mismatch strain on the different types of ordering possible in an α2(2x4) reconstruction, two atomistic orderings were examined utilizing DFT. The use of computational techniques in this study allows the differing roles of atomic mismatch strain and lattice mismatch strain to be analyzed as the composition and the lattice parameter can be varied independently of one another, unlike in experiments where they are coupled. This makes DFT a strong tool for understanding the fundamental interactions on reconstructed surfaces. The two orderings examined are shown in Fig. 3.5a and 3.5b. Fig. 3.5a is the R-Model, which exhibits a straight row of dimers along the $[1\bar{1}0]$, and Fig. 3.5b is the Z-Model, which consists of a row of alternating dimers along the $[1\bar{1}0]$. The energies of each of these models is normalized per (2x4) unit cell.

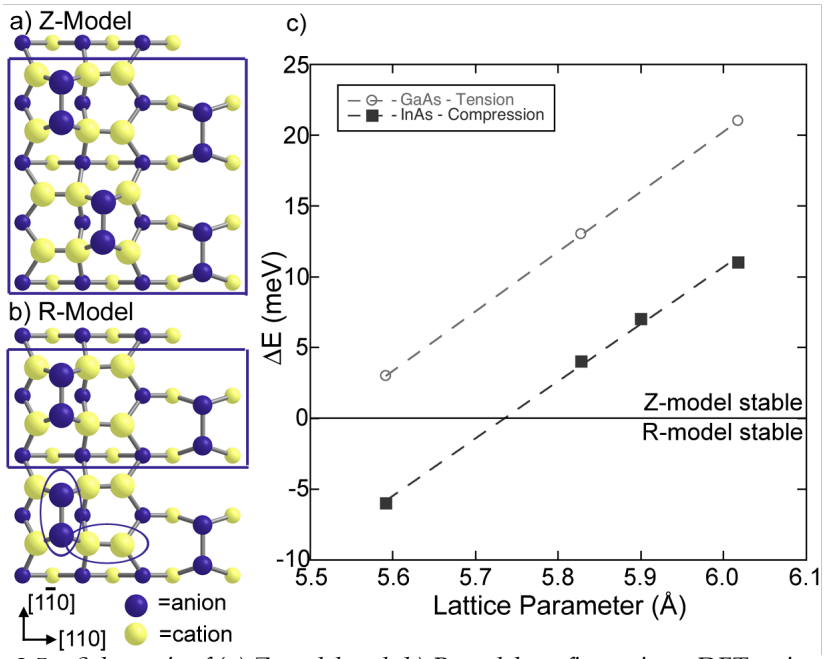

***Figure 3.5**: Schematic of (a) Z model and (b) R model configurations. DFT unit cells are outlined with rectangles and ovals outline one anion surface dimer, and one cationcation dimer. (c) The energy difference of the R model and Z model configurations as a function of lattice parameter for GaAs (open circles) and InAs (closed squares) slabs. $\Delta E = Energy^{R}_{model} - Energy^{Z}_{model}$; therefore, a positive energy means the Z model is more stable.*

Figure 3.5c shows the difference in energy between the R-Model and the Z-Model for pure GaAs and InAs slabs, in tensile and compressive lattice mismatch strain respectively, at LDA lattice parameters ranging from GaAs (5.592Å) to InAs (6.018Å). All energies are reported per (2x4) unit cell. A positive number in Fig. 3.5c indicates that the Z-Model is more stable than R-Model. For pure, relaxed GaAs, the Z-Model is stabilized relative to the R-Model by 3 meV per (2x4) unit cell. However, tensile strain enhances this stability up to 21meV when pure GaAs is strained in tension to the InAs lattice parameter. For pure, relaxed InAs, the Z-Model is also predicted to be more stable than R-Model, in this case by 11meV. This relative stability decreases as the slab is subjected to compressive strain until the lattice parameter reaches 5.74Å, below which the R-Model is stabilized.

While Z-Model is predicted to be stable for pure GaAs and InAs, it is only marginally stable relative to the R-Model, suggesting that thermal fluctuations can easily disorder the alternating dimer arrangement of the Z-Model at finite temperature. Monte Carlo simulations were applied to a lattice-model Hamiltonian describing the configurational energy of As dimers on the α2(2x4) reconstruction for InAs. The Monte Carlo simulations then sampled dimer configurations with a frequency determined by Maxwell-Boltzmann statistics. Three base (2x4) unit cells were examined: the α2(2x4) described in this chapter, the β2(2x4) which has an additional surface As dimer in each unit cell, and a (2x4) unit cell with no surface dimers. The no-dimer (2x4) cell is used as a limiting case for this model is unphysical and is *always* unstable relative to the ζ(2x4) reconstruction seen for In-rich films [18]. However, it provides a lower limit for the (2x4) unit cell in our model. Thus for these results, values below a dimer coverage of 0.5 are for trend analysis only. This lattice model was fit to DFT energies of seven (4x4) unit cell dimer arrangements of InAs at the InAs lattice parameter and includes interactions up to the third nearest neighbor. The model predicts a difference in energy between the z(4x4) and α2(2x4) of 11 meV per (2x4) surface unit cell, in agreement with the DFT simulation results shown in Fig. 3.5c. Monte Carlo simulations were performed in a 24x24 unit cell with 2000 passes and 1000 equilibration steps.

The results of the Monte Carlo studies, displayed in Fig. 3.6, show the stability of the α2(2x4) and β2(2x4) to be as expected. The graph of the left shows dimer coverage as a function of As chemical potential, μ_{As}. The steep jumps of the lines at 0.5 and 1 show that the α2(2x4) and β2(2x4) phases are stable over a range of μ_{As}. The transitions become more gradual as the temperature is increased, showing the expected trend that temperature induces disorder. Correlation analysis between different dimers at the 0.5 dimer coverage allows for statistical analysis of the incidence of alternating dimers between adjacent unit cells. These results, displayed in Fig. 3.6 (right), show that the incidence of the As dimers alternating position on the surface is 53% at typical growth conditions of T=475ºC (748K), and increases to only 61% at T=0ºC (273K). These correlations show that a difference of only 11meV between the R- and Z-Models allows for easy disordering of the Z-Model dimers at finite temperatures, explaining why the z(4x4) reconstruction is not reported for binary systems [5]. These correlations are also in agreement with published experimental work on homoepitaxially grown InAs. Statistical analysis of different published images [5, 7, 19, 20], while not a large enough sample to be robust, suggests that the incidence of alternating dimers is no more than ~58% under a wide range of growth conditions.

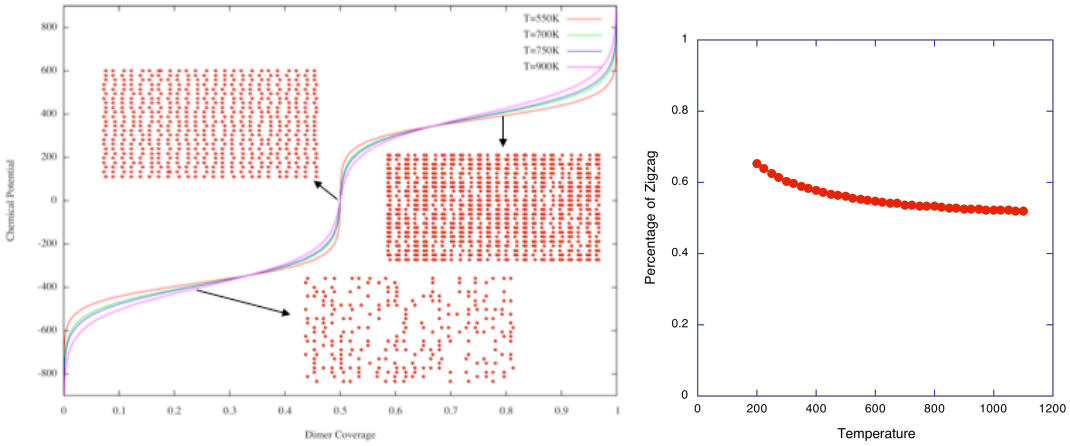

***Figure 3.6**: Monte Carlo simulations of InAs at the InAs lattice parameter. (left) Surface dimer coverage vs. μ_{As} at 550K, 700K, 750K and 900K. The vertical plateau at ~0.5 dimer coverage demonstrates the stability of the α2(2x4) reconstruction over a wide range of μ_{As}. (right) Percentage of alternating dimer configuration (zigzag) on the surface as a function of temperature.*

The small difference in energy between the R- and Z-Models from the GaAs to InAs lattice parameters shows that lattice mismatch strain cannot account for the existence of z(4x4) observed in the $In_{0.27}Ga_{0.73}As/GaAs$ system. The stability of the z(4x4) in the $In_{0.27}Ga_{0.73}As/GaAs$ system must instead derive from phenomena that result from alloying. It is well known that In surface segregates in InGaAs films [16, 21]. This observation is confirmed by DFT calculations on the R-Model surface, which show an energy increase of at least 170meV to move an isolated In in a GaAs slab from the highest energy surface position to the first cation subsurface layer. The energy continues to increase as the In atom is moved deeper into the GaAs slab, confirming a strong *thermodynamic* driving force for In surface segregation, in agreement with calculations for the β2(2x4) reconstruction in InGaAs [22]. For this reason, alloying studies on the relative stability of the R- and Z-Models focused on substitution of In atoms into the 6 surface cation positions of a (2x4) GaAs slab. The fraction of these surface sites occupied by In is denoted X_{In}.

DFT calculations of different configurations of In atoms in the surface sites of the R- and Z-Models show that the placement of In relative to As dimers has a large effect on the surface energy. The In positions with the lowest energy are those furthest from the As dimer, as they appear in Fig. 3.7b and 3.7c. In other words, the In preferentially sits in the cation-cation bond which is oriented along the [110] (circled in Fig. 3.5c). The cation-cation bond is generally in tension because the atom positions are constrained by the subsurface layers. Replacing Ga with the larger In reduces the bond tension and allows for relaxation in the [110] direction due to the 7% size difference between Ga and In. The large In atom can accommodate a longer bond, reducing the displacement from the bulk atomic position. For a slab of either model with surface composition X_{In}=0.33 the calculated bond length for the Ga-Ga cation bond is 2.48Å, while an In-Ga bond is 2.64Å. DFT calculations also show that a straight row of In along the $[1\bar{1}0]$ direction, as is the case in Fig. 3.7b, has a much higher energy than a configuration where the In alternates sides, as it does in Fig. 3.7c, due to the inability of the In to relax in the $[1\bar{1}0]$. If the configuration in Fig. 3.7b is taken as a reference state, alternating the In reduces the energy by 40meV. On the other

hand, alternating both the In and the As dimers, as is seen in Fig. 3.6c, reduces the energy by 132meV. Thus, the arrangement of In into a lower energy alternating configuration coupled with the preference of the In to sit in the cation-cation bond position opposite the As surface dimer induces the surface dimer to also alternate in the zigzag configuration.

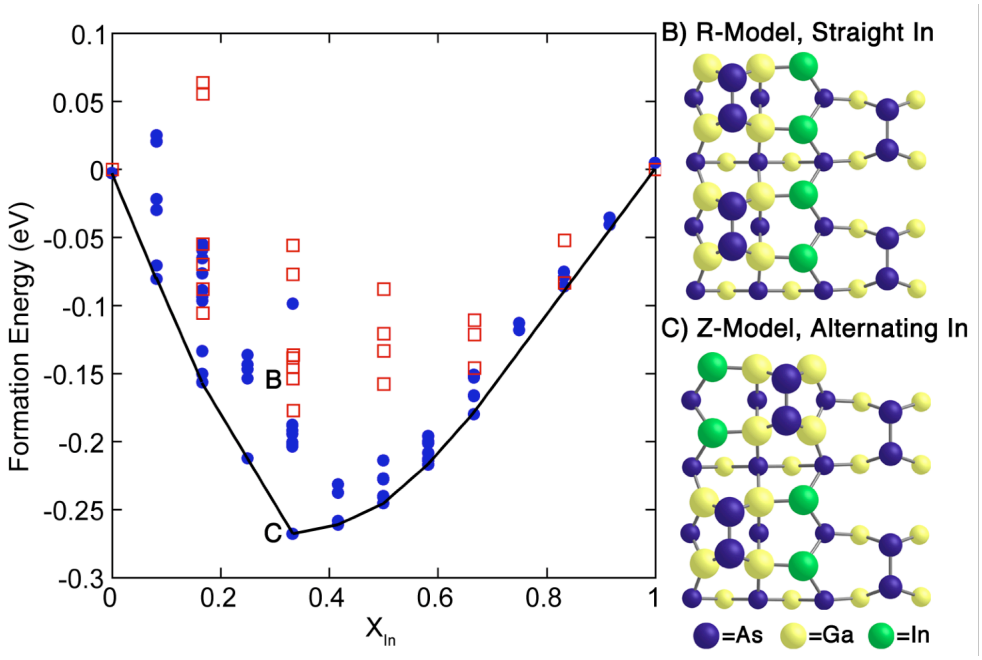

***Figure 3.7**: Convex Hull of the Formation Energy of different configurations of In in the Z-Model (open squares) and R-Model (closed circles) with schematics of configurations at points (b) and (c). Open squares = R-Model, Closed circles = Z-Model.*

There are a plethora of possible arrangements of In in the surface layer which have the same composition, X_{In}. Figure 3.7 shows the formation energy relative to a Z-Model with X_{In}=0 and a Z-Model with X_{In}=1 surface for various atomic configurations as a function of composition. Configurations were determined by systematically placing In into the surface sites, determining the lowest energy configuration for the composition, and repeating this cycle until X_{In}=1 was reached. Fig. 3.7 clearly shows that the Z-Model has a lower formation energy, and thus lower surface energy, for all intermediate In surface concentrations considered. The energy difference starts small at 3meV for X_{In}=0 (pure GaAs) and increases to a maximum of 92 meV at X_{In}=0.33, then decreases until finally the R-Model is stabilized by 4meV at X_{In}=1. The lowest energy Z-Model and R-Model at X_{In}=0.33 show that alternating both the In and the As

dimers is critical to minimizing the energy of the system. Furthermore, the large energy difference across the composition range $0.167 \leq X_{In} \leq 0.667$ is significantly larger than the 11meV difference found for pure InAs and GaAs significantly reducing disordering of the Z-model at typical growth temperatures.

iii. Understanding the InGaAs-(4x3) Reconstruction

The InGaAs-(4x3) reconstruction is seen over a wide variety of compositions but is unique to the InGaAs alloy and does not appear for binary InAs or GaAs. It is apparent from the z(4x4) reconstruction discussion, that atomistic misfit strain can play a large role in impacting surface structure. Computational results from Ratsch also suggest that lattice mismatch strain has the prospect of greatly impacting the stable surface reconstruction [17] and Tromp and Sears show that elastic relaxation may influence surface reconstruction coexistence [14, 15] such as is seen in the InGaAs system. Thus, it is easily hypothesized that the structure of the InGaAs-(4x3) reconstruction may be influenced by strain, either through lattice mismatch strain stabilizing a new reconstruction or by atomic mismatch strain changing the reconstruction stability.

Three main structures have been hypothesized for the (4x3) reconstruction. The first by Sauvage-Simkin *et al*. [8] does not follow the ECR. This model is actually a (2x3) reconstruction consisting of a surface terminated by a double layer of anions and a straight backbone of dimers along the $[1\bar{1}0]$ and adjacent unit cells are separated by a single anion trench dimer along the [110]. A modification of this model by Jones *et al*. [10] through the insertion of a cation on the first subsurface anion plane changes this structure to obey the ECR. A model of the structure is shown in Figure 3.8. As this model is characterized by the backbone of anion dimers, it will be referred to herein as the Anion Dimer model.

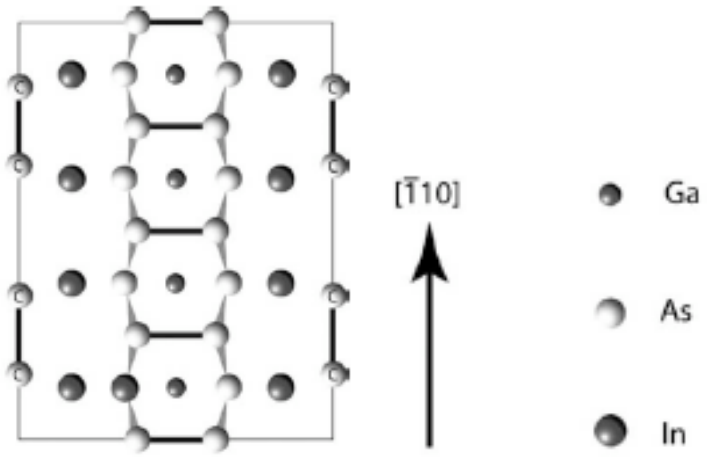

***Figure 3.8**: Proposed (4x3) model of Jones et. al. [10] Notice the insertion of an In in the As sublattice.*

The second proposed model comes out of the Millunchick group, and is a variation of the GaSb-(4x3) proposed by Barvosa-Carter *et al.* [23]. This model is shown in Figure 3.9a. The surface is terminated by a backbone of four surface dimers along the $[1\bar{1}0]$. There are three cation homodimers and a single anion-cation heterodimer that is "kinked" or shifted by one bulk atomic position along the [110]. The kinked dimer is the top dimer seen in Fig. 3.9a. Adjacent unit cells are separated along the [110] by a single anion trench dimer. This model will be referred to herein as the Cation Dimer model. A slight variation on this model is also shown, which includes an additional As dimer on the surface. This model is proposed by Riposan in his thesis [12]. This structure is herein termed the Mixed Dimer model because of the surface heterodimer and surface anion dimer and is an interesting model to study for two main reasons.

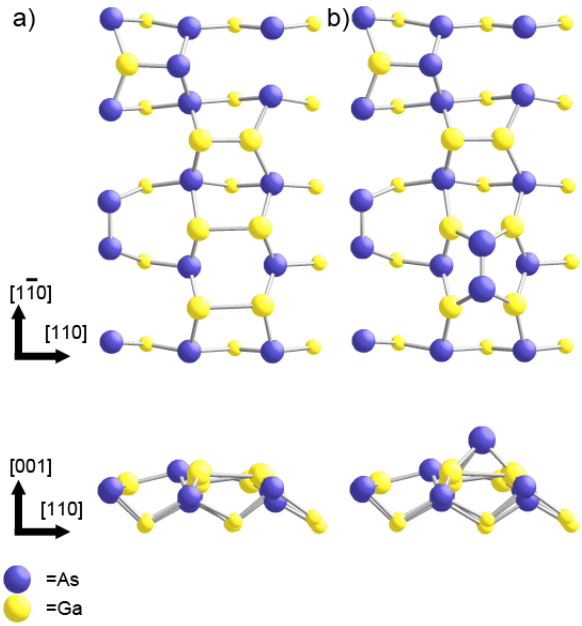

***Figure 3.9**: Schematics of proposed InGaAs-(4x3) models. (a) Cation Dimer model [9] and (b) Mixed Dimer model [12].*

The Cation Dimer model is often criticized for not having enough As in the surface. While the model terminates with θ_{As}=0.5ML, the same as the α2(2x4), the presence of cation homodimers rather than As homodimers terminating the surface often deceives the eye into believing this is an As-poor reconstruction. For this reason, and others, Riposan developed the Mixed Dimer model. This Mixed Dimer model is very interesting due to the height of the additional dimer. Visually, the STM of the (4x3) reconstruction appears to be bright pearls on a dim chain. The height of the additional dimer would make it appear very bright and possibly lead to this sort of STM image.

Each of these proposed models was developed based on STM images of the (4x3) reconstruction. STM is a powerful tool in allowing the imaging of atoms on the structure and some, limited, composition data can be obtained using dual bias imagery. According to the ECR, anions have filled dangling bonds and cations have empty dangling bonds. By altering the bias voltage, the electrons may tunnel out of filled states to the tip or from the tip into empty surface states. Thus anions appear relatively bright in filled state and dim in empty state and cations the reverse. In order to better understand each of the proposed models, simulated STM images were made of each structure. After relaxing structures using DFT, simulated STM images can be determined using

the method of Tersoff and Hamann [24]. They state that, to a first-order, STM images can be simulated by ignoring the wavefunctions of the tip and plotting the local density of states (LDOS) of the surface. This has been shown to reproduce semiconductor STM images well and is a generally accepted method within the field. Fig. 3.10 shows the atomic structures and simulated filled and empty state STM images of the Anion Dimer, Cation Dimer, and Mixed Dimer models. The STM images shown in Figs. 3.1, 3.2, and 3.3 are all filled-state images and show bright pearls separated by dim lines along the $[1\bar{1}0]$. As can be seen from Fig. 3.10a, the Anion Dimer Model has a series of bright bands of intensity along the $[1\bar{1}0]$, which does not reproduce the experimental STM image well. The Cation Dimer model shows a periodic intensity change along the $[1\bar{1}0]$, brightening and diming with the anion in the kinked dimer position acting as a bright point along the row. The Mixed Dimer model best reproduces the experimental STM, showing a bright intensity of the anion dimer separated by relatively dim sections along the $[1\bar{1}0]$ due to the height difference between the anion dimer and the surrounding surface. This suggests that the Cation Dimer and Mixed Dimer models are good candidates for the InGaAs-(4x3) reconstruction. However, the energetics of these reconstructions must still be examined.

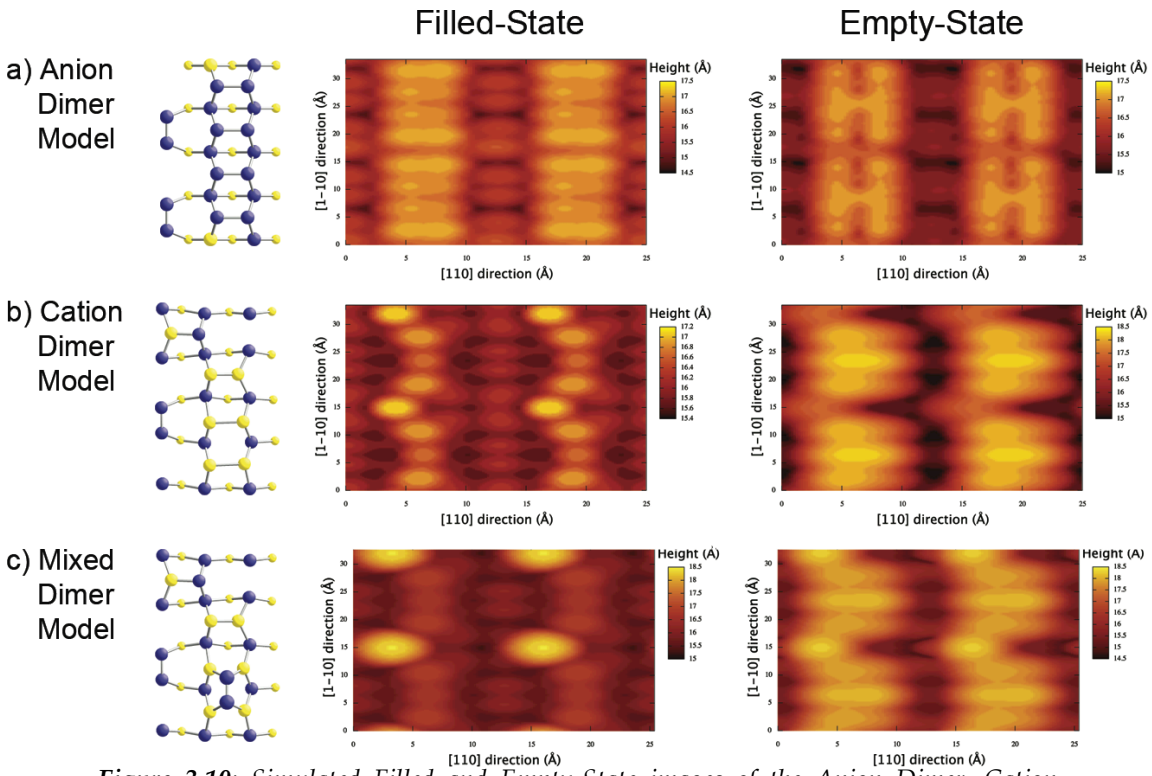

***Figure 3.10**: Simulated Filled and Empty-State images of the Anion Dimer, Cation Dimer, and Mixed Dimer Models.*

In order to analyze the role of strain on the surface stability of the (4x3), computational techniques were utilized. Initial energetic calculations focused on lattice mismatch strain, comparing the three proposed (4x3) models and the α2(2x4), β2(2x4) and c(4x4) reconstructions common to binary InAs and GaAs and the GaSb-(4x3), herein termed the BC model after its developer [23]. The (4x3) is often seen on compressively strained surfaces such as the $In_{0.27}Ga_{0.73}As/GaAs$ and the $In_{0.81}Ga_{0.19}As/InP$ surfaces. For this reason, energies of the proposed models were analyzed for pure InAs at the InAs and InP lattice parameters to examine the role of compressive strain in stabilization of the InGaAs-(4x3). Pure InAs was chosen to avoid any effects of atomic size mismatch strain in the initial study, focusing on lattice mismatch strain only. The results are plotted in Fig. 3.11. These plots show Energy (meV) vs. As chemical potential, μ_{As}, (meV). At any given μ_{As}, the curve with the lowest energy is the stable surface reconstruction. For InAs at the InAs lattice parameter, the expected stability is seen and the stable surface reconstruction with decreasing μ_{As} is the c(4x4), β2(2x4), and α2(2x4) which has been seen experimentally, where μ_{As} corresponds

to decreasing As flux or increasing temperature, and computationally [5]. The distance between cross-over points is also in agreement with previously reported work. For InAs at the InP lattice parameter there are some shifts in the positions of the curves, with the Mixed Dimer and BC model dropping in energy relative to the stable reconstructions, the Cation Dimer model increasing in energy relative to the stable reconstructions, and the cross-over points for the α2(2x4)-β2(2x4) and β2(2x4)-c(4x4) reconstructions shift. However, lattice mismatch strain does not explain the presence of the (4x3) reconstruction in the InGaAs system as the stable reconstructions are still, with decreasing μ_{As}, the c(4x4), β2(2x4), and α2(2x4).

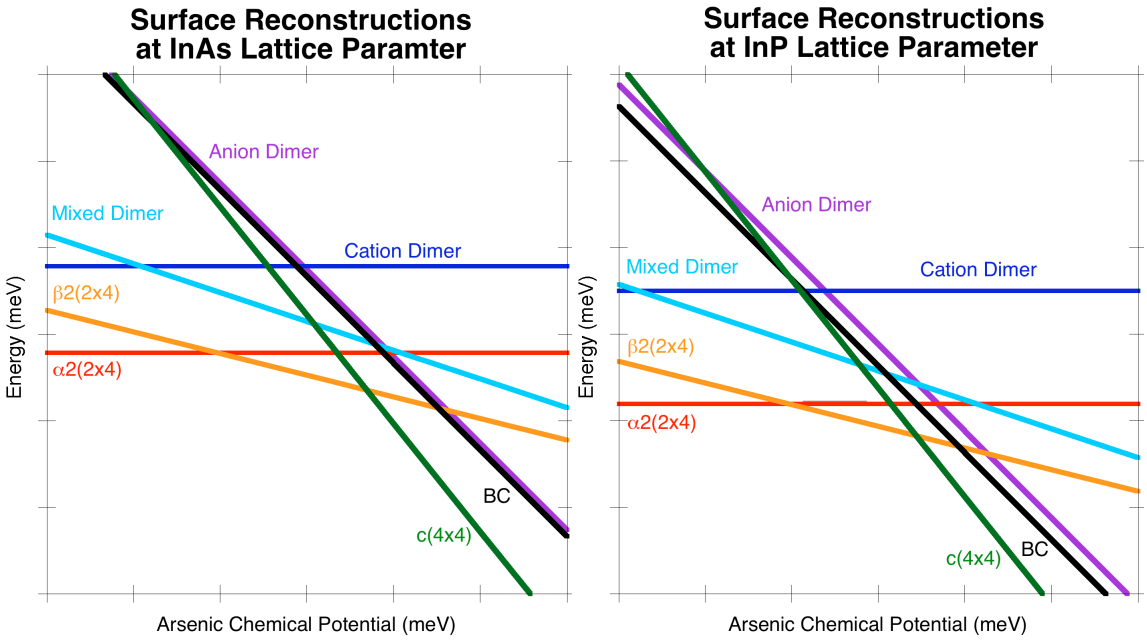

***Figure 3.11**: Energy vs. μ_{As} for different reconstructions at the InAs (left) and InP (right) lattice parameters.*

It is not surprising that lattice mismatch strain does not stabilize the (4x3) reconstruction because, while the (4x3) reconstruction is seen in compressively strained films, it is also seen in the non-strained $In_{0.47}Ga_{0.53}As/InP$ film. Also, the only time that it is reported on its own is for the lattice-matched $In_{0.47}Ga_{0.53}As/InP$ and the nominally unstrained films of Jones *et al.* in the composition range of $0.4 \leq X_{In} \leq 0.8$. This suggests that in fact atomic size mismatch strain may be responsible for the stability of the (4x3) reconstruction. Atomic size mismatch strain was analyzed for the top two layers of cations for the α2(2x4), β2(2x4),

c(4x4), and Mixed Dimer model, resulting in the analysis of 14, 14, 18, and 16 cation positions respectively for the different reconstructions. The Mixed Dimer model was chosen because it has the surface energy closest to that of the stable (2x4) and (4x4) reconstructions. These surfaces were examined at the GaAs lattice parameter because the (4x3) reconstruction appears and coexists with the α2(2x4) for $In_xGa_{1-x}As/GaAs$ films with a very low X_{In} concentration. Structures were determined by inserting In (Ga) into GaAs (InAs) films at the GaAs lattice parameter. A single atom was inserted at all available cation positions. The lowest energy structure was determined. That structure was then used as a starting structure for the next step of the alloying, inserting a second atom into all remaining cation positions, until all possible positions had been filled with the alloying cation. The resulting energies are a function of both μ_{As} and of the difference in chemical potential between the In and Ga cations, $\Delta\mu_{Cation}$ and are shown in Fig. 3.12 along with pure, strained films of the Cation Dimer model and the Anion Dimer model. Due to the 3D nature of this graph, it is projected here from the bottom, and shows only the most stable reconstruction at any μ_{As}-$\Delta\mu_{cation}$ combination. The stable reconstructions, regardless of alloying, are the α2(2x4), β2(2x4) and c(4x4) with increasing μ_{As}, though changing $\Delta\mu_{cat}$ does result in some changes in the cation composition within these structures. The shape of the boundary between the α2(2x4) and β2(2x4) is in agreement with published DFT-MC studies [25]. However, the (4x3) models are not stable at any chemical potential suggesting that atomic size mismatch strain alone may not be able to account for the stability of the (4x3) reconstruction.

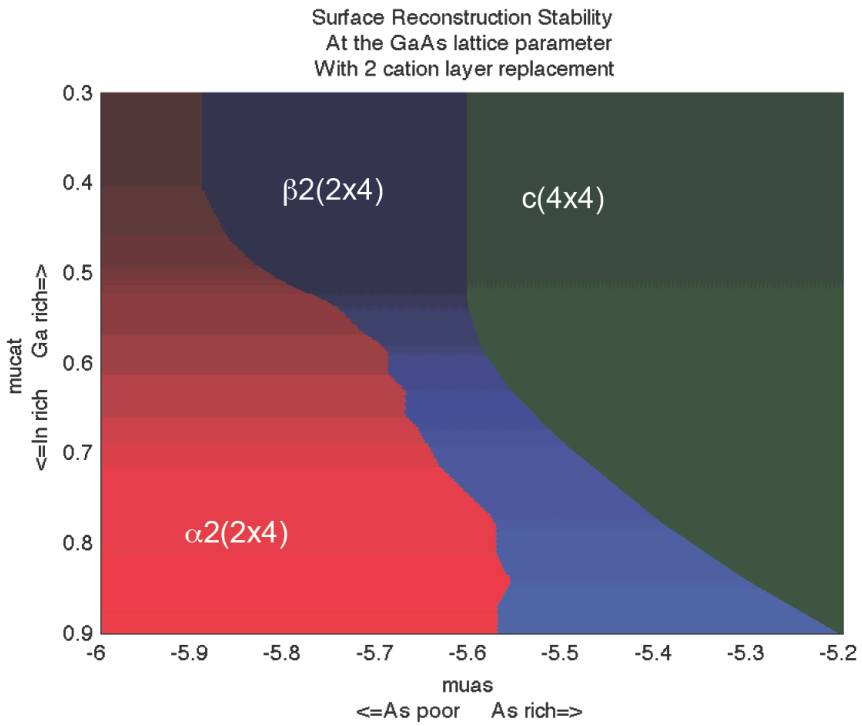

***Figure 3.12**: Lowest energy reconstruction for alloyed InGaAs at the GaAs lattice parameter. Lightening and Darkening of single hues represent different ratios of In:Ga within the reconstruction.*

These results show that atomic size mismatch strain alone is *probably* not responsible for the stability of the (4x3) reconstruction. A few possibilities that might explain why these studies have not yet been successful are:

1. The correct structure for the (4x3) reconstruction has not yet been proposed.

2. Interactions between specific atomic sites must be taken into account more fully.

3. Interactions including *both* lattice mismatch strain *and* atomic size mismatch strain must be taken into account.

4. Disorder may hide the actual reconstruction.

The first point has been somewhat addressed using simulated STM. Examining experimental STM and comparing the Anion Dimer, Cation Dimer, and Mixed Dimer models suggests some characteristics which may be important in determining the actual (4x3) reconstruction. The Anion Dimer model is very high in energy, presumably due to the insertion of a cation onto the anion sublattice. This type of antisite inclusion is typically a very high energy defect,

and the energy decrease due to the reconstruction obeying the ECR and not acquiring a surface charge does not appear to counteract the increase in energy due to the antisite. Also, As surface dimers appear bright under filled-state STM imaging. As the actual STM appears to show a periodic intensity along the $[1\bar{1}0]$, this suggests that the surface does not have a regular backbone of anion dimers. The closer match of the Cation Dimer model and the Mixed Dimer model suggest that either a mixed anion-cation surface or a height difference, or a combination of the two most accurately reproduce the STM intensity seen on the surface. Thus, it would be sensible to examine reconstructions with these features.

The second point raised is not trivial. The number of possible configurations of two atoms on an N site lattice is 2^N. While this is small for small N, the number of cation sites being considered in this study is on the order of 14, resulting in over 16,000 possible configurations. In order to make this more manageable, a method of alloying was chosen that reduces the number of possible configurations to $\sum_{i}^{N} i$ where 14 possible positions results in only 105 possible configurations. While this method is a good way of reducing the numbers of possible alloying structures to a reasonable number, it ignores the possibility that the lowest energy two-atom structure does not include the lowest energy one-atom structure. The data shows that this may be an important consideration because a low energy position in one iteration may be a much higher energy position in the next iteration due to the placement of a cation in an adjacent position. Previous work on In surface segregation and pair interactions for InGaAs in the β2(2x4) reconstruction shows a wide range of pair interactions changing from attractive to repulsive depending on the pair distance [22]. However, while this point is not trivial, the method of *how* to include all these interactions while limiting the sampling set to a reasonable number remains a difficult problem.

The interaction between lattice mismatch and atomic mismatch strain may be trivial to the stabilization of the (4x3) reconstruction. The fact that the (4x3) reconstruction appears at a wide variety of lattice strains (0-2%) suggests that

lattice mismatch strain is not playing a large role in stabilization of the (4x3) surface structure. It is possible that large (>2%) strains induced on the surface due to coexistence. The (4x3) coexists with (2x4) reconstructions according to both Millunchick and Placidi [9, 13] and with the c(4x4) according to Jones [10] at nominally unstrained low In content films. Elastic relaxation at domain borders may induce a surface lattice mismatch strain where adjacent domains having opposite sign strain. This may also be due to atomic mismatch strain due to the hypothesis that In may preferentially segregate to one reconstruction on the surface [16]. Yet, as the (4x3) reconstruction is seen when InGaAs is lattice matched to InP, this interaction of strains cannot account for all manifestations of the (4x3) reconstruction.

The idea that disorder may hide the actual (4x3) reconstruction is also not trivial. In both the Cation Dimer and Mixed Dimer models the kinked dimer may change positions within the unit cell, as long as the kink appears somewhere in the cell. This variation would induce no energy change in the surface as the energies of the different configurations would be degenerate (assuming no interaction energy between kinked dimers). This could induce a large amount of disorder along the $[1\bar{1}0]$ and would explain why the RHEED patterns appears as a (1x3) rather than a (4x3). It is also possible that the unit cell is not actually a (4x3). While it is generally thought to have a 4x periodicity along the $[1\bar{1}0]$, there is a lot of disorder in all the experimental STM from different groups. This suggests that the unit cell may be either larger or smaller and the actual periodicity is disguised by the amount of disorder on the surface.

iv. Conclusions

The InGaAs work shown here examines the structure of the $In_{0.27}Ga_{0.73}As/GaAs$ surface, which displays a *coexistence* of two surface reconstructions. This coexistence was originally termed a (4x3)-α2(2x4) coexistence, but the α2(2x4) unit cell displays a regular ordering where the dimer alternates between two positions in adjacent unit cells. Thus, this structures is better termed a z(4x4) reconstruction or an ordered α2(2x4) reconstruction. DFT results clearly indicate that this ordering is due to placement of In in the surface

unit cell inducing a regular ordering of the anion dimer in the α2(2x4) reconstruction. Therefore, it is necessary to examine the placement of alloyed atoms on the surface and take atomic size mismatch strain into account when analyzing alloy surfaces. This is important because, while the structure of the reconstruction has been known to influence alloy placement within the bulk structure, this is the first time that alloying has been proven to impact the *atomic structure of the surface reconstruction*. This shows that it is vitally important to consider atomic size mismatch strain when analyzing the surface structures of alloyed reconstruction and this has already been taken up by Thomas *et al.* who further examine the ordering of the z(4x4) structure, examining the As dimer concentration and ordering on the (2x4) surface as a function of In concentration utilizing Monte Carlo methods fit to DFT energies [25].

This work also analyzes the structure of the (4x3) reconstruction and its stability as a function of lattice mismatch and atomic size mismatch strain. The structure of the (4x3) reconstruction remains unconfirmed, though the work here suggests certain features, such as a high surface anion dimer, or a cation rich surface with a single anion, which are likely part of the actual reconstruction. Four possible explanations for the remaining mystery surrounding the (4x3) reconstruction are discussed. Some suggestions for future work are: (1) utilize a cluster fit MC simulation to analyze the cation pair interactions in the first two cation layers in order to better drive atomic size misfit strain studies within this system, and (2) examine the interaction energy between kink dimers at different distances to better understand the impact this interaction may have on surface disorder.

Overall, this chapter shows the importance of atomic size mismatch strain in the study of alloyed surface reconstructions. It also shows that while this strain interaction energy is important, it does not alone explain all the surface phenomena unique to alloyed reconstructions surfaces, and that future studies into competing interactions of strain and chemistry are important to fully understand the complexity of this alloyed system.

v. References

1. Y. L. Wang, H.-J. Gao, H. M. Guo, H. W. Liu, I. G. Batyrev, W. E. McMahon, and S. B. Zhang, *Phys. Rev. B* **70**, 073312 (2004).
2. J. Z. Liu, G. Trimarchi, and A. Zunger, *Phys. Rev. Lett.* **99**, 145501 (2007).
3. F. J. Effenberger, and M. J. Abhay, *Proceedings of the SPIE* **3380**, 144 (1998).
4. M. A. Tischler, T. Katsuyama, N. A. El-Masry, and S. M. Bedair, *Appl. Phys. Lett.* **46**, 294 (1985).
5. W. Barvosa-Carter, R. S. Ross, C. Ratsch, F. Grosse, J. H. G. Owen, and J. J. Zinck, *Surf. Sci.* **499**, L129 (2002).
6. V. P. LaBella, H. Yang, D. W. Bullock, P. M. Thibado, P. Kratzer, and M. Scheffler, *Phys. Rev. Lett.* **83**, 2989 (1999).
7. H. Yamaguchi, and Y. Horikoshi, *Phys. Rev. B* **51**, 9836 (1995).
8. M. Sauvage-Simkin, Y. Garraeu, R. Pinchaux, A. Cavanna, M. B. Vernon, N. Jedrecy, J. P. Landesman, and J. Nagle, *Appl. Surf. Sci.* **104**, 646 (1996).
9. J. Mirecki Millunchick, A. Riposan, B. Dall, C. Pearson, and B. Orr, *Surf. Sci.* **550**, 1 (2004).
10. P. A. Bone, J. M. Ripalda, G. R. Bell, and T. S. Jones, *Surf. Sci.* **600**, 973 (2006).
11. J. C. Thomas, Unpublished Work (2009).
12. A. Riposan. "Surface Reconstructions and Morphology of InGaAs Compound Semiconductor Alloys," University of Michigan, Ann Arbor, 2004.
13. F. Patella, A. Sgarlata, F. Arciprete, S. Nufris, P. D. Szkutnik, E. Placidi, M. Fanfoni, N. Motta, and A. Balzarotti, *J. Phys. Condens. Matter* **16**, S1503 (2004).
14. L. E. Sears, J. M. Millunchick, and C. Pearson, *J. Vac. Sci. Techol. B* **26**, 1948 (2008).
15. R. M. Tromp, and J. B. Hannon, *Surf. Rev. and Lett.* **9**, 1565 (2002).
16. A. Riposan, J. M. Millunchick, and C. Pearson, *J. Vac. Sci. and Tech. A* **24**, 2041 (2006).
17. C. Ratsch, *Phys. Rev. B* **63**, 161306 (2001).
18. R. H. Miwa, R. Miotto, and A. C. Ferraz, *Surf. Sci.* **542**, 101 (2003).
19. G. R. Bell, M. Itoh, T. S. Jones, B. A. Joyce, and D. D. Vvendensky, *Surf. Sci.* **433**, 455 (1999).
20. P. Laukkanen, M. Kuzmin, R. E. Perala, M. Ahola, S. Mattila, I. J. Vayrynen, and J. Sadowski, *Phys. Rev. B* **72**, 045321 (2005).

21. A. Bosacchi, F. Calonna, S. Franchi, P. Pascarella, P. Allegri, and V. Avanzini, *J. Cryst. Growth* **150**, 185 (1995).

22. J. H. Cho, S. B. Zhang, and A. Zunger, *Phys. Rev. Lett.* **84**, 3654 (2000).

23. W. Barvosa-Carter, A. S. Bracker, J. C. Culbertson, B. Z. Nosho, B. V. Shanabrook, L. J. Whitman, H. Kim, N. A. Modine, and E. Kaxiras, *Phys. Rev. Lett.* **84**, 4649 (2000).

24. J. Tersoff, and D. R. Hamann, *Phys. Rev. B* **50**, 1998 (1983).

25. J. C. Thomas, J. M. Millunchick, N. A. Modine, and A. Van der Ven, *Phys. Rev. B* **80**, 125315 (2009).

Chapter IV

The Development of Lattice Mismatch Strained Surface Reconstructions

Globally applied strain may induce bulk crystal changes from one structure to another due to differences in atomic packing factors. In thin film growth, the stress induced by the difference in lattice parameter is known to deflect a cantilever by an amount proportional to the applied stress. Chapter III examined InGaAs films, focusing on the effect of point atomic size mismatch strain on surface atomic ordering and reconstruction stability. The interactions between the point strain due to alloying and the displacement strain due to the formation of the surface reconstruction were shown to interact and induce a surface dimer ordering in the α2(2x4) reconstruction. Chapter IV examines the interactions between global lattice mismatch strain and a surface reconstruction particularly focusing on the effects of lattice mismatch strain on surface reconstruction stability. The mixed anion system GaSb/GaAs is the model system.

i. Understanding the GaSb/GaAs Surface

A fair amount of previous research has examined GaSb/GaAs, a materials system that is technologically important for a number of different devices. Some example are the stacking of GaSb and GaAs for use in tandem solar cells [1] and concentrator arrays with InGaP [2].

GaSb/GaAs films exhibit a 7% lattice mismatch strain which typically results in SK growth with a critical thickness, h_c, between 2.5 and 3ML [3]. These QD structures have been studied by multiple groups to examine QD size, shape, density, and defects [3-6]. More important to film growth, however, is the sub-critical thickness surface layers which control atomic incorporation of GaSb on the surface and which may influence defect formation and film growth.

Generally, it is accepted that GaSb grown by homoepitaxy exhibits a (4x3) reconstruction by STM that corresponds to a (1x3) pattern on RHEED [7]. This is due to disorder along the $[1\bar{1}0]$ which alters the periodicity of the structure along this direction, disrupting the regularity of the x4 periodicity. Sub critical thickness films of GaSb/GaAs have been shown to have either a (2x4) or (2x8) pattern [8, 9] neither of which are not seen in the unstrained film. However, the exact structure of the (2x8) reconstruction has been contentious, and in the course of this study, it is shown that the (2x4) reconstruction is not a single reconstruction covering the surface but rather a coexistence of the (2x4) with a (4x3) surface reconstruction. The RHEED pattern is defined only by the (2x4) because it covers a larger percent of the surface.

The surface reconstruction in homoepitaxial films is determined by the competing interactions of (1) local chemistry, (2) local displacement strain, and (3) the ECR [10]. In strained films, strain adds a fourth factor to this. This chapter analyzes the basic structure of the (2x4)-(4x3) and (2x8) alloy surface reconstructions. However, the surface reconstruction, film growth, and surface atomic incorporation, which impact the strain field, are also impacted by the surface kinetics of the system. The surface kinetics are determined by the growth temperature, flux rate, and flux ratio and so these factors are examined in order to fully characterize the factors influencing this alloy surface. Specifically, this chapter examines the effects of:

- Film thickness
- The presence of anion flux during cooling
- The presence of cation flux during growth
- Anion flux rate during growth

These different parameters are discussed below in relation to their impact on the surface reconstruction of GaSb/GaAs. Specifically, it is shown that three different surface structures can be obtained by altering the film thickness and the anion overpressure. The presence of a cation flux alters the ratio of two coexisting surface structures while the anion flux has little impact on this structure.

ii. Surface Development of Lattice Mismatched Films: GaSb/GaAs

a. *The Three Surface Reconstructions of GaSb/GaAs*

Very thin films of GaSb can be formed by exposing a GaAs surface to an Sb flux of atoms which replace the As atoms near the surface due to anion exchange. Surface anion exchange is impacted by a number of factors, including the relative overpressures of the anions, the bond strength of the cation to the different anions, surface migration rates, and the surface reconstruction [11]. However, these factors only influence the amount and rate of exchange [11]. Thus, thin films can be grown below the critical thickness for SK islanding. The resulting films show three distinct structures:

- Submonolayer mottled films
- Mixed surface reconstruction films
- (2x8) reconstruction films

Each of these structures will be examined in detail.

Submonolayer-thick films of Sb/GaAs were grown with Sb exposure times of $t < 2.2$ s. This correlates to $h < 0.8$ ML assuming all anions are incorporated into the film. Prior to exposure to the Sb flux, a sharp (2x4) RHEED pattern is obtained. The x4 pattern on the $[1\bar{1}0]$ azimuth sharpens during annealing when the As shutter closes then dims when the Sb shutter opens, with the (0, 1/2) line disappearing relative to the background intensity. The (0, 1/4) and (0, 3/4) lines dim as well, but rarely disappear. Upon completion of the Sb exposure, the RHEED pattern quickly returns to a (2x4) reconstruction as seen in Fig. 4.1a. During cooling to 200°C under no Group V flux, the pattern changes to the (2x3) shown in Fig. 4.1b. This pattern is similar to the (1x3) RHEED pattern associated with the (4x3) reconstruction of bulk GaSb [7]. The spacing between

the lines in the RHEED pattern in Fig. 4.1b is not exact, with the (0, 1/3) and (0, 2/3) lines closer to the primary azimuths than to each other. This uneven fractional spacing in the RHEED pattern has been called "incommensurate" and suggests surface disorder where two variations of a reconstruction coexist [12]. Observations by RHEED are supported by STM, which is shown in Fig. 4.1c and exhibits a mottled and disordered surface.

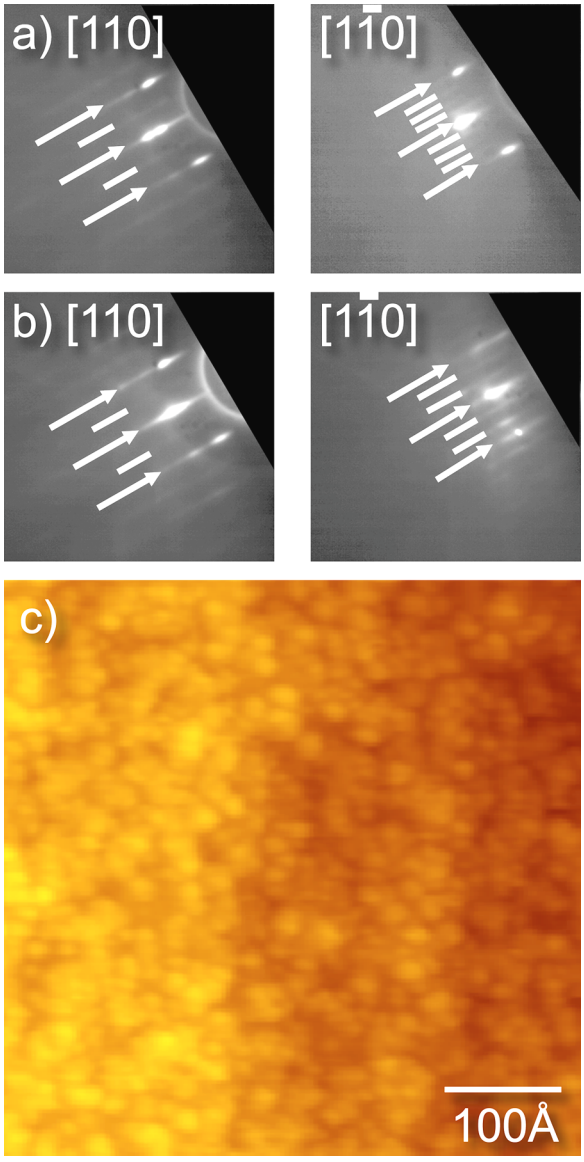

***Figure 4.1**: RHEED and STM of t=1.4s (0.5ML) Sb/GaAs. (a) [110] and [1$\bar{1}$0] RHEED patterns just after Sb exposure, (b) [110] and [1$\bar{1}$0] RHEED patterns upon cooling, and (c) STM of the surface taken at I=100pA and V=-4.7V.*

Thicker films of Sb/GaAs show a very similar RHEED pattern development, as can be seen for the t=2.2s growth in Fig. 4.2a. Similar to the

thinner films, the fractional RHEED lines dim during Sb exposure, indicating disorder on the surface during growth. Along the [110] direction, the (0,1/2) line dims but never disappears, thus retaining a periodicity of x2 during growth. Along the $[1\bar{1}0]$, all fractional lines dim and broaden somewhat. The (0, 1/2) sometimes disappears, resulting in a periodicity of 3 or 4 along this direction. As for the disordered films, the x3 spacing is not consistent; the (0, 1/3) and (0, 2/3) lines sitting at (0, 1/4) and (0, 3/4) instead. This suggests surface disorder on the surface or the possibility of multiple surface reconstructions [12] as has been seen in InGaAs films [13, 14]. Regardless of whether the pattern appears as a (2x4) or an incommensurate (2x3) during Sb exposure, a (2x4) pattern is quickly obtained upon closing the Sb valve (Fig. 4.2a) and retained upon cooling the film (Fig. 4.2b). STM (Fig. 4.2c) shows that the surface is indeed comprised of two reconstructions, with one reconstruction covering most of the surface, while another reconstruction of intermediate height appears at step edges.

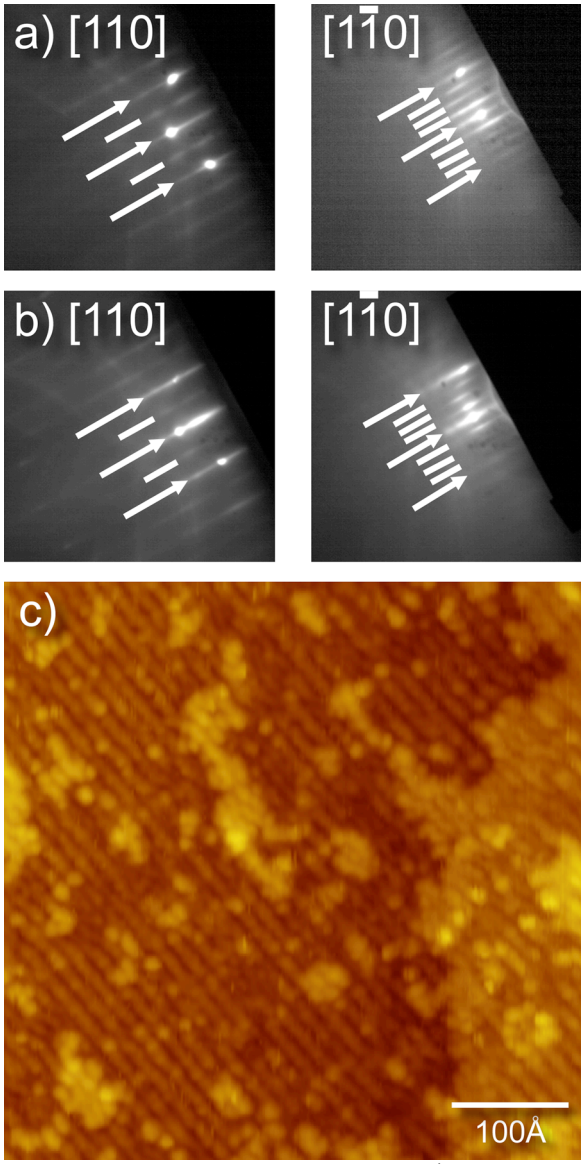

Figure 4.2: *RHEED and STM of t=2.2s (0.8ML) Sb/GaAs. (a) [110] and* [1$\bar{1}$0] *RHEED patterns just after Sb exposure, (b) [110] and RHEED patterns upon cooling, (c) STM of the surface taken at I=100pA and V=-3.38V.*

A high resolution image of the mixed reconstruction surface can be seen in Fig. 4.3. The majority surface reconstruction is the α2(2x4), in agreement with the observed RHEED pattern. It consists of a single anion dimer atop six cations, with neighboring cells separated along the [110] by trench anion dimers [15], illustrated schematically in Fig. 4.4. This reconstruction is not typical for bulk GaSb, though it is a common reconstruction for GaAs, and (2x4) reconstructions have been reported for Sb capped GaAs [8, 9, 16, 17]. The rows are spaced 14.6Å apart, which is in good agreement with a 4a spacing where a=3.94Å is the in-

plane lattice parameter. The second reconstruction, which is not evident in the RHEED patterns presumably due to its low surface coverage (~25%), appears predominately at step edges and consists of rows in the $[1\bar{1}0]$ spaced at 11.2 ± 0.6 Å, or three times the in plane spacing of GaAs, suggesting an (nx3) reconstruction. This (nx3) appears to be of intermediate height, 1.3Å above and below the adjacent α2(2x4) terraces, as can be seen in Fig. 4.3b. The combination of row spacing and height, nominally one atomic layer difference relative to adjacent α2(2x4) terraces, suggests that this is one of the (4x3) reconstructions stable for bulk GaSb, the α(4x3) or β(4x3) that have been previously described [7]. These reconstructions consist of a $[1\bar{1}0]$ row of surface dimers with every fourth dimer displaced by a single bulk spacing in the [110]. Adjacent surface cells are separated in the [110] by a trench anion dimer, as can be seen in Fig. 4.4.

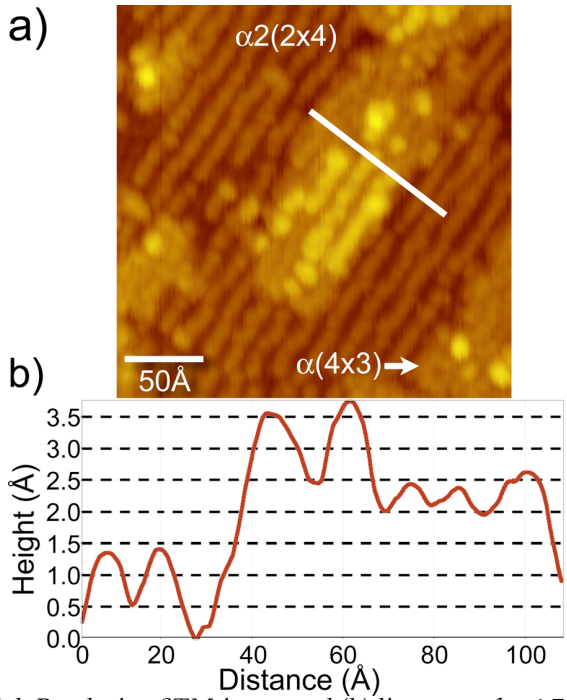

Figure 4.3: *(a) High Resolution STM image and (b) line scan of t=4.7s (h~1.7ML) taken at I=100pA, V=-4.33V. Regions of the α(4x3) and α2(2x4) reconstructions are marked and the line scan shows the height difference between the two reconstructions.*

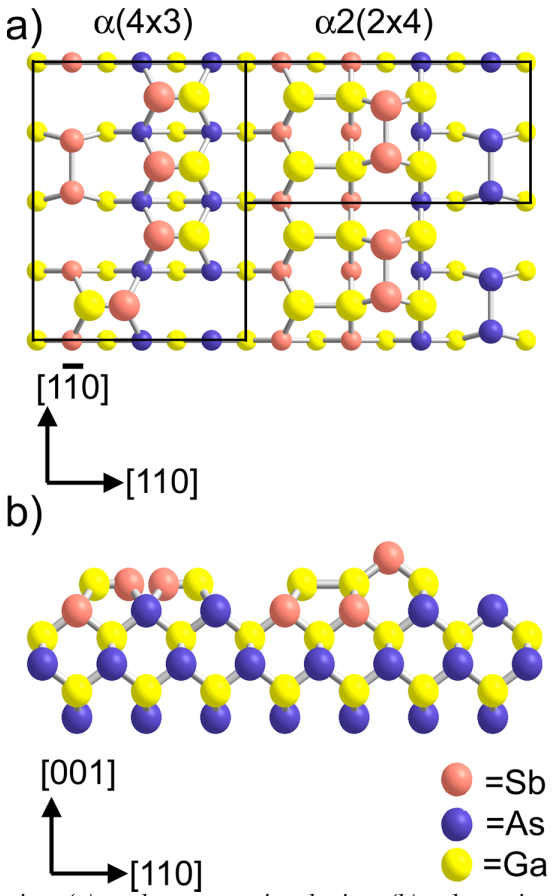

Figure 4.4: *Plane-view (a) and cross-sectional view (b) schematics of the α(4x3) and α2(2x4) reconstructions.*

The specific nature of the (nx3) reconstruction may be determined by additional STM measurements. The difference between the α(4x3) and β(4x3) surface structures is in the composition of the dimer row in the topmost layer. In the β(4x3), the topmost layer consists of anion dimers with a kinked anion-cation heterodimer. In the α(4x3), it consists entirely of heterodimers. The surface composition of the (4x3) structures observed in our films can be determined using dual bias imagery, in which filled anion dangling bonds appear bright in negative bias while empty cation dangling bond appear bright in positive bias. Analysis of the α2(2x4) areas (Fig. 4.5 rectangles) confirm this reconstruction is anion terminated, as it appears bright in the negative bias and dim in the positive bias images, in agreement with the model shown in Fig. 4.4. Some regions of the α2(2x4) appear to be darker in both the forward and reverse bias images. This may be due either to the presence of As in the surface, which would lower the intensity because GaAs has a larger band gap than GaSb, or other defects in the

surface reconstruction, which result in a change in the local density of states and thus the relative intensity. The (4x3) reconstructed areas (circled in Fig. 4.5) show the domains are relatively bright under both negative and positive bias, suggesting this is the α(4x3) reconstruction comprised of surface heterodimers. The disorder seen in Figs. 4.2c and 4.3a can also be easily explained by the structure of the α(4x3), as the kinked dimer may sit in any of the surface dimer positions without disrupting surface charge neutrality. The α(4x3) appears predominately at step edges. In these films (Figs. 4.2, 4.3, 4.5) there are many small islands which exhibit only the α(4x3) reconstruction and larger islands which exhibit a mixed α(4x3)-α2(2x4) reconstruction. Analysis of the STM images at t=2.2 and 4.7s yields a critical island area of 30±10nm2 below which islands are comprised solely of the α(4x3) reconstruction, and above which they exhibit the mixed character.

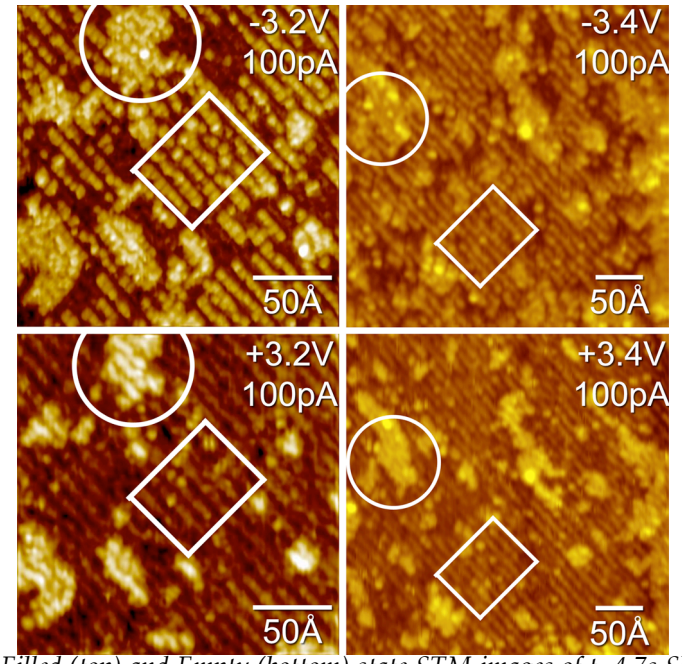

Figure 4.5: *Filled (top) and Empty (bottom) state STM images of t=4.7s Sb/GaAs. The circles show areas of α(4x3) reconstruction and the rectangles show areas of α2(2x4) reconstruction.*

The α2(2x4)-α(4x3) reconstruction is present under long exposure times to Sb. Longer exposure time of the surface to a flux of Sb results in more of the GaAs being converted to GaSb until the near-surface As is depleted. Films exposed to Sb for 2.2 ≤ t ≤ 27.8s exhibit the mixed α2(2x4)-α(4x3) surface reconstruction upon cooling and, with the exception of the t=27.8s sample, show

RHEED development as in Fig. 4.2a. The t=27.8s sample changes towards the end of growth from the diffuse pattern to a (2x8) reconstruction comprised of a double layer of Sb, which has been reported for high Sb overpressures [8, 9]. After the Sb flux is removed, this sample quickly returns to the (2x4) reconstruction, which it retains upon cooling in the absence of a Group V flux. The result is that samples of $t \geq 2.2s$ exhibit a mixed (2x4)-(4x3) reconstruction as described for Fig. 4.2.

The (2x8) reconstruction appears for very thin layers of GaSb on GaAs grown under Sb rich conditions, as just described. Cooling this surface in the absence of an Sb overpressure causes the reconstruction to quickly revert to the mixed (2x4)-(4x3) structure. Cooling this surface under a small Sb overpressure, $R_{Sb\text{-}Cool} \approx 0.5 * R_{Sb\text{-}Growth}$, however, results in a stabilization of the (2x8) reconstruction. The growth begins as previously, with the fractional lines dimming slightly. Upon completion of the exposure and reduction of the Sb flux to R_{Sb}=1.5ML/s, the (2x4) pattern is not recovered, but the fractional lines resolve into a (2x8) pattern (Fig. 4.6a) that is retained upon cooling (Fig. 4.6b). The resulting STM shows a (2x8) reconstruction, in agreement with published results [8, 9]. Figure 4.7 shows a more detailed structural view of the surface, including a line scan in Fig. 4.7c. The (2x8) reconstruction consists of straight rows of atoms along the $[1\bar{1}0]$ direction. These rows are spaced regularly along the [110] at 32Å, as can be seen in Fig. 4.7c, corresponding to a periodicity of 8 times the bulk in-plane lattice parameter a_0, where a_0 is between the GaAs and GaSb lattice parameters. A line scan across the reconstruction rows shows very little structural detail, only an approximately sinusoidal variation in apparent height. There is a slight amount of disorder on the surface where the rows diverge and recombine, which is likely due to quenching the sample without additional annealing. Similar disorder appears in the STM images by Whitman *et al.* [9], though not in those by Laukannen *et al.* [8]. This suggests the disorder may be thermally unstable and anneal out under long Sb exposures.

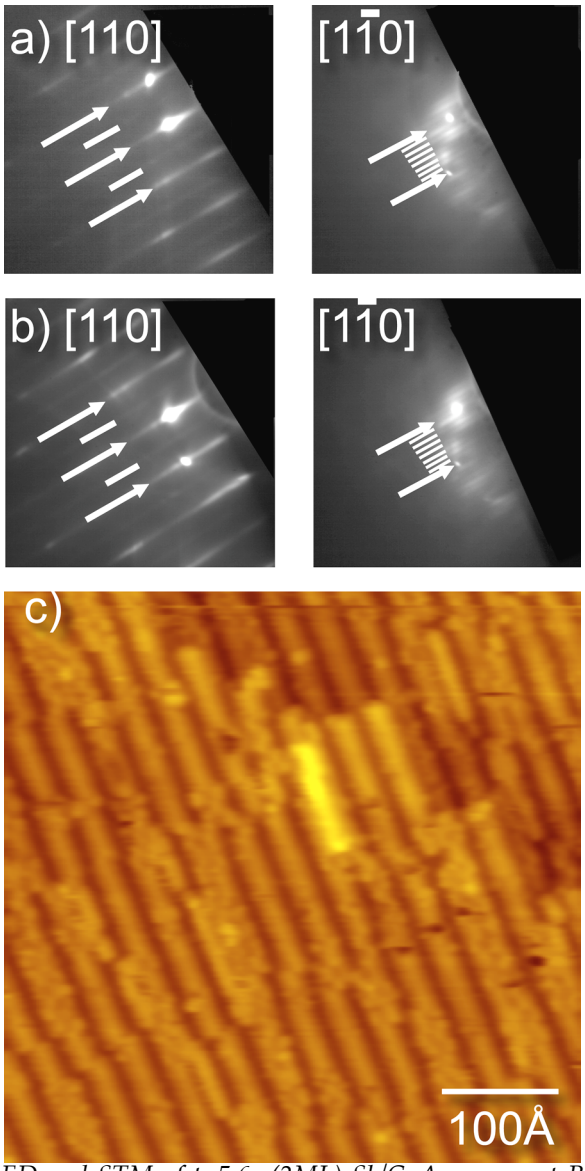

Figure 4.6: *RHEED and STM of t=5.6s (2ML) Sb/GaAs grown at R_{Sb}=0.36ML/s and cooled under R_{Sb}=1.5ML/s. (a) [110] and* $[1\,\bar{1}\,0]$ *RHEED patterns just after reducing Sb flux, (b) [110] and* $[1\,\bar{1}\,0]$ *RHEED patterns upon cooling, and (c) STM of the surface taken at I=100pA and V=-3.43V.*

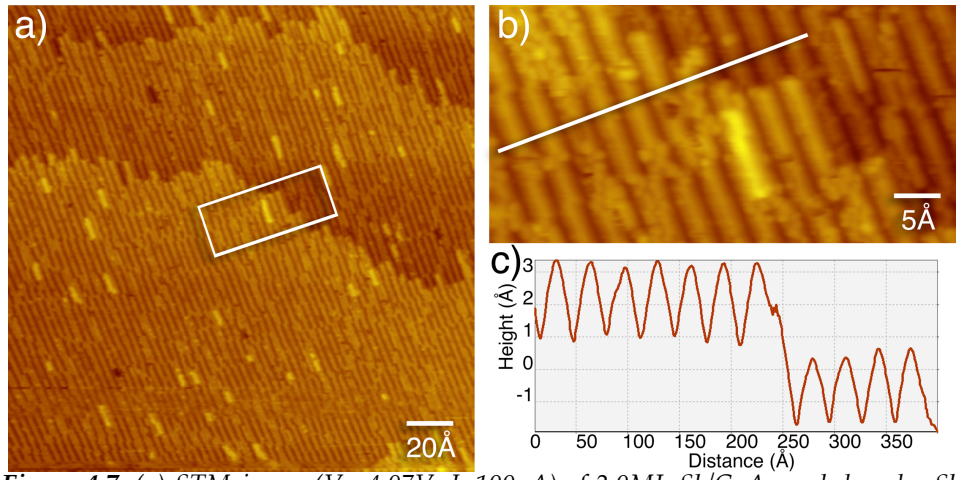

Figure 4.7: *(a) STM image (V=-4.07V, I=100pA) of 2.0ML Sb/GaAs cooled under Sb flux to form the (2x8) reconstruction. (b) High resolution portion of the image in (a). (c) A line scan across the line indicated in (b).*

b. *The Effect of Sb Saturation on GaSb/GaAs Film Development*

The reversion to the mixed surface reconstruction under no Sb flux suggests that desorption of Sb from the (2x8) reconstructed surface occurs because the group V species are quite volatile. These observations are consistent with the notion that the (2x8) reconstruction contains excess Sb [8, 9, 18] and the idea that the surface is saturated with Sb.

Examination of the 2D mixed reconstruction island coverage as a function of these films provides insight into the surface Sb saturation in this system. Two dimensional film growth occurs by a few growth mechanisms. One possibility is step-flow growth such as is seen in Si, where atoms adsorb at terrace edges and fill in a step. A second possibility is island nucleation and growth where 2D islands nucleate on the film surface, grow, and coalesce to form a new layer such as seen in this system. Two maxima 2D island coverages occur at t~2.2s (h~0.8ML) and t~5s (h~1.8ML) as seen in Figure 4.8. Above t~5.6s (h~2ML), the 2D island coverage remains constant around 18%. The fact that the number of 2D islands remains constant suggests that there is no further incorporation of Sb into the surface beyond t=5.55s (h~2ML). This, combined with the (2x8) RHEED of the t=27.8s (h~10ML) sample suggests that Sb initially incorporates on the surface in the mixed (4x3)-(2x4) reconstruction, then reaches a point beyond which, without a Ga flux, no more Sb can be incorporated into the surface. The excess Sb is taken up by transforming the surface to the Sb-rich (2x8) reconstruction. Upon cooling in the absence of a Group V overpressure, Le

Chatelier's Principle dictates that the excess Sb taken up by the (2x8) reconstruction be released, and the surface reverts to the mixed reconstruction. This is supported by the fact that the (2x8) reconstruction can be obtained for thinner films cooled under an Sb overpressure.

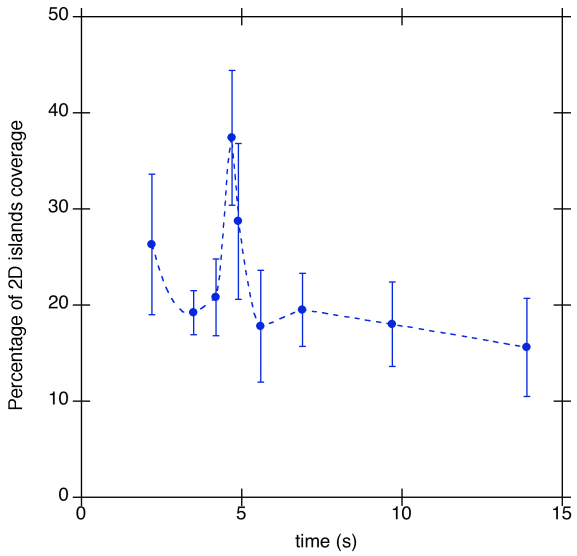

Figure 4.8: *Plot of 2D island coverage vs. Sb exposure time for Sb/GaAs films. Note: t < 2.2s and t > 27s cannot be plotted due to surface reconstruction changes. Dotted line provided as a guide to see peaks and valleys.*

c. *The Intersection between Kinetics and Thermodynamics*

When fluxes of both Ga and Sb are provided, the resulting surfaces also exhibit the (2x4)-(4x3) surface reconstruction coexistence as seen in Fig. 4.9. Films of GaSb/GaAs of thickness $0.25 \leq h \leq 3.0$ML were grown to examine the role of Ga on the surface structure. For GaSb/GaAs, the transition from incommensurate (1x3) to commensurate mixed reconstruction is not seen. Instead, all samples with $h \leq 2.5$ ML exhibit the mixed surface reconstruction, with the α(4x3) appearing exclusively in the vicinity of step edges. Above 2.5ML, the film transitions to 3D quantum dot growth, in agreement with values reported in the literature [3]. An examination of the wetting layer surrounding these dots, shown in the inset of Fig. 4.9f, reveals a film that greatly resembles the incommensurate Sb/GaSb layer seen in Fig. 4.1b, suggesting that upon QD nucleation, wetting layer material diffuses and incorporates into the QDs, resulting in an ultra-thin (<1ML) wetting layer.

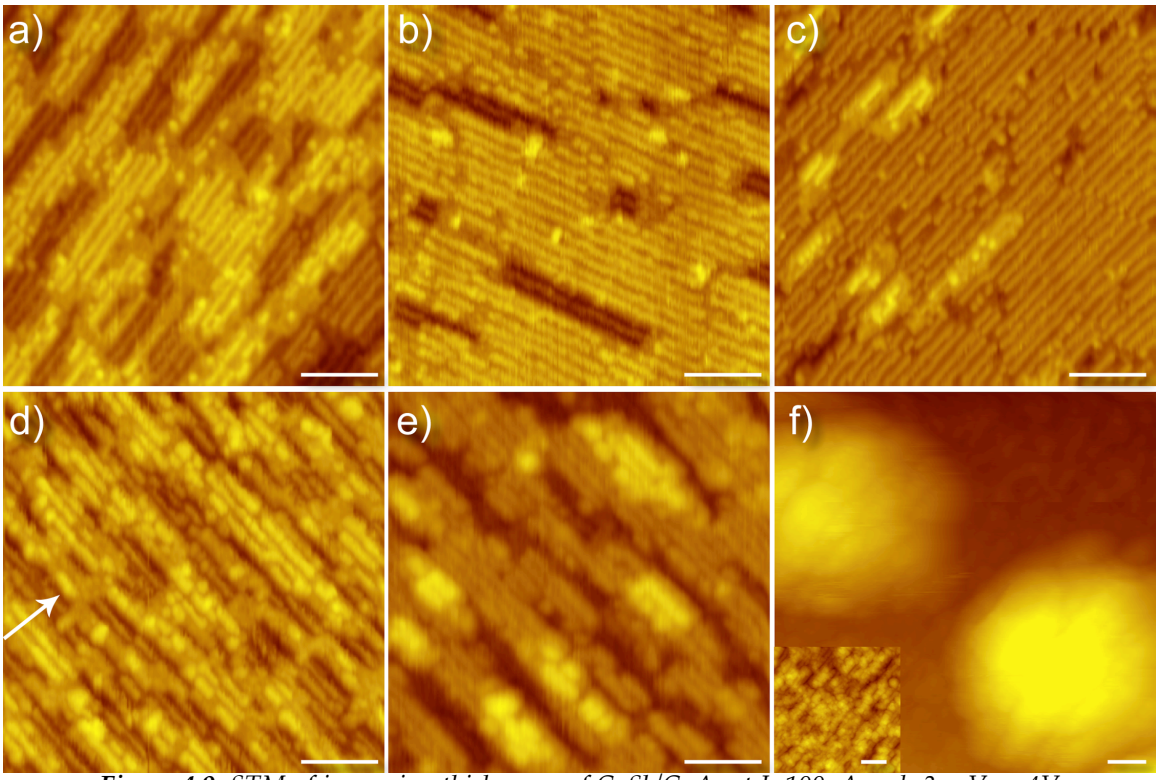

Figure 4.9: *STM of increasing thicknesses of GaSb/GaAs at I=100pA and -3 ≤ V ≤ -4V (a) 0.5ML, (b) 0.75ML, (c) 1ML, (d) 1.5ML, (e) 2ML, (f) 3ML showing QDs with inset of wetting layer. Scale bar is 100Å in all images. The arrow in (d) shows the directionality of the α(4x3) coverage that always appears at step edges along the* $[1\bar{1}0]$ *and typically, but not always, along the [110].*

While both the Sb/GaAs films and the GaSb/GaAs films exhibit a mixed surface reconstruction, there is an important difference in the morphology of these two films. In the Sb/GaAs films, the surface is covered by distinct 2D islands that coalesce with increasing thicknesses. Figure 4.9 shows that the GaSb/GaAs films form as interconnected terraces with holes. The α(4x3) still forms at the terrace edges, but distinct 2D islands are rarely seen, only appearing when a new layer nucleates as in Fig. 4.9c. This difference suggests that Ga provided by the growth flux is playing an important role in the morphological evolution of these films. In the GaSb/GaAs films, Ga is present in the deposition stream and so is available across the entire sample surface. In the Sb/GaAs films, Ga is only available to form GaSb by detaching from step edges or when Sb directly replaces As. Thus in the GaSb films, the Sb has a shorter diffusion length before incorporation than in the Sb films, resulting in smaller, interconnected mesas rather than widely spaced compact islands.

The presence of Ga in the flux further impacts the relative amounts of the α2(2x4) and α(4x3) reconstructions on the surface. Examination of Fig. 4.4 shows that the α2(2x4) reconstruction requires more Ga per unit area than the α(4x3) reconstruction: 3/4 Ga atom per 1x1 unit cell in the α2(2x4), compared to only 1/3 Ga atom per 1x1 cell in the α(4x3). This means that the transformation from α(4x3) to α2(2x4) in the Sb/GaAs system is limited by the amount of Ga present. Figure 4.10 plots the percentage of the surface covered by the α(4x3) reconstruction as a function of the number of GaSb and Sb monolayers deposited on the surface. Fig. 4.11 shows a surface development model with STM images taken from previous figures. Initially the film is a flat α2(2x4) surface. As GaSb is deposited, small 2D islands of α(4x3) reconstruction nucleate, transforming to the mixed surface reconstruction at the critical island size of 30nm^2. These islands grow and coalesce into a full monolayer with minimal step edges thus returning to a flat α2(2x4) reconstruction, and this process repeats for the next monolayer. Thus the amount of α(4x3) on the surface is minimized at an integer number of MLs up until the critical thickness. This is true for GaSb/GaAs films as can be seen in Fig. 4.10. However, for the deposition of Sb in the absence of a Ga flux, the minimum coverage of α(4x3) occurs at a higher thickness, 1.25ML, and the absolute coverage is somewhat higher (15% compared to 9% for the GaSb films), suggesting that the lack of Ga limits the transition from α(4x3) to α2(2x4) in the 2D islands. The lack of Ga could be attributed to either a lack of a Ga flux, or a Ga surface diffusion rate that is low enough to keep the Ga from reaching the islands to facilitate the transformation. However, Ga diffusion rates have been shown to increase in the presence of Sb [19], suggesting that Ga diffusion is not limiting the α(4x3)-α2(2x4) transformation. Examination of the surface as a function of Sb flux rate shows little changes. Table 4.1 shows the amount of α(4x3) present on the surface for h=0.8ML Sb/GaAs grown as a function of Ga deposition rate. The amount of α(4x3) on the surface shows little difference as a function of growth rate compared to the standard deviation of the measurement. If Ga diffusion is limiting the transformation from the α(4x3) to the α2(2x4) reconstruction, there should be a marked increase in α(4x3) coverage for increasing R_{Sb}. Thus, it is the presence of Ga in the flux stream, rather than

Ga diffusion on the surface, that limits the transformation of the α(4x3) reconstruction to the α2(2x4) reconstruction.

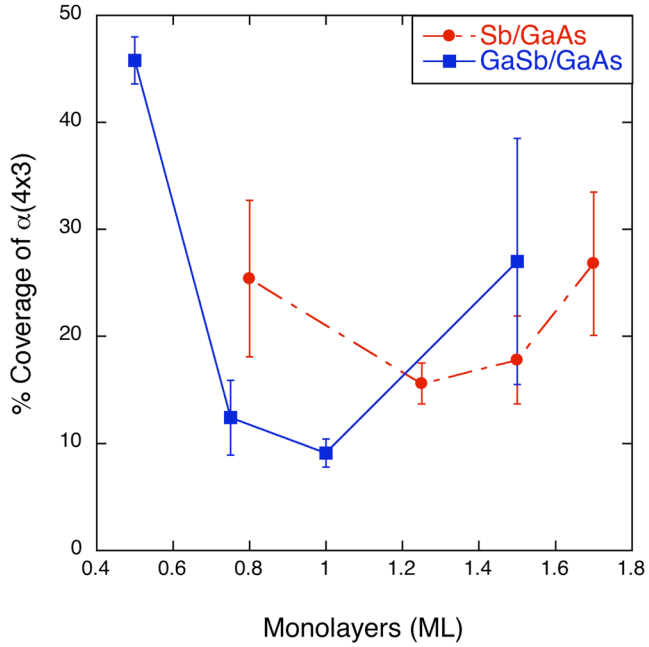

***Figure 4.10**: Percent of the surface covered by the α(4x3) reconstruction vs. film thickness (MLs).*

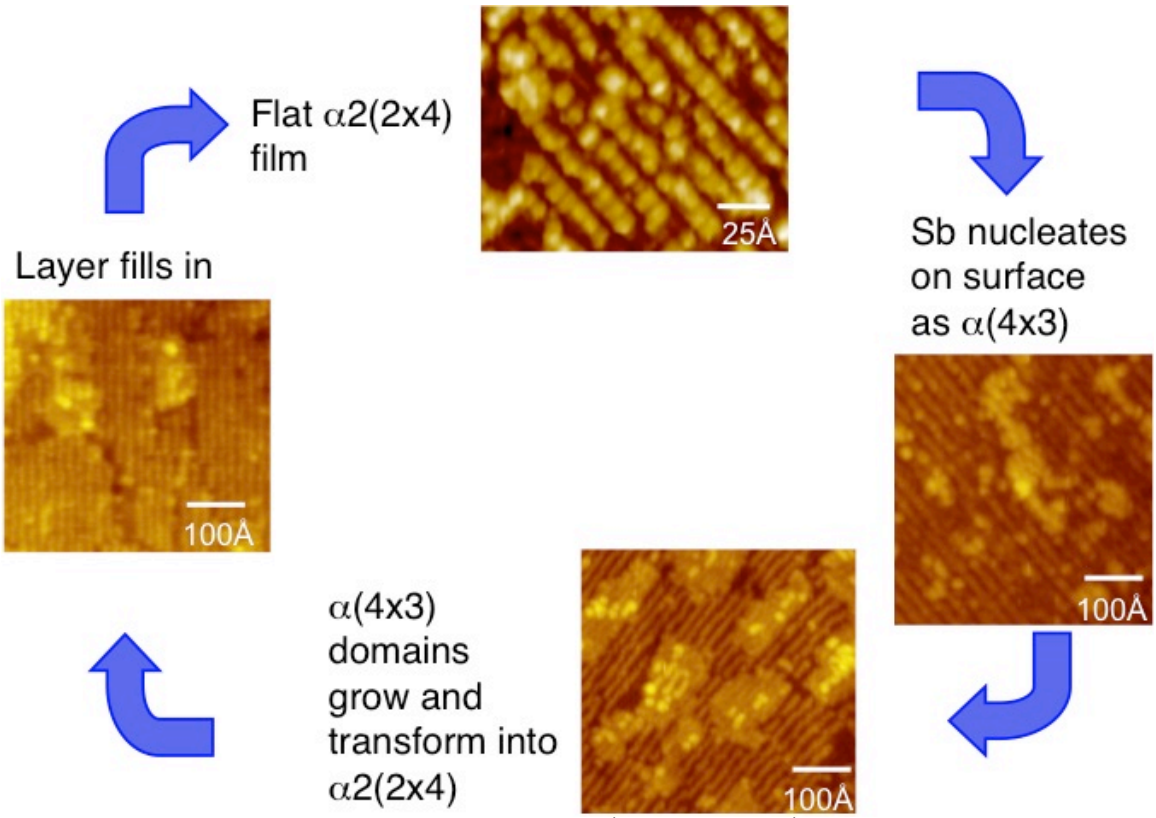

***Figure 4.11**: Surface development model for Sb/GaAs and GaSb/GaAs.*

***Table 4.1**: Surface coverage of α(4x3) as a function of deposition rate*

R_{Sb} (ML/s)	% α(4x3)	Std. Dev.
0.36	25.38	7.29
0.57	16.76	7.13
1.06	34.63	2.53

An analysis of STM images, such as those in Fig. 4.11, shows that while the α(4x3) is always present at step edges normal to the $[1\bar{1}0]$, it is not always present at step edges normal to the [110]. This is due to the directionality of Ga diffusion or the anisotropy of the α2(2x4) and α(4x3) surface reconstructions, or to a combination of both these factors. Ga diffuses more quickly along the [110] direction and this rate is increased in the presence of Sb [19]. Therefore Ga is more likely to be present along this direction to affect the Ga limited transformation from the α(4x3) to the α2(2x4) reconstruction. Along the $[1\bar{1}0]$ the Ga diffuses more slowly, resulting in a higher amount of the Ga-poor reconstruction.

d. *Surface Reconstruction Evolution Model for GaSb/GaAs Thin Films*

The morphological evolution of the surface suggests a possible model of how the Sb is incorporated into these GaSb/GaAs films, which is illustrated schematically in Fig. 4.12. For simplicity, it is assumed that no intermixing between the As and Sb species occurs. Initial growth from the pure β2(2x4) GaAs buffer layer into the GaSb α(4x3) is shown in Figs. 4.12a-d. Assuming that the initial steps of this growth proceed as for GaAs homoepitaxy [20], Sb will incorporate first into the (2x4) trench. This requires a Ga atom to incorporate, breaking the As trench dimer bond, and the Sb incorporates above the Ga resulting in the surface pictured in Fig. 4.12b. The two sides of the trench are equivalent and so entropy dictates the Sb atom may incorporate on either side. The trench will not be totally eliminated as there is a high energy barrier to complete filling [20]. Thus the result is a flat surface with every 3rd to 5th anion missing along the [110]. The next two processes are assumed to occur simultaneously. As shown by the arrow in Fig. 4.12c, the trench can be completely filled in by Sb, and as shown by the arrow in Fig. 4.12d, an Sb-Ga heterodimer can adsorb upon the surface. While initially the barrier to trench

filling may be higher than that of dimer adsorption, the trench must fill for the surface to adsorb all the heterodimers needed to form the α(4x3) reconstruction. Once completed, the α(4x3) reconstruction is formed on the surface as seen in Fig. 4.12e.

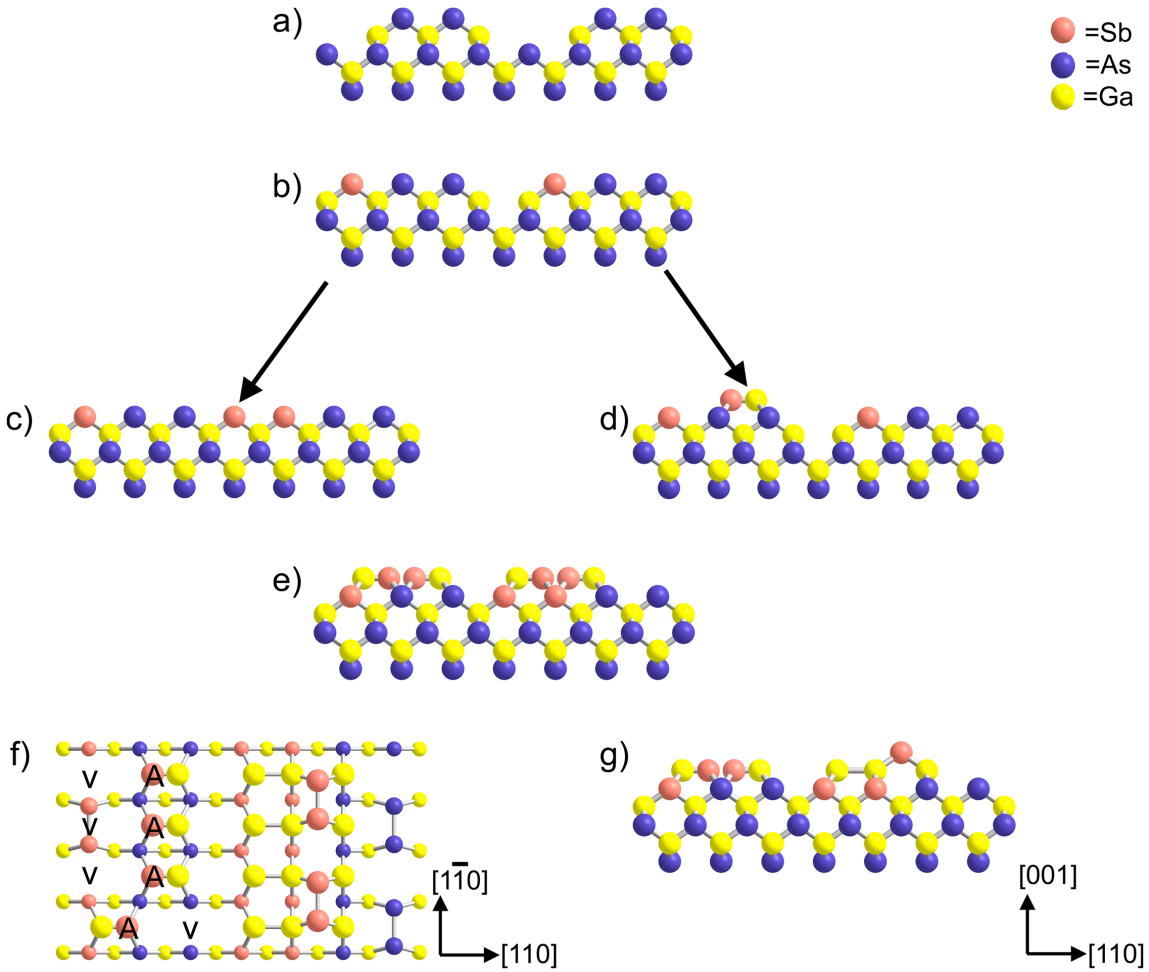

***Figure 4.12**: Schematic model of Sb incorporation into GaAs surface to form α2(2x4)-α(4x3) reconstructed surface. (a) Initial surface of pure GaAs β2(2x4). (b)-(e) Development of the α(4x3) reconstruction by the incorporation of Sb in the trench (b), completion of the trench (c) and/or formation of the Ga-Sb heterodimer (d), and final establishment of the α(4x3). (f) Plan-view schematic of the reconstructed surface showing the Ga vacancies (V) and Sb anti-sites (A) available in the α(4x3) for the transformation to the α2(2x4). (g) cross-sectional view of the coexistence of the α(4x3) and the α2(2x4).*

The transformation of the pure α(4x3) reconstruction into the α(2x4) to form the mixed reconstruction surface requires additional Ga, as discussed above. The surface anions sitting in anti-sites of the α(4x3) (indicated by A in Fig. 4.12f) must be displaced by Ga, and two more Ga are required to fill vacancies in the cation layer (indicated by V in Fig. 4.12f) in order to complete

each (2x4) structure. The Sb atoms displaced by Ga remain on the surface moving from the cation layer to the empty anion layer above, which dimerize as seen in Fig. 4.12e-f, thus completing the transformation.

iii. Lattice Mismatch Strain Stabilization of Surface Reconstructions

After analyzing the different surface structures which appear experimentally and the growth conditions under which they are stable, DFT can be used to analyze the influence of strain on the structures. In the case of the (2x8) reconstruction, the structure is very Sb rich and is only seen for strained thin films of GaSb/GaAs, but not for GaAs or for GaSb at its relaxed lattice parameter [8, 16, 17]. In the case of the α2(2x4)-α(4x3) reconstruction, this *coexistence* of reconstructions is new and, for the III-V semiconductor system, has only been reported for alloyed surface structures [13, 14]. Thus, in each of these cases, it is reasonable to assume that lattice mismatch strain is playing a role in [8, 9] the structural stability of these films.

a. Examining the Coexistence of the α2(2x4)-α(4x3) Reconstructions

The mixed α2(2x4)-α(4x3) reconstruction is stable under a range of growth conditions. However, coexistence of multiple reconstructions has only been reported for alloyed systems, suggesting strain plays a role in the stability of this surface. The relative amounts of the reconstruction are impacted by both the presence of Ga in the supplied flux and the size of the 2D islands on the surface. The size of the 2D islands appears to have a strong influence on the appearance of the α2(2x4) reconstruction within the islands. Figure 4.13 displays a range of Sb/GaAs samples with differing thickness. For $0.8 \leq h \leq 1.7$ ML, Sb/GaAs small 2D islands consist entirely of the α(4x3) reconstruction, as can be seen in the small 2D islands in Fig. 4.13. As the island size increases, the 2D islands transform to also include patches of the α2(2x4) reconstruction, as is seen for the large islands in Fig. 4.13. An analysis of many STM images shows the average island size at which the α2(2x4) reconstruction appears is $30 \pm 10 nm^2$.

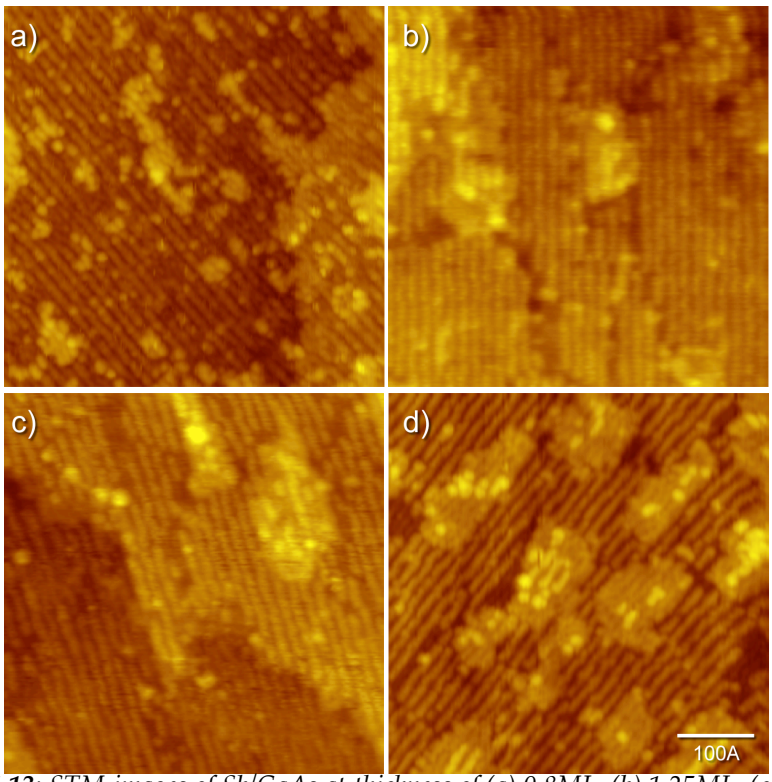

***Figure 4.13**: STM images of Sb/GaAs at thickness of (a) 0.8ML, (b) 1.25ML, (c) 1.5ML, and (d) ~1.7ML. Images taken at I=100pA and -4.5<V<-3.2V.*

The stable surface reconstruction and resulting surface morphology are typically the result of several competing interactions. These include displacement strain, surface charge neutrality, local chemistry, and chemical potential, all of which are, at least indirectly, temperature dependent. In the case described here, both the α2(2x4) and the α(4x3) reconstructions exhibit charge neutrality and the correct local chemistry. Since they are grown on the same surface and remain stable upon cooling, the chemical potential is also constant for these two reconstructions. The fact that the α(4x3) reconstruction only appears at step edges very strongly suggests that elastic strain relaxation impacts the stability of the reconstructions of these very thin strained layers.

The surface energies of the α2(2x4), β2(2x4), α(4x3), β(4x3), and the c(4x4) reconstructions of GaSb are plotted as a function of Sb chemical potential in Fig. 4.14 at both the GaSb (Fig. 4.14a) and GaAs (Fig. 4.14b) lattice parameters. Slabs of pure GaSb are used because the surface is assumed to be pure GaSb due to the tendency of Sb to surface segregate [21] and also the fact that x-ray studies of Sb-capped GaAs with a (2x4) reconstruction show the Sb is limited to the surface

[22]. The surface energies are calculated using the method described by Wixom *et al.* [23]. The x-axis is chemical potential of Sb, μ_{Sb}, relative to that of bulk rhombohedral Sb, $\mu_{S\beta(bulk)}$. The reconstruction with the lowest energy at a given $\mu_{Sb} - \mu_{S\beta(bulk)}$ is predicted to be the stable reconstruction on the surface with higher energy curves energetically inaccessible. At the GaSb lattice parameter (Fig. 4.14a), the most stable reconstructions with decreasing chemical potential (moving left along the x-axis) are the c(4x4), followed by the β(4x3), α(4x3), and α2(2x4). This agrees with the calculations of Righi *et al.* [24] which shows a (4x3) reconstruction for Sb rich GaSb and a β2(2x4) reconstruction for Ga rich GaSb. When the GaSb crystal is constrained to the GaAs lattice parameter (Fig. 4.14b), the stability of the different reconstructions changes dramatically. The lines shift relative to each other to the point that the α(4x3) reconstruction is never the lowest line for any chemical potential, and thus is excluded as a stable reconstruction at this lattice parameter. Instead, the stable reconstructions with decreasing chemical potential are the β(4x3), followed by the β2(2x4) and α2(2x4) reconstructions. This is due to changes in the relative energy of the different reconstructions, which can be seen in the y-axis intercept point. The changes in relative energy also result in a change in the relative cross-over points of the reconstructions. The transition from the (4x3) reconstructions to the (2x4) reconstructions is shifted to a higher chemical potential by $\Delta\mu_{Sb}$=0.25eV

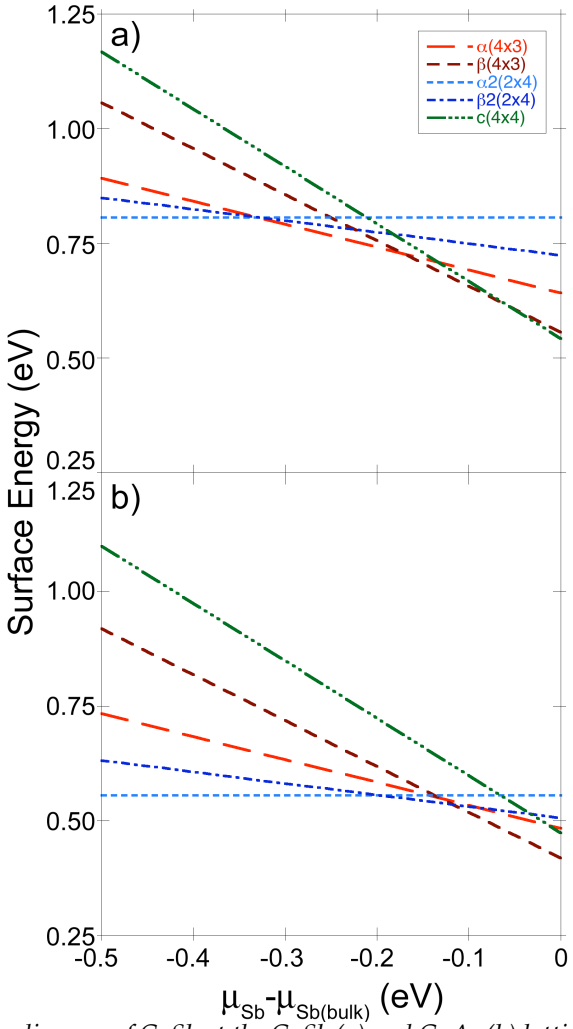

***Figure 4.14**: Phase diagram of GaSb at the GaSb (a) and GaAs (b) lattice parameters.*

The shift in stability of the surface reconstructions of GaSb between the GaSb and GaAs lattice parameters is demonstrated by the appearance of both the α2(2x4) and β(4x3) reconstructions in the Sb/GaAs films, with the α(4x3) appearing at step edges where elastic relaxation occurs and the α2(2x4) appearing in areas where the lattice parameter is constrained, i.e. within large terraces or near the center of large 2D islands. This mixed reconstruction has not been previously reported, even for Sb-capped GaAs [8, 9, 17, 25-28]. This is likely due to different growth conditions of those experiments, which often include extensive annealing that would decrease the chemical potential thus further stabilizing the (2x4). A strain induced shift in reconstruction stability has been predicted by DFT [29] and suggested as the mechanism behind the atomic structure which develops in the Sb:Ge/Si(111) system [30]. The work presented

here, however, shows that a local variation in strain can produce a *coexistence* of reconstructions on a single surface.

The mechanism by which the α2(2x4) surface reconstruction in GaSb is stabilized may be understood by examining the details of the atomic arrangement within the individual reconstructions. Near step edges, the Sb bond lengths elastically relax towards that of bulk GaSb because they are not laterally constrained by the substrate and thus may take on the bulk GaSb reconstruction, α(4x3). Away from step edges, the layer is constrained by the substrate, thus inducing the α2(2x4) reconstruction. This suggests that the α2(2x4) reconstruction can relieve the high compressive strain better than the β(4x3), likely due to the fact that the α2(2x4) has a larger surface corrugation than the β(4x3). As measured in Fig. 4.1b, the peak to valley height of the α2(2x4) is 3.1Å, while that of the β(4x3) is 1.8Å; both are in close agreement with simulation results. By considering other bond lengths and distances between atoms, the mechanism by which the α2(2x4) relieves stress becomes apparent. Simulation results show that the heterodimer in the α(4x3) reconstruction cannot accommodate the compressive strain induced by being constrained to the GaAs lattice parameter. However, there is a mechanism by which this strain may be relieved in the α2(2x4) reconstruction. This reconstruction has a cation-cation back bond, which is circled in Fig. 4.15. This bond is normally in tension. Reducing the lattice parameter to that of GaAs reduces the tension in this bond to compensate exactly for the compressive strain. This explanation is consistent with the experimental observations of the dependence of the reconstruction on 2D island size. Specifically, small 2D islands exhibit only the α(4x3) reconstruction while 2D islands greater than a critical size exhibit the α2(2x4) in the center and α(4x3) at the edges.

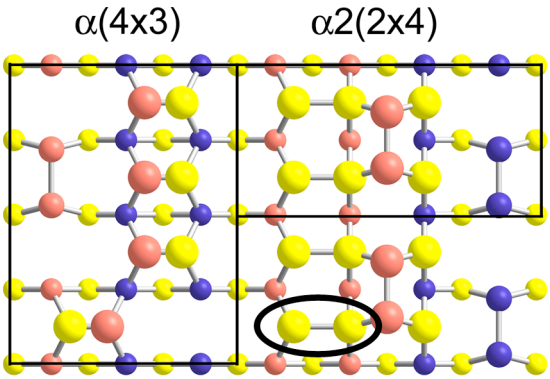

Figure 4.15: *Plane-view (a) schematic of the α(4x3) and α2(2x4) reconstructions. Yellow = Ga cation, Pink = Sb anion, Blue = As anion.*

b. *The Structure of the (2x8) Surface Reconstruction*

Two structures have been proposed in the literature for the GaSb/GaAs-(2x8) reconstruction. This work examines these two structures, a (2x8) structure proposed for InSb and a variant on this structure in order to determine the actual structure of the GaSb-(2x8) reconstruction. Each of the structures obeys the ECR and terminates in a double anion layer, as suggested by experimental observations. The first structure was initially proposed for the InSb (2x8) reconstruction [31], and is referred to here as the β(2x8) (Fig. 4.16a). This structure consists of a backbone of Sb dimers along the $[1\bar{1}0]$ (2 dimers per unit cell) in the topmost Sb layer. This layer sits atop a second Sb layer, which has an additional four anion dimers along the [110] which orient parallel to the $[1\bar{1}0]$. A final anion dimer sits in the trench between adjacent unit cells. This structure is termed the β(2x8) because it contains a single unit cell of the α2(2x4) reconstruction common to III-As systems (outlined in Fig. 4.16a - left). The β(2x8) reconstruction may be easily constructed from a base structure of two α2(2x4) cells by adding two Ga and eight Sb atoms above the central trench dimer. A simulated filled state STM image is shown in the center of Fig. 4.16a. These images were generated using the method proposed by Tersoff *et al.* [32]. A single (2x8) unit cell is outlined in the simulated STM image. This STM image shows the regularity of the electron density along the anion backbone along the $[1\bar{1}0]$ and a periodic increase and decrease along the [110]. This variation also appears in a line scan in the [110], determined from averaging the z-height at all $[1\bar{1}0]$ positions within the unit cell (Fig. 4.16a - right). The original data is shown

in the dotted line, and the result is smoothed using a Steinman function and applying a geometric weighting of the nearest 10% of data points to get the solid line. This smoothed function more accurately simulates a rounded STM tip and results in an almost sinusoidal change in apparent height. The second structure, the β(2x8) (Fig. 4.16b), is similar, except that it is built from the III-As β2(2x4) reconstruction that contains two Sb surface dimers (outlined in Fig. 4.16b-left) and exhibits a similar simulated STM image and line scan. The addition of an extra Sb surface dimer to the horizontal results in wider rows along the [110], changing the line scan shape to a cycloid. The third structure was proposed by Laukkanen *et al.* [8] as a possible structure for the GaSb-(2x8) reconstruction. Because this structure also contains the β2(2x4) unit cell as a basis structure, it is herein termed the β2(2x8) reconstruction. The β2(2x8) only has a single Sb dimer in the topmost surface layer, which requires the introduction of Sb atoms into anti-sites in the topmost cation layer to maintain charge neutrality. The simulated STM image differs from that of the β(2x8) in that it shows a periodic change in intensity along the $[1\bar{1}0]$ due to the presence of the single anion dimer per unit cell. The [110] line scan is very similar to that in Fig. 4.16b, but lower in amplitude due to averaging over the periodically missing anion dimer. The final structure is a modification of that proposed by Whitman *et al.* [9] as a possible structure for the GaSb-(2x8) reconstruction and is shown in Fig. 2d. This structure, herein termed as the γ(2x8), resembles that of the β2(2x8), containing the same missing dimer along the $[1\bar{1}0]$ that requires two Sb anti-sites. This structure does not have a trench dimer; instead, the trench is filled with an additional pair of Ga atoms. The result a two dimer structure on the right side of the reconstruction, and a three dimer structure which is a known III-As unit cell, the β(2x4) unit cell [15] (outlined Fig. 4.16d-left), on the left of the Sb dimer chain $[1\bar{1}0]$ backbone. This configuration admits the possibility for disorder within the structure as the two dimer and three dimer structures can change sides in adjacent unit cells, resulting in the top-most Sb dimer backbone shifting positions between adjacent unit cells. The simulated STM of the γ(2x8) structure is similar to that of the β2(2x8) without a gap for the trench dimer, and the resulting line

scan is shallow in depth between adjacent unit cells due to the lack of the trench and takes on a shallow centroid shape.

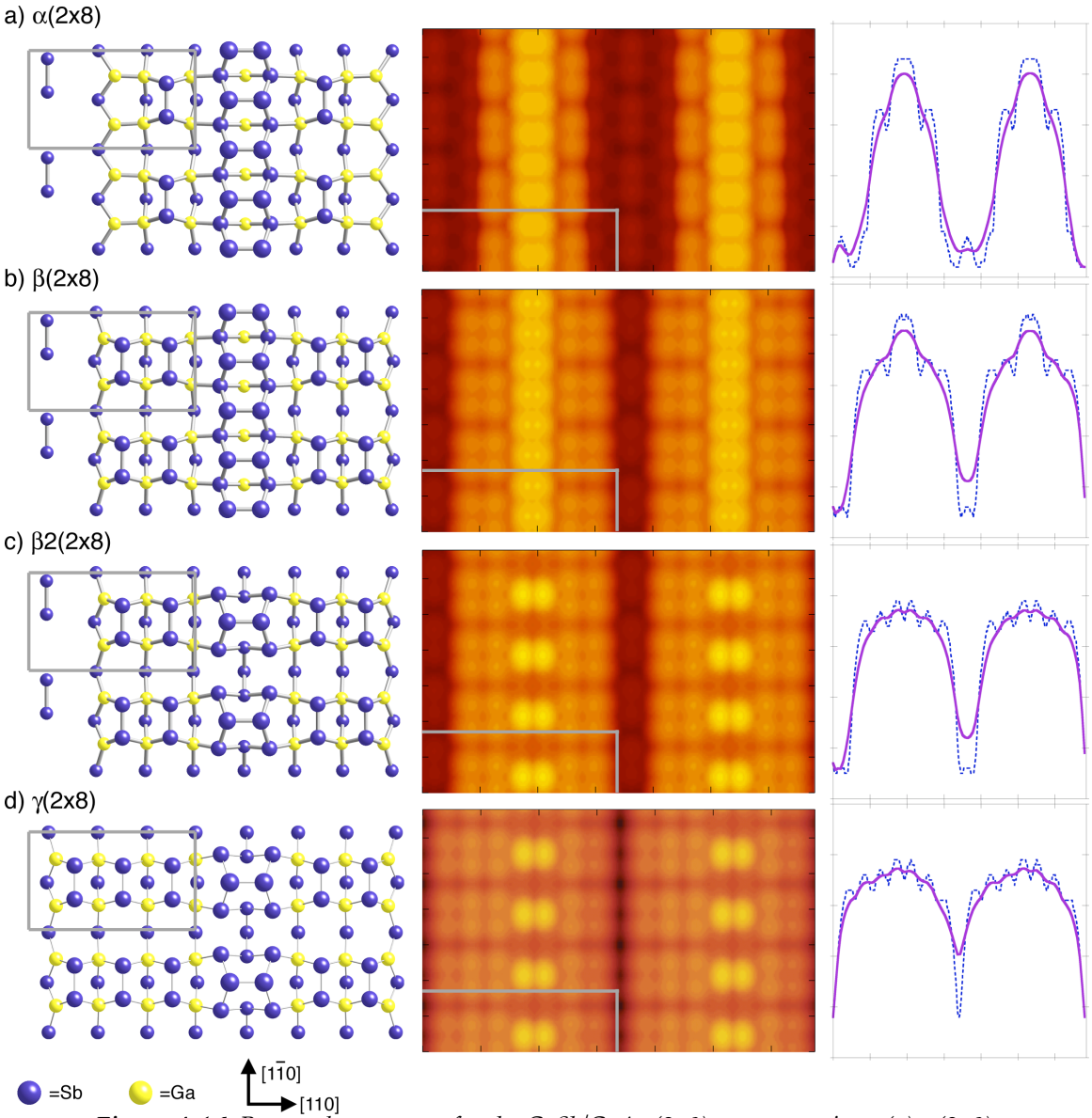

***Figure 4.16**: Proposed structures for the GaSb/GaAs-(2x8) reconstruction. (a) α(2x8), (b) β(2x8), (c) β2(2x8), and (d) γ(2x8). On the left are the atomic structures (Note: Some atoms removed for clarity). The boxes show relationships of the (2x8) to similar (2x4) reconstructions. In the middle are simulated filled-state (negative bias) STM images. (ticks = 10Å). The box outlines a single (2x8) unit cell. On the right are line scans of the simulated STM images with the original data (dotted line) and a smoothed line (solid line) calculated using a Steinman function and applying a geometric weighting of the nearest 10% of data points. (x-ticks = 10 Å, y-ticks = 1Å).*

Qualitative similarities between the experimental and simulated STM images suggest that the β(2x8) reconstruction is a promising candidate for the atomic structure of the experimentally obtained (2x8) reconstruction. The

original STM of the (2x8) obtained experimentally (displayed in Fig. 4.7) is reproduced as Fig. 4.17 for comparison to the simulated STM images in Fig. 4.16. Both the α(2x8) and β(2x8) structures exhibit straight rows of intensity along the $[1\,\bar{1}\,0]$, in agreement with the straight row of intensity seen in Fig. 4.17a along the dimer backbone. However, examination of the line scan in Fig. 4.17c shows a very sinusoidal character with almost even widths of the peaks and valleys. The β(2x8) reconstruction shows a broader peak with a narrow valley, while the α(2x8) shows a line scan which closely resembles a sinusoid, suggesting the α(2x8) structurally agrees with experimental results.

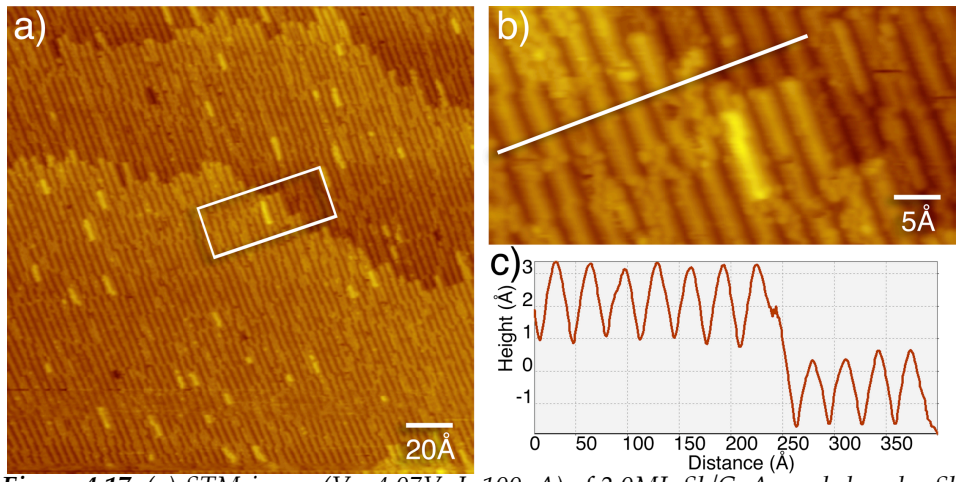

Figure 4.17: *(a) STM image (V=-4.07V, I=100pA) of 2.0ML Sb/GaAs cooled under Sb flux to form the (2x8) reconstruction. (b) High resolution portion of the image in (a). (c) A line scan across the line indicated in (b).*

The relative stabilities of these three possible (2x8) structures were examined using Density Functional Theory (DFT). Calculations were performed as described previously, examining the surface reconstructions imposed upon a periodically repeating slab structure. K-point meshes are 6x3, 3x4, 3x3, and 6x2 for the 2x4, 4x3, 4x4, and 2x8 slabs, respectively. The surface energies of the three potential (2x8) reconstructions are plotted against those of other common anion-rich surface reconstructions of pure, relaxed GaAs, including the (2x4) family of reconstructions, and pure, relaxed GaSb, which exhibits the (4x3) family of reconstructions. GaSb slabs were used in all energy calculations because the surface is assumed to be pure GaSb due to the tendency of Sb to surface segregate [21]. The results shown in Fig. 4.18a-c are for pure GaAs slabs relaxed at the GaSb, InP, and GaAs lattice parameters respectively. The grand

canonical surface free energies were determined by relaxing each structure, then relating the surface energy to the surface stoichiometry and Sb chemical potential according to the method described by Wixom *et al.* [23]. The resulting energy values are plotted along the y-axis in (eV) vs. the chemical potential of Sb relative to that of bulk, rhombohedral Sb, μ_{Sb}-$\mu_{S\beta(bulk)}$, on the x-axis. The lowest curve at any given chemical potential is the thermodynamically stable reconstruction, with higher energy reconstructions energetically inaccessible. The x-axis boundaries are determined by the bulk energy of rhombohedral Sb and the calculated formation energy of GaSb, which is -0.3eV per GaSb unit. This value is slightly smaller than experimentally reported values [33]. However the predicted stable reconstructions at the GaSb and GaAs lattice parameters agree qualitatively with the experimental results.

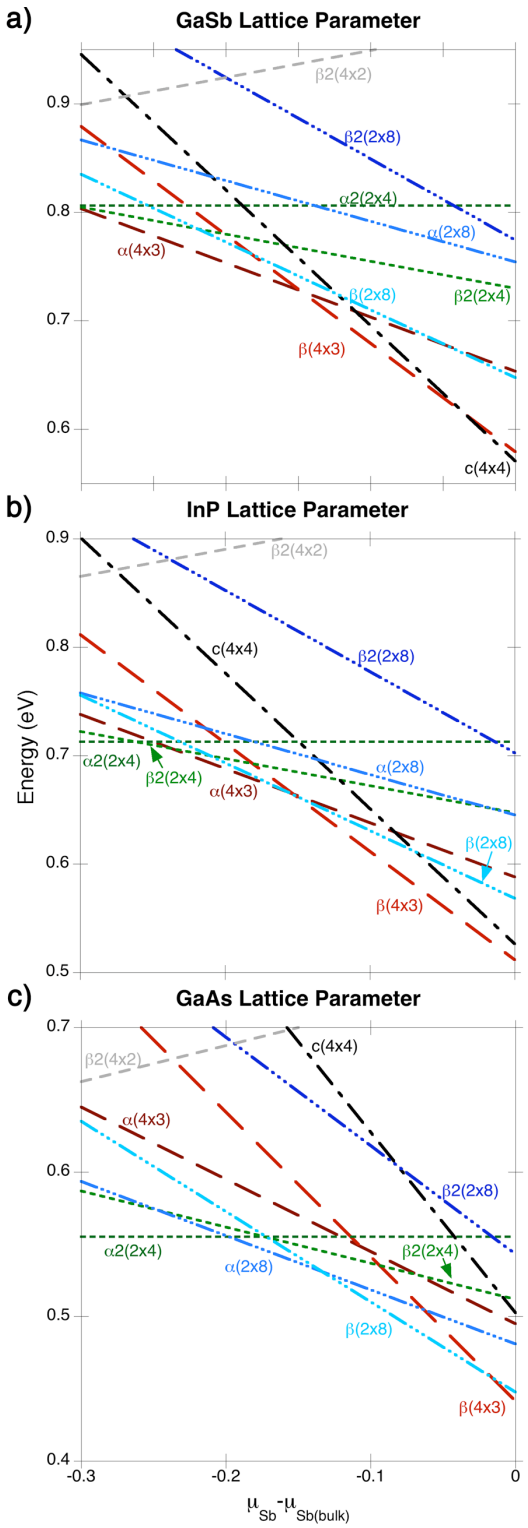

***Figure 4.18**: Energy vs. μ_{Sb}- $\mu_{S\beta(bulk)}$ at the (a) GaSb, (b) InP, and (c) GaAs lattice parameters, respectively. The lowest line on any graph is the stable reconstruction at that chemical potential.*

GaSb surface reconstructions were examined at three different lattice parameters in order to determine how stability changes as a function of strain. The three lattice parameters examined are: (1) GaSb, as a control state because the surface structure of GaSb at the GaSb lattice parameter is relatively well understood [7]; (2) InP, an intermediate lattice parameter chosen to examine the stability of the surface reconstructions changes as a function of compressive strain; and (3) GaAs, as this is nominally the lattice parameter of the film in the experiments. Figure 4.3a shows that for GaSb at the GaSb lattice parameter, the stable reconstructions with increasing μ_{Sb} are the α(4x3), β(4x3) and c(4x4). The α(4x3) and β(4x3) reconstructions are experimentally observed and are generally accepted to be the stable surface reconstructions for pure unstrained GaSb at typical growth conditions. However, under very Sb rich conditions a third reconstruction is experimentally observed, either a c(2x10) or c(2x5) reconstruction [34]. There is little consensus on the atomistic details of the c(2x10)/c(2x5) reconstruction, and recent x-ray experiments rule out all of the proposed structures [34]. For this reason, the c(4x4) reconstruction is used as a proxy for the c(2x5)/c(2x10) reconstruction in our energy calculations. This substitution was chosen because the c(4x4) is reported in the AlSb system [7], which has the same surface reconstructions as GaSb under most growth conditions. Our DFT calculations show that the c(4x4) is stable only at the highest values of μ_{Sb} at the GaSb lattice parameter, consistent with expectations.

When the lattice parameter is constrained to the smaller InP lattice parameter, the relative stability of the different surface reconstructions changes as each surface atomic configuration accommodates the compressive strain differently. At the InP lattice parameter, the stable reconstructions with increasing μ_{Sb} are the α2(2x4), β2(2x4), α(4x3) and β(4x3). The c(4x4) proxy has increases in energy such that it is no longer stable at any chemical potential. The α(4x3) and β(4x3) remain stable, although not over as large a chemical potential range. The β(2x8) reconstruction decreases in energy relative to the (4x3) reconstructions and approaches stability at the intersection of the α(4x3) and β(4x3) lines.

This shift in stability of the various surface reconstructions continues as the lattice parameter is further reduced to that of GaAs (Fig. 4.3c), where the stable reconstructions with increasing Sb are the α2(2x4), α(2x8), β(2x8), and β(4x3) reconstructions. The DFT results show that the stability of the (4x3) reconstructions is all but eliminated. The β(4x3) is stable only at very high values of μ_{Sb} and the (2x4) and (2x8) reconstructions are the stable reconstructions at most chemical potentials. This agrees with experimental results that demonstrate the stability of the (2x4), (2x8) and (4x3) [7-9, 16, 17, 35].

At the GaAs lattice parameter, it is evident that the stable GaSb/GaAs-(2x8) reconstruction is the α(2x8) or β(2x8). Interestingly, the β(2x8) has a lower energy than the β(2x8) at the InP lattice parameter, but the β(2x8) decreases much more rapidly in energy as the lattice constant is reduced further, to become stable at the GaAs lattice parameter. This may be due to the highly tensile cation-cation bond present in this structure. Thus, as the lattice parameter is reduced, the amount of strain within this cation-cation bond is reduced, dramatically lowering the energy of the structure. The low energy of the β(2x8) and β(2x8) reconstructions relative to other reconstructions may be due to the presence of surface Sb-dimers in both the [110] and $[1\bar{1}0]$ directions, which may allow the 7% mismatch strain of the surface to be relieved along both directions.

These results also show that the proposed β2(2x8) and γ(2x8) reconstructions are never in thermodynamic equilibrium, as they are always >25meV per unit area higher than the stable reconstruction at any μ_{Sb} at any lattice parameter. The γ(2x8) is always greater in energy than the β2(2x8), which is consistent with III-As calculations that show the β(2x4) higher in energy than the β2(2x4) reconstruction. The higher energies of the β2 and γ(2x8) reconstructions are likely due to the Sb anti-sites in these structures. Experimentally, it is possible that anti-sites may form, given that both Sb and Ga are required but only Sb is supplied in the growth flux. Despite this, the results suggest that no anti-sites form in these experiments as the STM results are consistent only with the α(2x8) and β(2x8) which show no intensity change along the dimer chains in the $[1\bar{1}0]$ direction.

iv. Conclusions

This chapter examines the GaSb/GaAs surface. It explores the possible surface structures obtainable with different growth parameters: (1) for sub-monolayer growth of Sb/GaAs, a mottled, disordered film develops, (2) for mid-thickness Sb/GaAs and for GaSb/GaAs films a mixed α2(2x4)-α(4x3) reconstruction appears on the surface, and (3) for very Sb rich conditions the surface forms a (2x8) reconstruction. The surface development of the α2(2x4)-α(4x3) is discussed and shown to nucleate initially as 2D α(4x3) islands that grow as more material is deposited. When these islands reach a critical size they transform to coexist as the α2(2x4)-α(4x3). The islands continue to grow, coalescing into a single α2(2x4) surface. A model for the incorporation of Sb into the surface is developed. Ga presence plays a large role in this incorporation, acting as a rate limiting step in the surface transition from small α(4x3) islands to mixed α(4x3)-α2(2x4) islands. In the presence of Ga, this transition is easy; but without supplied Ga, the surface transition is more limited. The presence of the α(4x3)-α2(2x4) in films grown with and without a supplied Ga flux shows that the mixed reconstruction surface is thermodynamically stabilized rather than kinetically stabilized due to an inability to transform to the low energy surface configuration.

Lattice mismatch strain plays a large role in the stability of GaSb/GaAs thin films. In the case of the mixed α(4x3)-α2(2x4) reconstruction, elastic relaxation of the lattice parameter at step edges induces a surface reconstruction coexistence in the alloy. The α(4x3) reconstruction is common to homoepitaxially grown GaSb. The α2(2x4) is not seen in the III-Sb system, but it is common to the GaAs system of the substrate. The introduction of the α2(2x4) reconstruction to the GaSb film occurs because of the ability of the cation-cation backbond to more effectively relieve compressive strain.

Lattice mismatch strain also induces the stability of another reconstruction, the (2x8) reconstruction, not seen in homoepitaxially grown films. Under Sb rich conditions, a (2x8) reconstruction is obtained which is stabilized due to the lattice mismatch strain between the film and substrate. Four atomistic (2x8) reconstruction models of this reconstruction are examined and the structure

is shown to be the α(2x8) reconstruction. As with the α2(2x4), the α(2x8) reconstruction appears because it is more able to relieve the compressive strain imparted into the film from the substrate.

The stability of the mixed α2(2x4)-α(4x3) and the α(2x8) reconstruction shows the dramatic impact that lattice mismatch strain can have on the surface reconstructions of covalently bonded films and the discussion of atomistic incorporation shows the influence the surface reconstruction has on continued film development. This suggests that if surface reconstructions can be engineered via strain, they may provide a pathway for self-assembly on the surface of covalent materials.

v. References

1. J. E. Arvery, L. M. Fraas, V. S. Sundaram, N. Mansoori, J. W. Yerkes, D. J. Brinker, H. B. Curtis, and M. J. O'Neil, *Conf. Rec. of the 21st IEEE Photovoltaic Specialists Conference* **2**, 1277 (1990).
2. L. Fraas, B. Daniels, H.-X. Huang, J. Avery, C. Chu, P. Iles, and M. Piszczor, *Conf. Rec. of the 28st IEEE Photovoltaic Specialists Conference* **1**, 1150 (2000).
3. P. M. Thibado, B. R. Bennett, M. E. Twigg, B. V. Shanabrook, and L. J. Whitman, *J. Vac. Sci. and Tech. A* **14**, 885 (1996).
4. S. H. Huang, G. Balakrishnan, A. Khoshakhlagh, A. Jallipalli, L. R. Dawson, and D. L. Huffaker, *Appl. Phys. Lett.* **88**, 131911 (2006).
5. A. Jallipalli, G. Balakrishnan, S. H. Huang, A. Khoshakhlagh, L. R. Dawson, and D. L. Huffaker, *J. Cryst. Growth* **303**, 449 (2007).
6. R. Kaspi, and K. R. Evans, *J. Cryst. Growth* **175**, 838 (1997).
7. W. Barvosa-Carter, A. S. Bracker, J. C. Culbertson, B. Z. Nosho, B. V. Shanabrook, L. J. Whitman, H. Kim, N. A. Modine, and E. Kaxiras, *Phys. Rev. Lett.* **84**, 4649 (2000).
8. P. Laukkanen, R. E. Perala, R.-L. Vaara, I. J. Vayrynen, M. Kuzmin, and J. Sadowski, *Phys. Rev. B* **69**, 205323 (2004).
9. L. J. Whitman, B. R. Bennett, E. M. Kneedler, B. T. Jonker, and B. V. Shanabrook, *Surf. Sci. Lett.* **436**, L707 (1999).
10. M. D. Pashley, *Phys. Rev. B* **40**, 10481 (1989).
11. Y. Q. Wang, Z. L. Wang, T. Brown, A. Brown, and G. May, *J. Cryst. Growth* **242**, 5 (2002).
12. B. A. Joyce, and D. D. Vvendensky, *Mat. Sci. and Eng. R* **46**, 127 (2004).
13. P. A. Bone, J. M. Ripalda, G. R. Bell, and T. S. Jones, *Surf. Sci.* **600**, 973 (2006).
14. J. Mirecki Millunchick, A. Riposan, B. Dall, C. Pearson, and B. Orr, *Surf. Sci.* **550**, 1 (2004).
15. H. Yamaguchi, and Y. Horikoshi, *Phys. Rev. B* **51**, 9836 (1995).
16. F. Maeda, Y. Watanabe, and M. Oshima, *Phys. Rev. B* **48**, 14733 (1999).
17. P. Moriarty, P. H. Beton, Y. R. Ma, and M. Henini, *Phys. Rev. B* **53**, R16148 (1996).
18. J. E. Bickel, C. Pearson, and J. Mirecki Millunchick, *Surface Science* **603**, 14 (2009).
19. R. R. Wixom, L. W. Rieth, and G. B. Stringfellow, *J. Cryst. Growth* **265**, 367 (2004).
20. P. Kratzer, E. Penev, and M. Scheffler, *Appl. Surf. Sci.* **216**, 436 (2003).
21. S. Froyen, and A. Zunger, *Phys. Rev. B* **53**, 4570 (1996).

22. T.-L. Lee, and M. J. Bedzyk, *Phys. Rev. B* **57**, R15059 (1998).

23. R. R. Wixom, N. Modine, and G. Stringfellow, *Phys. Rev. B* **16**, 115309 (2003).

24. M. C. Righi, R. Magri, and C. M. Bertoni, *Phys. Rev. B* **71**, 75323 (2005).

25. M. Wang, D. Collins, T. McGill, and R. Grant, *J. Vac. Sci. and Tech. B* **11**, 1418 (1993).

26. W. G. Schmidt, and F. Bechstedt, *Phys. Rev. B* **55**, 13051 (1997).

27. R. M. Feenstra, D. A. Collins, D. Z.-Y. Ting, M. W. Wang, and T. C. McGill, *Phys. Rev. Lett.* **72**, 2749 (1994).

28. B. R. Bennett, P. M. Thibado, M. E. Twigg, E. R. Glaser, R. Magno, B. V. Shanabrook, and L. J. Whitman, *J. Vac. Sci. and Tech. B* **14**, 2195 (1996).

29. C. Ratsch, *Phys. Rev. B* **63**, 161306 (2001).

30. A. Antons, Y. Cao, B. Voigtländer, K. Schroeder, R. Berger, and S. Blugel, *Europhys. Lett.* **62**, 547 (2003).

31. W. Barvosa-Carter, F. Grosse, J. H. G. Owen, and J. J. Zinck, *Mat. Res. Soc. Symp. Proc.* **692**, H8.4 (2002).

32. J. Tersoff, and D. R. Hamann, *Phys. Rev. B* **50**, 1998 (1983).

33. K. Yamaguchi, Y. Takeda, K. Kameda, and K. Itagaki, *Mat. Trans.* **35**, 596 (1994).

34. B. P. Tinkham, O. Romanyuk, W. Braun, K. H. Ploog, F. Grosse, M. Takahasi, T. Kaizu, and J. Mizuki, *J. Elec. Materials* **37**, 1793 (2008).

35. J. J. Zinck, E. J. Tarsa, B. Brar, and J. S. Speck, *J. Appl. Phys.* **82**, 6067 (1997).

Chapter V

Impact of Surface Strain on Subsequent Film Growth

Chapters III and IV demonstrate the dramatic impact of strain on surface reconstructions of alloyed films. Strain is also known to greatly impact defect formation in thin film growth, resulting in the nucleation of dislocations or the development of 3D growth in alloyed systems to relieve lattice mismatch strain. It is known that surface reconstructions impact atomic incorporation within a film, which may lead to bulk atomic ordering [1, 2]. This chapter examines the hypothesis that the surface reconstruction is not only affected by strain but also impacts the strain relaxation and surface topography in thin films and interacts with dislocations. These interactions may lead to insertion of specific types of defects into the film structure and, combined with the impact on surface topography, may lead to specific engineering of surface structures and defects.

i. Surface Reconstruction Influence on Film Structure

In order to examine the effect of surface reconstruction on subsequent film growth and defect morphology, two samples were grown under the same growth parameters but on two different starting surface reconstructions–an $\alpha 2(2x4)$ and an $\alpha(2x8)$ reconstruction. Sample growth varied slightly from the growth method described in II.i.i. Samples were grown on 150μm thick wafers freely mounted in Mo rings rather than on 500μm thick wafers In mounted on Mo pucks. This change in both substrate thickness and mounting allows characterization of the stress evolution within the sample by MOS, described in

II.i.c. The surface oxide was desorbed and a 0.5μm buffer was grown as described previously (II.i.i). The α2(2x4) surface was prepared by lowering the buffer under an As_4 overpressure to the film growth temperature of T=525°C. The α(2x8) surface was prepared by closing the As valve while still at the buffer growth temperature of T=600°C. The excess As_4 in the chamber was pumped out, and As was allowed to desorb from the sample surface resulting in a surface reconstruction change to the Ga rich (4x2). The Sb_4 valve and shutter were opened and the sample was lowered to the growth temperature, T=525°C, resulting in a Sb-rich (2x8) reconstruction. Schematic depictions of the α2(2x4) and α(2x8) reconstructions are shown in Figure 5.1. Samples were grown at R_{Ga}=0.30ML/s, which corresponds to R_{GaSb}~0.37ML/s according to the calibration shown in Fig. 2.5. R_{Sb}=0.35ML/s giving a ~1:1 V:III ratio. Each sample was produced using the same growth conditions while only varying the initial surface structure. This allows any differences between the samples to be attributed to the difference in starting surface structure rather than changes in temperature or V:III ratio.

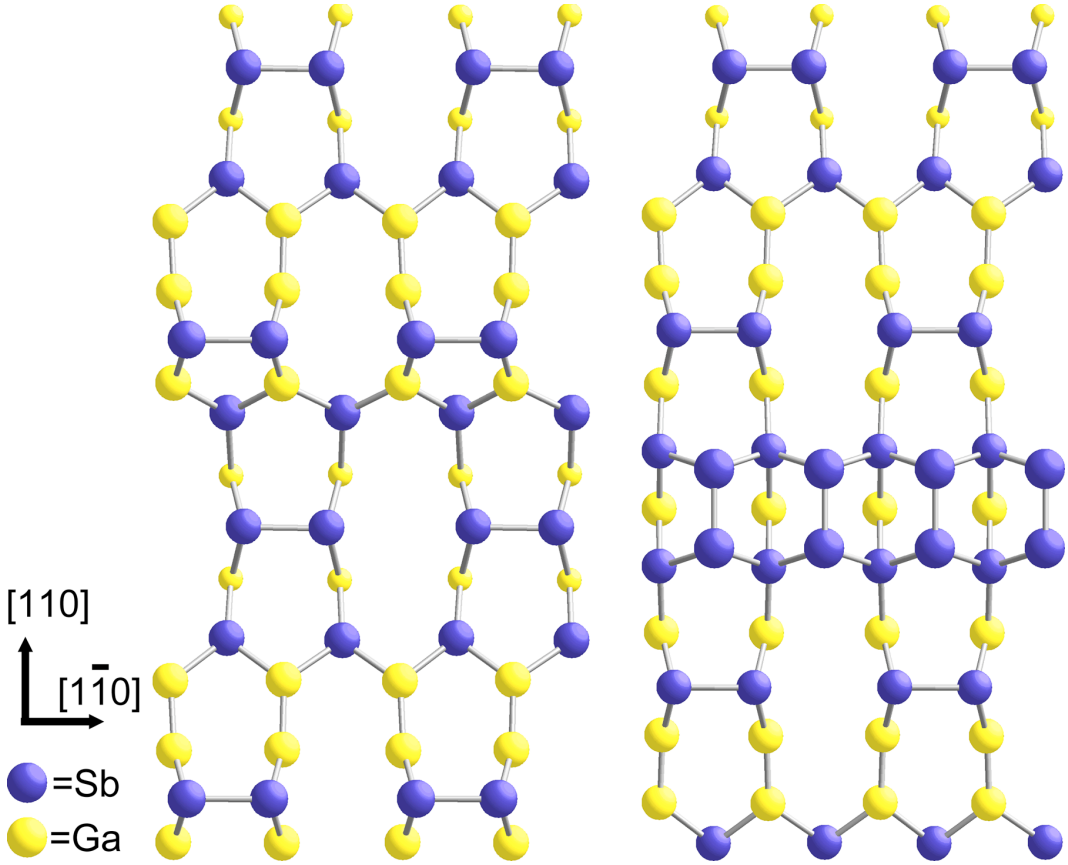

***Figure 5.1**: Schematic surface atomic structures of the (left) α2(2x4) and (right) α(2x8) reconstructions. Some atoms removed for clarity.*

RHEED characterization of the samples during growth shows an immediate difference in the surfaces which develop from the (2x4) and (2x8) reconstructions. Figure 5.2 shows RHEED images of the $[1\bar{1}0]$, [100] and [110] directions of a sample upon completion of the buffer layer (top) and after growth on the (2x4) (middle) and (2x8) reconstructions (bottom). Both the (2x4) and (2x8) samples lose the higher order patterns along the $[1\bar{1}0]$, resulting in a (2x2) reconstruction upon completion of the growth. The RHEED patterns for both samples also show some evidence of surface roughening and 3D growth characterized by the appearance of spots in their patterns. However, while the (2x4) sample is spotty along all axial directions, the (2x8) sample retains a somewhat streaky pattern along the [100] and [110] directions, which is often indicative of a smoother surface.

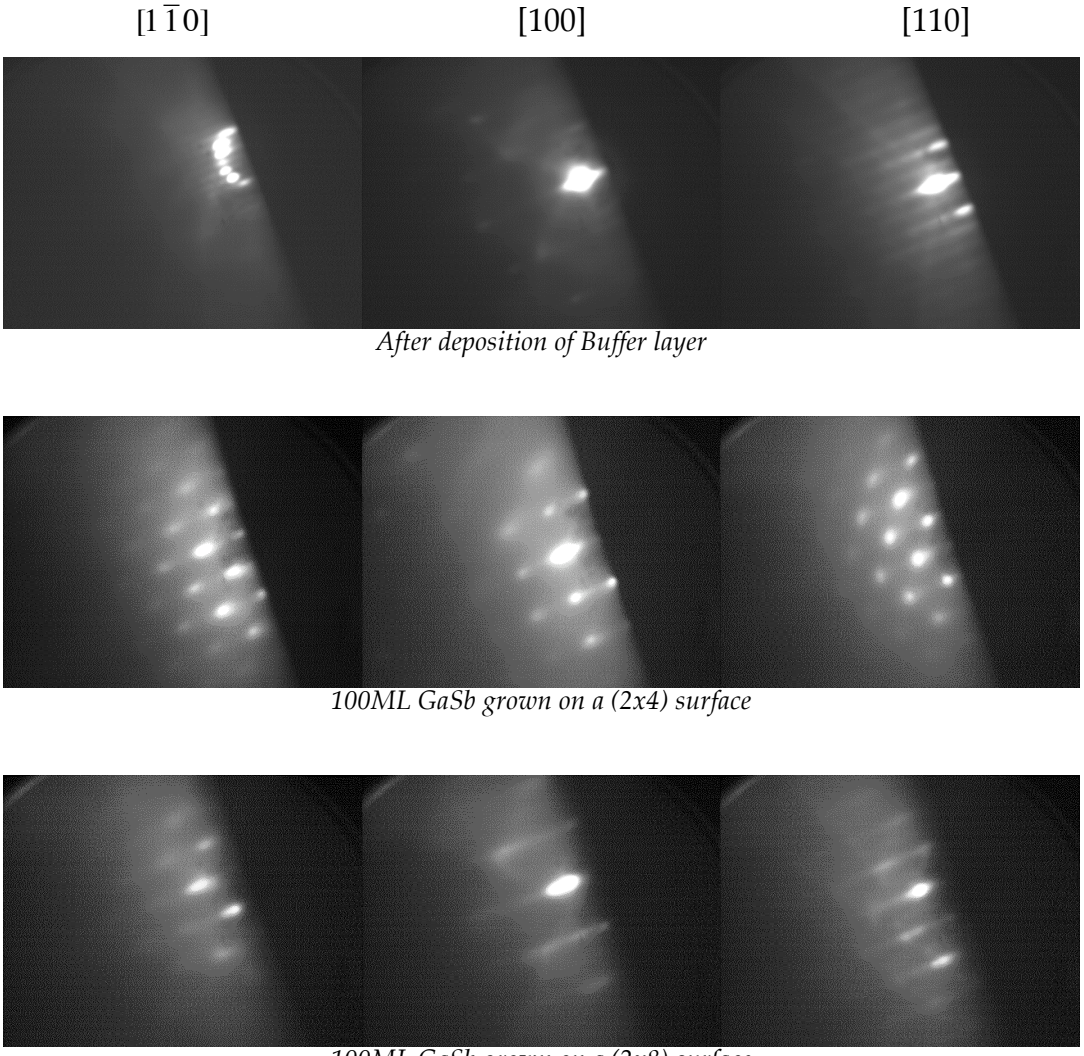

Figure 5.2: *RHEED images taken (top) after buffer deposition (middle) after deposition of 100ML GaSb on the (2x4) reconstruction and (bottom) after deposition of 100ML GaSb on the (2x8) reconstruction.*

The data from MOS curvature measurements also shows distinct differences between the two samples, as shown in Figures 5.3. The MOS laser beam is split by the etalons into an array of multiple beams in both the horizontal and vertical directions, allowing for independent curvature measurements along these axes. The approximate crystallographic directions of these axes can be determined by comparing the relative orientation of the MOS to the RHEED pattern.

Figure 5.3 shows the percentage of strain relaxation, γ, for the two samples. This value calculated by:

$$\gamma = \frac{f - \varepsilon}{f} * 100 \qquad (5.1)$$

where f is the amount of misfit strain, which can be related to the lattice parameters of the film, a_f, and substrate, a_s by:

$$f = \frac{a_s - a_f}{a_s} \qquad (5.2)$$

The strain, ε, is determined by equation 2.2 and is proportional to the curvature of the wafer and the inverse of the film thickness.

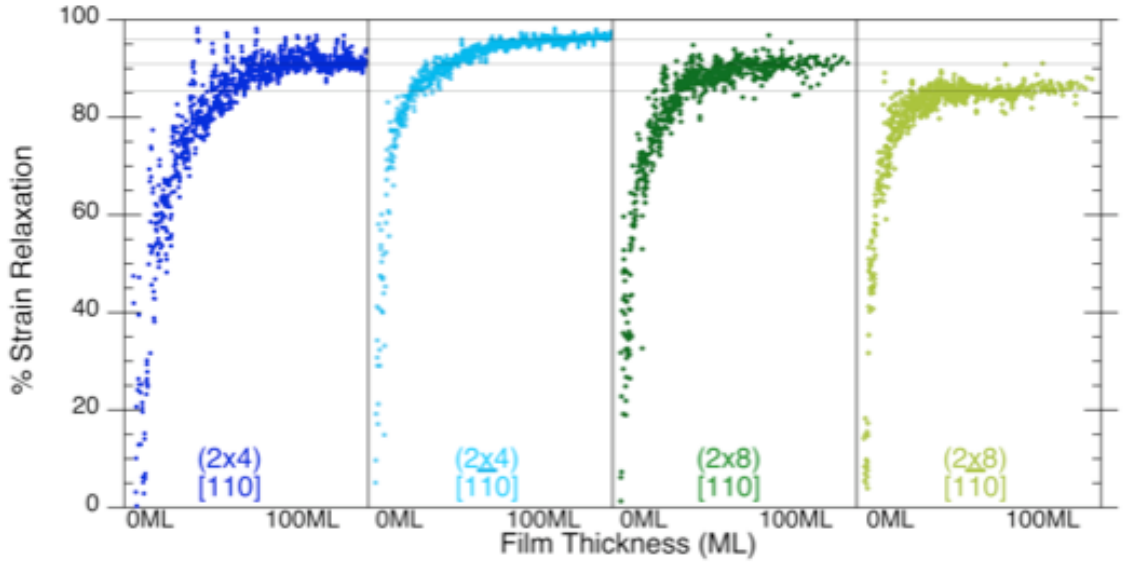

***Figure 5.3**: Percent strain relaxation of 100ML GaSb grown on a (2x4) and (2x8) reconstruction. The width of each box is 100ML.*

MOS data was collected during the film deposition on the (2x4) sample and during both the formation of the (2x8) reconstruction and the subsequent film growth on the (2x8) sample. There was no change in curvature, κ(t), when the (2x8) surface was initially exposed to Sb. Some change was seen as the wafer was cooled to the growth temperature, but this is common for all wafers. The MOS data collection was then stopped and restarted to separate the data collection of the (2x8) surface development and the sample film growth. Thus, all the strain relaxation reported can be attributed to the growth of the 100ML GaSb film and not to the initial formation of the surface reconstruction.

Figure 5.3 shows three regimes: (1) an initial fast relaxation of strain, (2) a transition with a decreasing slope, and (3) a plateau where most of the strain has been relieved and the remaining strain remains constant. The (2x4) sample

curves are very distinct from one another and do not overlap when plotted together. The initial slopes of the curves are slightly different when plotted together, with the [110] displaying a slower strain relaxation. When the section (1) of the curves are fitted with a linear relation and an R^2 value greater than 0.7, an approximate slope can be determined for the curves of 2.1 and 2.5 for the [110] and $[1\bar{1}0]$, respectively. It should be noted that these slopes are approximate. They are fitted by excluding outliers and maximizing R^2, but calculation of the standard deviation of the slopes shows this value is large relative to the actual slope. However, this relative slope is confirmed by visually analyzing the deviation from linearity at 15ML and 11ML for the [110] and $[1\bar{1}0]$, respectively. Despite this initial deviation, both curves plateau at approximately the same point, 200s or 60ML into the growth. The [110] relieves less strain, only 91% relative to the $[1\bar{1}0]$ which relieves 86% of the strain in the sample.

Initially, the curves of the (2x8) overlap well when plotted together. Calculation of the slope shows both are ~3.3, which is significantly faster initial relaxation than the (2x4) sample. They plateau out at slightly different times, with the $[1\bar{1}0]$ reaching the plateau region at ~30ML, and the [110] reaching the plateau region at ~40ML. In this case, the [110] relieves more strain than the $[1\bar{1}0]$ at 92% and 85%, respectively. Overall, the most important things to note are that the (2x4) relieves more strain than the (2x8) sample but requires more time to fully relax, whereas the (2x8) relieves less of the total strain, but does so more quickly in the growth.

The difference in the amount of strain relieved and the amount of time needed to relieve the strain suggests that there are distinct differences between the (2x4) and (2x8) samples in how atoms and defects are incorporated into the film. The difference along the $[1\bar{1}0]$ is initially surprising, since both reconstructions exhibit a periodicity of 2 along this direction. Re-examination of the atomic structure, seen in Fig. 2.1, suggests why this difference occurs. The (2x8) structure has a backbone of anion dimers that connect adjacent unit cells along the $[1\bar{1}0]$. This backbone will greatly impact strain relaxation in this direction as the dimers are pushed closer together or pulled further apart from one another. This backbone limits the amount of compression/tension that can

be accomodated along this crystallographic direction, as is evidenced in the lower amount of strain relaxation seen for the (2x8) along this direction. The orientation of the surface anion dimers parallel to the $[1\bar{1}0]$ for the (2x4) reconstruction may allow for slightly more compression, as it is limited only by overlap of dangling bonds rather than stretching of surface bonds.

The similarities between the two structures along the [110] also accounts for the similar strain relaxation along this direction. Along the [110], both structures exhibit a cation-cation bond as well as a trench dimer. This cation-cation bond is typically under tension. Thus, when the bond is broken in order to incorporate an Sb atom, this will relieve the strain within it. The [110] may also better relieve strain due to variation in reconstruction height along this crystallographic direction. If little or no surface As diffusion is assumed, the initial ML of deposited material will fill in the surface layer, resulting in a mixed Sb-As layer along the [110]. The lack of height variation of both reconstructions along the $[1\bar{1}0]$ limits the possibility for this type of relaxation in the opposite direction.

The RHEED and MOS data suggests that there are distinct differences in the films that grow on the (2x4) and (2x8) reconstruction surfaces. This is also reflected in AFM data of the two surfaces, as shown in Fig. 5.4. The (2x4) and (2x8) reconstructions both result in surfaces where there are large quantum dot (QD) islands surrounded by smaller dots, but the samples appear very different visually with regards to the shape and density of the smaller dots.

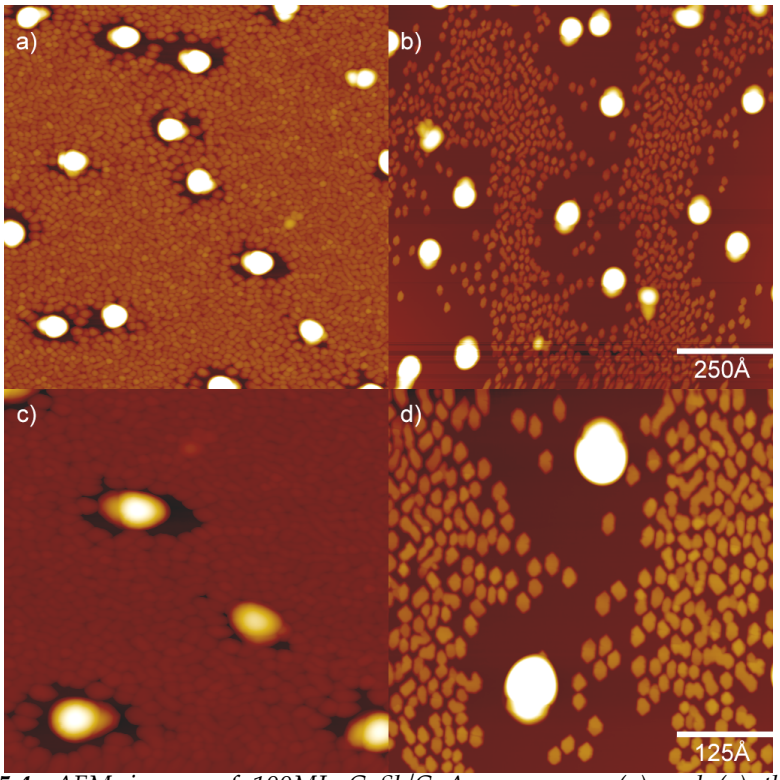

***Figure 5.4**: AFM images of 100ML GaSb/GaAs grown on (a) and (c) the (2x4) reconstruction and (b) and (d) the (2x8) reconstruction. (top) 10μm images and (bottom) 5μm images.*

The large QDs are very similar between the two samples. These dots are approximately round with basal areas of $354*10^3 \pm 69*10^3$ nm^2 and $387*10^3 \pm 82*10^3$ nm^2 for the (2x4) and (2x8) samples, respectively. The histogram of large QD size, displayed in Fig. 5.5, shows that the variation in dot size is small, in agreement with the relatively small standard deviation. The densities of the large dots are also very similar between the two samples at $1.43*10^{11}$/nm^2 and $1.74*10^{11}$/nm^2 for the (2x4) and (2x8) samples respectively. It should be noted that the large QDs in both samples often have a second dot that is adjacent to the large QD on one side. These second dots appear on multiple sides of the large dots, and TEM images show at least one case of a large dot with a second dot adjacent to it for the (2x4) sample, so this is not an AFM artifact. For statistical determinations, these double dots have been treated as a single dot due to the difficulty in accurately determining the height and area of the smaller dot. Due to this approximation, the actual area of the dots is slightly over estimated. For both samples, there is also a denuded area around the large QDs. The presence of this denuded zone suggests that the material directly adjacent the dots is all

quickly incorporated in the large QDs. The larger denuded area around the dots in the (2x8) sample suggests there may be differences in diffusion length on the two sample surfaces.

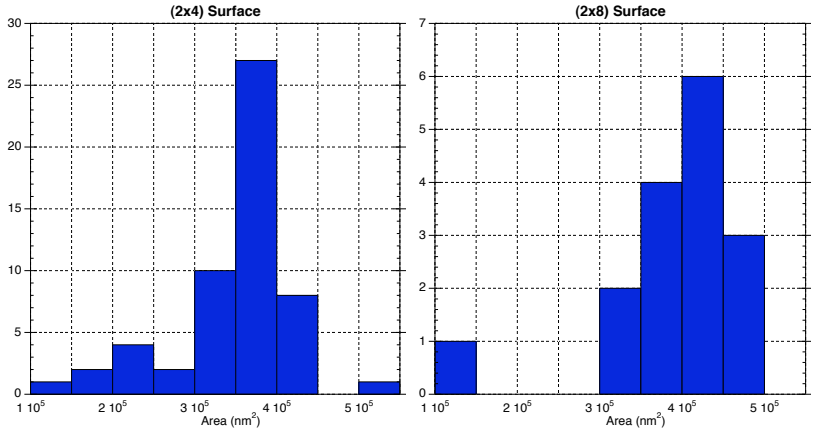

***Figure 5.5**: Area of large QDs grown on the (2x4) and (2x8) reconstruction surface.*

The dramatic topographical difference between these two samples is manifested in the shape, size, and particularly density of the smaller dots. On the (2x4) sample, the small dots are very densely packed and tend to agglomerate into large chains of dots. The density of the small dots is $3.26*10^{13}/nm^2$, and they cover ~89% of the sample surface, which is much larger than the 5% of the surface covered by the large QDs.

The small islands grown on the (2x8) surface are drastically different from those on the (2x4) surface. The density of the small dots is almost three times smaller than for the (2x4) surface, at only $1.09*10^{13}/m^2$, resulting in the observed lower surface coverage of the small dots. The shape of the small islands is also significantly different, with the small dots exhibiting facets. The dots resemble hexagons elongated along the $[1\bar{1}0]$, with points forming at the tips oriented along the $[1\bar{1}0]$ as shown in Fig. 5.6. The elongation and the formation of facets in these islands may suggest that diffusion is faster along the $[1\bar{1}0]$ in the (2x8) sample. This is in agreement with the fact that the denuded zone around the large QDs appears longer along the $[1\bar{1}0]$ than the [110]. This is reasonable since Sb has been shown to increase the diffusion rate of Ga on GaAs [3]. The surface reconstruction is also known to dramatically impact atomic diffusion on the

surface with the $[1\bar{1}0]$ being the fast diffusion direction for the α2(2x4) and β2(2x4) in InAs/GaAs thin films [4].

***Figure 5.6**: Schematic of small island shape grown on (2x8) reconstruction surface.*

For both samples, 100ML of material was nominally deposited. Yet, with the dramatic differences in surface topography, it is unclear how much material was incorporated. This determination requires a knowledge of the heights and profiles of the different dots.

Particularly for the (2x4) sample, determination of the height of either the small or large dots is very difficult with AFM due to the difficulty in determining the relative substrate height. For this reason, TEM was used to examine the dots. A montage of TEM images of small dots and one large QD on the (2x4) sample surface is shown in Fig. 5.7. Analysis of TEM images of 38 small and 5 large dots shows that these small dots are 48 ± 5nm in height, compared to 153 ± 28nm for the large QDs. This height is accurate for the small dots due to the shape of the dots, which resemble hemispheres with the top removed. Thus, the height is constant through a large percentage of the dots, resulting in an accurate height measurement. The height of the larger dots is underestimated because the sample set is small and the probability of hitting a dot center is also very low. Multiple line scans were flattened by a third order polynomial flattening function and normalized in height such that the minimal point on the surface is zero. These line scans are plotted in Fig. 5.8. These profiles indicate the small dots are ~50nm in height, in agreement with the TEM analysis. This agreement with the TEM height of the small dots means the determination of the substrate position is accurate and allows for a more accurate height determination for the large dots of 252 ± 55nm.

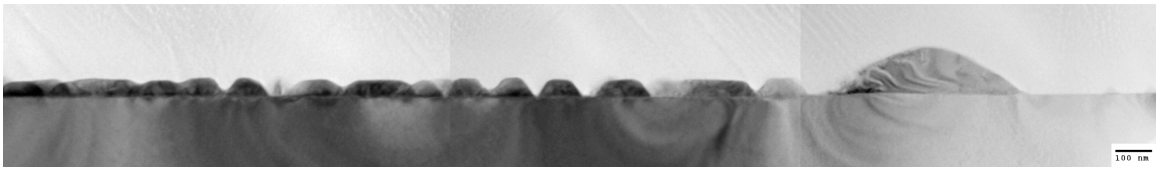

***Figure 5.7**: Montage of TEM images of small and large dots grown on the (2x4) surface.*

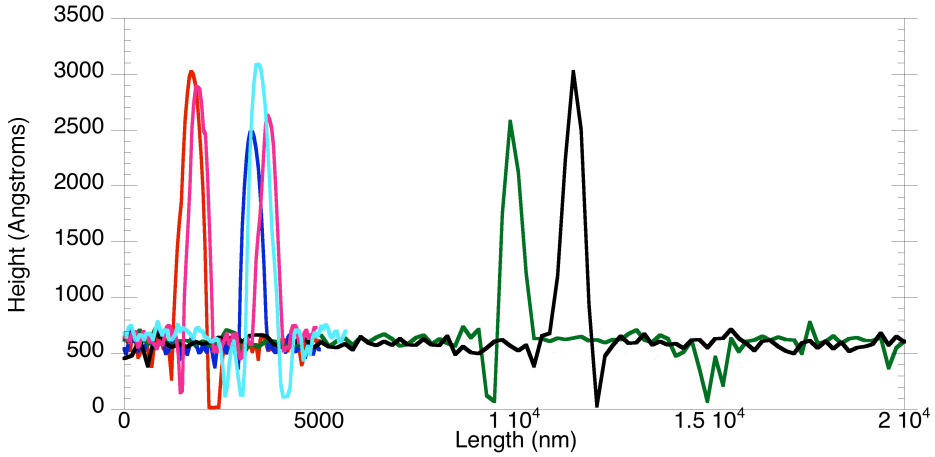

***Figure 5.8**: Line profiles of large and small dots on the (2x4) sample.*

Using the height and surface coverage, the amount of material incorporated onto the surface can be estimated. The large dots are almost hemispheres, but they do not have an equal radius for their base and height. Generally for a hemisphere:

$$V = \frac{2}{3}\pi r^3 \tag{5.3}$$

Accounting for the difference in basal radius and height means that the large QDs can be approximated as:

$$V = \frac{2}{3}Ah \tag{5.4}$$

where A is the basal area and h is the dot height. The factor of π is included in the basal area. The results show that the large QDs have an average volume of $4.7*10^7$ nm^3. Given the density of these dots, this correlates to a volume/area or an incorporated thickness of 6.7nm or 22ML.

The smaller dots on the (2x4) sample resemble truncated hemispheres. The volume can be broken into two components – a cylinder that describes the center of the truncated hemisphere and the rest of the volume, which is almost triangular – and can thus be approximated by the integral:

$$dV = 2\pi rh(r)dr \tag{5.5}$$

Solving this equation gives:

$$V = \pi r_1^2 h + (\pi r_2^2 - \pi r_1^2)\frac{r_2 h}{r_2 - r_1} - \frac{2}{3}\frac{h}{r_2 - r_1}\pi(r_2^3 - r_1^3) \tag{5.6}$$

where r_1 is the average radius at the top of the islands, and r_2 is the average radius at the bottom of the islands, and h is the average height. r_1 and r_2 are determined from TEM image analysis of 15 dots. The result is that the smaller dots have an average volume of $2.0*10^5$ nm^3. Given the density of these dots, this correlates to a volume/area or an incorporated thickness of 12nm, or 40ML. Adding this to the thickness in the large islands, this corresponds to an incorporated thickness of 19nm, or 61ML. This is lower than the "deposited" amount of 100ML. This is a lower bound to the amount of material incorporated due to the difficulty in identifying individual islands for the density due to island agglomeration. A second method of approximating the volume of the smaller islands is to multiply the approximate surface coverage and the average island height. This results in an incorporated thickness of 38nm, which is much larger than the previously calculated 19nm. This value is an overestimate because it assumes the islands have a constant area through the entire height of the dot, which, as is seen from the profile, is not the case. It does suggest that the actual amount of material incorporated may be higher than the calculated amount of 61ML.

A similar calculation can be performed for the (2x8) surface. The average height of the islands is significantly larger than for the (2x4) sample. The small dots are 102 ± 25nm in height, compared to 50nm, and the large dots are 356 ± 60nm in height, compared to 250nm. An analysis of the material incorporated into the surface for the large dots (assuming a hemisphere as before) shows an incorporation of 12nm, or 40ML.

The smaller islands are harder to analyze due to their shape. A TEM montage of the small islands is shown in Fig. 5.9, which shows them to be flat over most of the dot with an almost triangular shape at the edges. If the islands are assumed to be brick-like in shape – i.e. the island area is constant over the entire island height, ignoring the triangular edge – then volume = area*height, resulting in an incorporation of 40nm, or 132ML. This is much thicker than the

amount of film deposited and so assumptions must be made for the fact that the islands edges appear triangular. Using TEM images and averaging over 6 islands, it can be shown that the ratio of the length of the top edge to the bottom edge is 0.73. The volume can be approximated as:

$$V = V_1 + \frac{1}{2}(V_2 - V_1) \tag{5.7}$$

where V_2 and V_1 are the volume of a brick-like hexagon with side length 2 and 1, respectively. Solving this gives a modified incorporation of 31nm or 100ML. This is still large, which can be attributed to the rough approximation of the volume and the fact that the shape is not an exact hexagon, but the value is much more reasonable. Combining this value with that of the large dots gives a total incorporated thickness of 43nm or 141ML. This is greater than the amount of material deposited (100ML), suggesting that the approximations in this incorporation need further refinement. A small sample set was available from the TEM analysis and slight differences in island rotation and the fact that the islands are not perfect hexagons may contribute to error in the calculations. This value does suggests that most of the material deposited on the surface is incorporated either into the small or large dots.

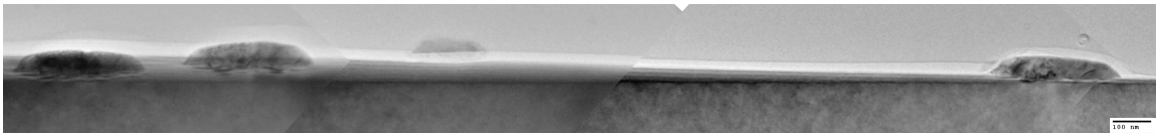

***Figure 5.9**: TEM montage of small islands grown on (2x8) reconstruction surface. Note: some shadowing appears in this image due to the high sample tilt required to bring the sample to a zone axis orientation.*

This analysis assumes that all the material incorporated is incorporated into the islands and that there is limited diffusion and exchange of material between the substrate and the islands. This is a reasonable assumption because Sb is a known surface segregant while As is not, which should limit the diffusion of Sb into the bulk and As into the islands. This can be confirmed by analyzing electron diffraction patterns and FFTs of TEM images. Figure 5.10 shows electron diffraction patterns including both the QDs and the substrate. As can be seen in the image there are double diffraction spots for each point in both the (2x4) and (2x8) samples, suggesting two lattice parameters. FFT patterns of high resolution images show the same double spot pattern. Inverse FFT (IFFT) images

of the inner and outer dots show two different lattice parameters for the dots and substrate, showing that the GaSb is incorporating in the QDs. In neither case is it clear whether a wetting layer of GaSb exists or not; it would be very thin (<3ML) which would be difficult to discern using this analysis.

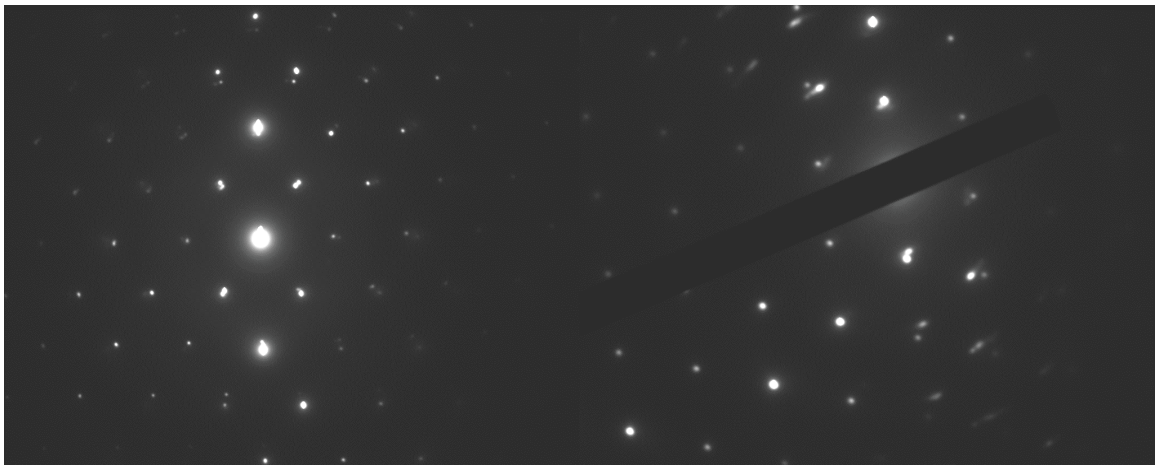

***Figure 5.10**: Diffraction patterns from left to right of the sample grown on the (2x4) and (2x8) surface. Note: the central transmitted spot has been blocked for imaging purposes in the (2x8) pattern.*

Further analysis of the (2x4) sample shows that the strain is relieved by two mechanisms, stacking faults and edge dislocations, both of which can be seen in Fig. 5.11. The edge dislocations often consist of two ½ planes of atoms that terminate at the boundary between the film and substrate. The extra planes extend into the GaAs substrate, as is expected due to the larger lattice parameter of GaSb. The dislocations are spaced at ~15 lattice planes apart.

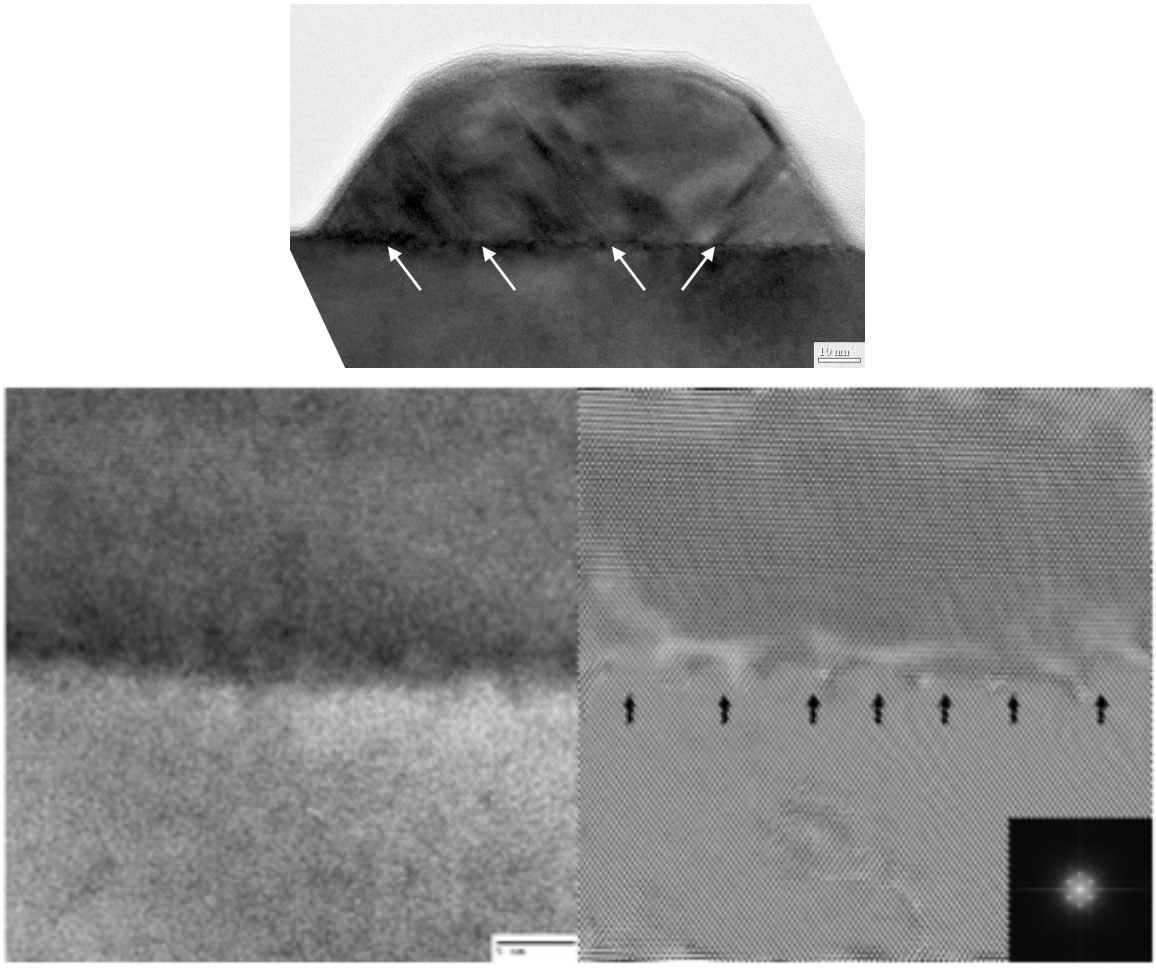

***Figure 5.11**: (top) TEM image of stacking faults and (bottom) TEM image and inverse FFT TEM image of edge dislocations grown on the (2x4) sample. The FFT of the original HRTEM image is inset in the lower right corner of the filtered image.*

Analysis of the diffraction pattern, as well as some of the FFT patterns, for the (2x8) sample shows that the additional spots are rotated relative to those of the substrate. This suggests the presence of a tilt boundary, which is visible in TEM images such as the one shown in Fig. 5.12. The top image shows a 5° tilt boundary which, together with the array of dislocations visible in the lower image, relieves the strain. In this case, the tilt disappears when the dislocations appear and vice versa. The dislocations have no apparent regularity in their spacing.

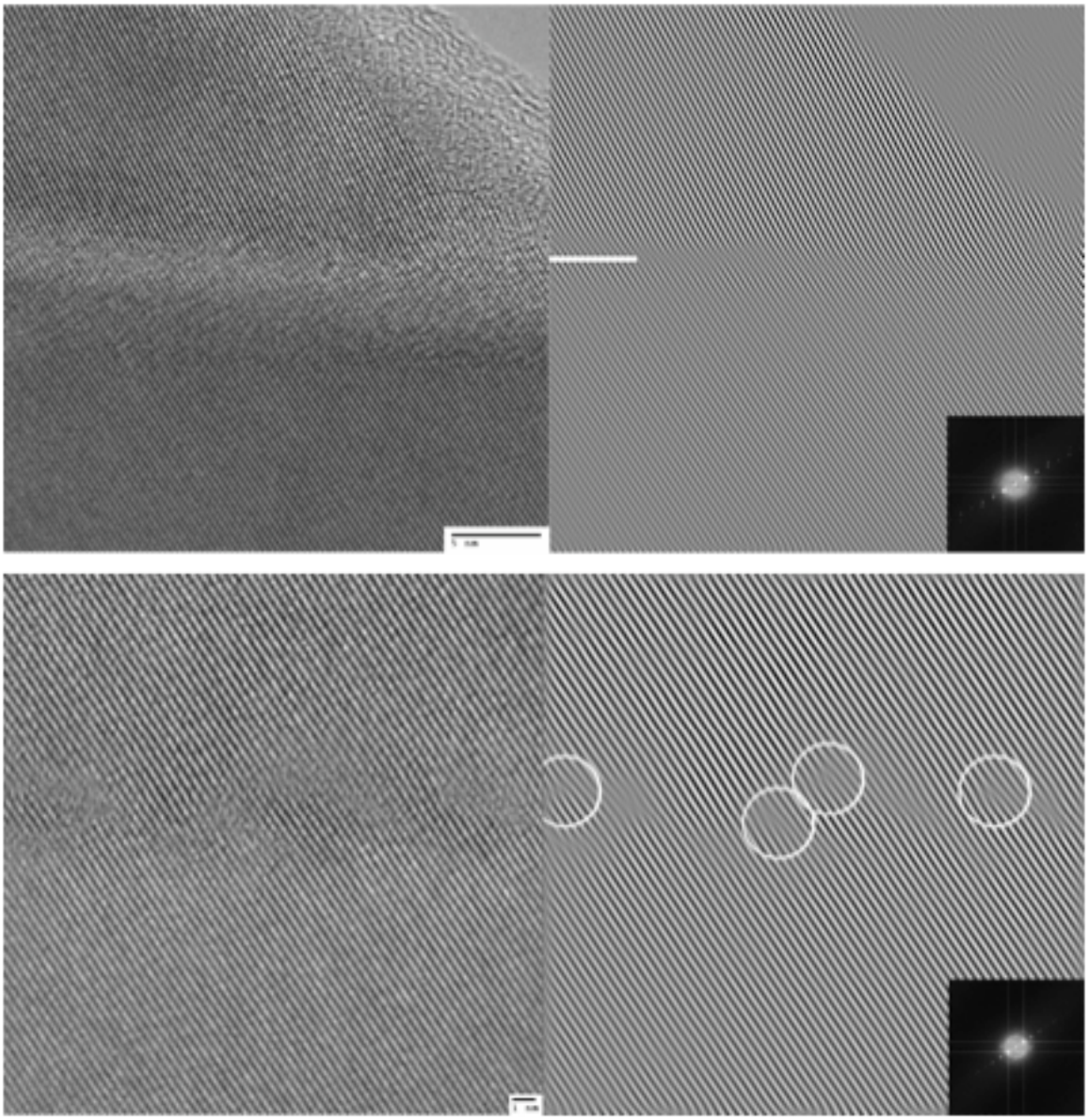

***Figure 5.12**: TEM and inverse FFT TEM images of (top) 5° tilt boundary and (bottom) dislocations from (2x8) sample. The FFTs of the original HRTEM images are inset in the lower right corner of the filtered images.*

The results presented here show that there is a distinct difference in the surface topography, defect structure, and strain relaxation between samples grown on a (2x4) and (2x8) reconstruction surface. This shows that the initial incorporation of atoms onto the surface greatly impacts the film development, which has been suspected but has not been closely examined previously. This work was motivated by the hypothesis that differences in defect structure seen by the Huffaker group [5-9] might be explained, not by differences in flux, as was originally postulated by the group [6], but by differences in surface structure

resulting from how the Sb rich surface was prepared [5]. The resulting defect structures obtained in this work do not correlate with the previous work. The RHEED patterns of the (2x4) sample generally resemble those reported by Huffaker *et al* [6], who demonstrated a very spotty pattern for structures grown on a (2x4) reconstruction with a low V:III ratio. The (2x8) pattern does not display the chevron pattern [6] associated with the 90° misfit dislocation array. The resulting defect structures are also different from those previously reported. The structures obtained in this work exhibit a stacking defect and misfit array for the (2x4) and a tilt boundary and irregularly spaced defects for the (2x8) rather than the previously reported threading dislocations for V:III poor and misfit array for V:III rich [6]. These differences may stem from slight differences in procedure or slight variations in temperature. A test sample was grown for this study on a substrate that was In mounted onto a Mo puck. The RHEED pattern that resulted from growth on a (2x8) surface reconstruction was a chevron pattern similar to that obtained by the Huffaker group [6]. This suggests that the free-mounting technique used for obtaining MOS data alters how quickly the sample adjusts to slight fluctuations in temperature compared to the In mounting technique on Mo pucks used for many III-V sample growths. Thus, the MOS studies may require re-optimization of growth in order to match the In mounted results. Two other possible reasons for the differences between this and previous work are: (1) the samples were grown at slightly different temperatures (525°C rather than 500°C), and (2) slight procedural variations may result in the presence of more or less As in either chamber due to how the material source valve and shutter are activated. Either of these differences may dramatically impact the initial incorporation of Sb in the film.

ii. Interaction of Dislocations and Surface Reconstructions

The differences in defect structure obtained when the same sample is grown on two different surface reconstructions suggest that there is some interaction between the surface reconstruction and defect. An array of edge dislocations is the ideal defect structure for device applications due to the fact that these dislocations are localized at the interface between layers and do not thread through the film to act as non-radiative recombination locations. This

array of edge dislocations has been seen experimentally, [6,10] and is shown in Fig. 5.11. The structure of the edge dislocation in GaSb/GaAs seen experimentally is an arrowhead [10], where two planes of GaAs come in and terminate at a single point. This defect structure is common to diamond and Zinc Blende crystal structures. It has been studied for Ge/Si crystals, and the structure of this defect is shown in Fig. 5.13 [11]. The same structure has been suggested for the III-V semiconductors and has been studied for GaAs where it is shown that the bond formed at the termination of the two half-planes is of Group III atoms [12].

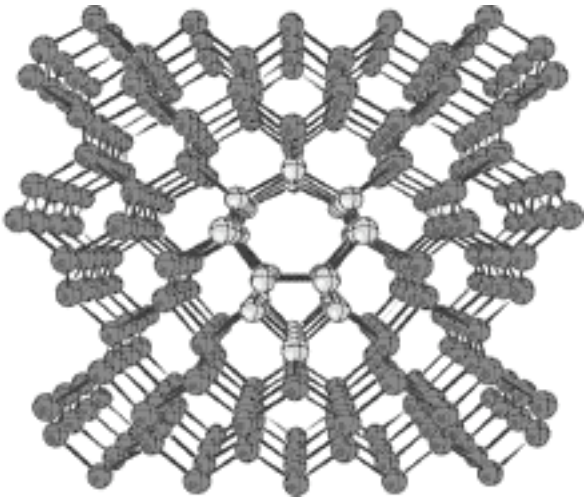

***Figure 5.13**: Dreidal structure of a 90° edge defect imaged along the <110> with two ½ planes of atoms at the bottom of the structure that terminate at the defect. Taken from [11].*

In order to examine the interplay between a surface reconstruction and an edge dislocation, computational runs were performed as described in II.ii.b. Slabs were prepared with an edge dislocation at the interface between a GaAs and GaSb layer beneath either a (2x4) or (2x8) GaSb surface reconstruction. Some relaxed structures can be seen in Fig. 5.14 (left). The relative positions of the dislocation and surface reconstruction were shifted in order to examine the lowest energy position of the dislocation with respect to the surface. Due to the periodicity of the surface, eight positions were examined and these positions are labeled in Fig. 5.14 (left). Due to the structure of the α2(2x4) reconstruction there are two possible orientations of adjacent unit cells. One of these is plotted as the structure in Fig. 5.14, with the alternate structure in grey. The energies of each of these positions are normalized relative to the lowest energy position and are

plotted in Fig. 5.14 (right). There are two curves for the α2(2x4) structure for the two possible structure orientations. The absolute energies between different structures cannot be compared due to changes in stoichiometry, but the relative energetic changes within each structure can be compared. These relative changes can be very dramatic with up to a 2eV change for moving the dislocation across the unit cell, as seen for the α(2x8) structure.

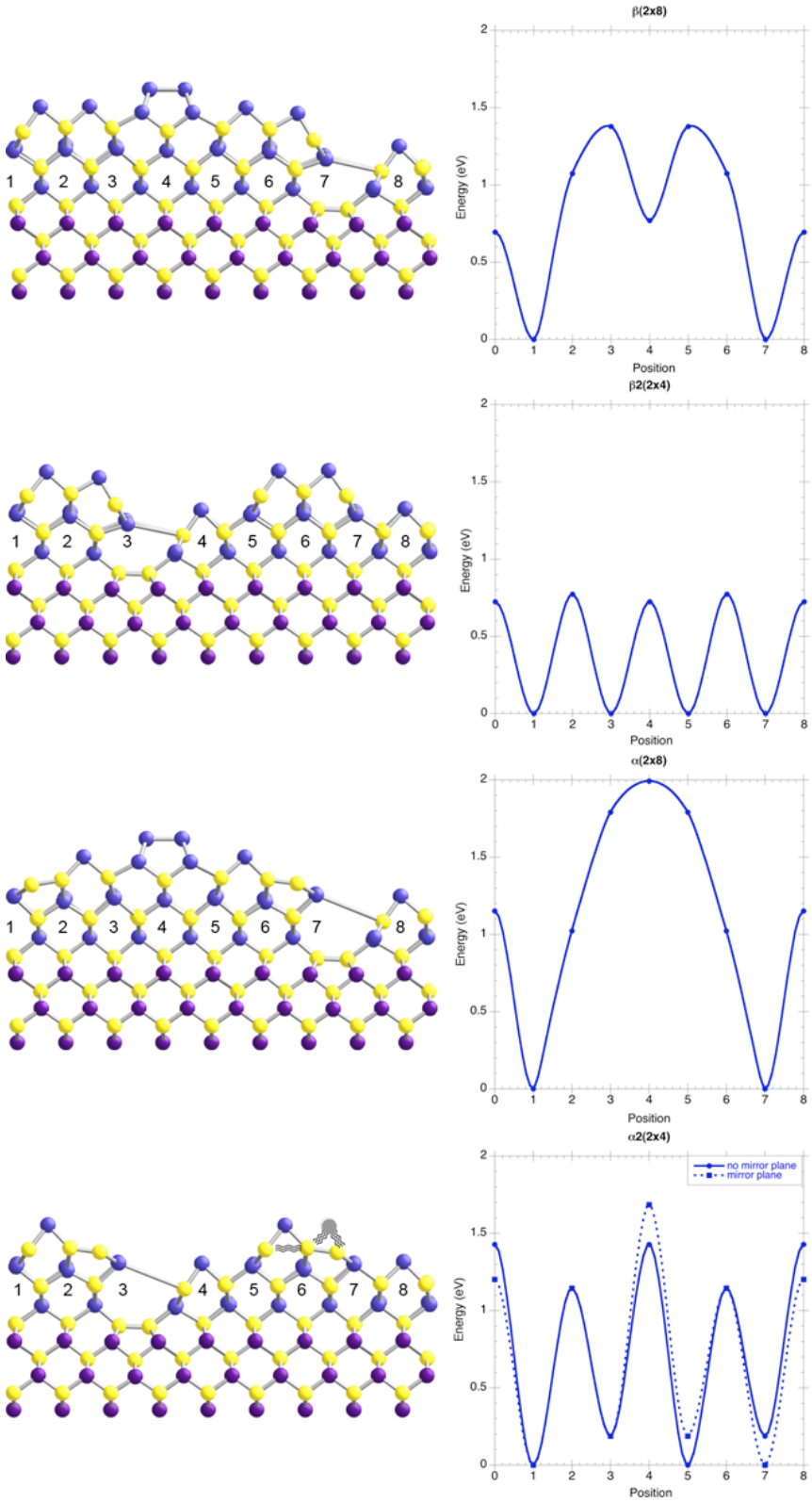

***Figure 5.14**: Top to bottom, (left) structure and (right) energy as a function of position for a dislocation under a β(2x8), β2(2x4), α(2x8) and α2(2x4) reconstruction. Energy normalized to lowest energy per reconstruction.*

The lowest energy configurations for each structure are shown in Fig. 5.14 (left). In each case the lowest energy position is adjacent to the trench dimer in the position between the trench and the rest of the reconstruction – positions 1 and 7 for the (2x8) reconstruction and positions 1, 3, 5 and 7 for the (2x4) reconstructions. As can be seen in Fig. 5.14, this edge position allows one Sb-Ga bond to stretch very dramatically. The different configurations possible in the α2(2x4) reconstruction indicate that the lowest energy position is not only adjacent to the trench dimer, but also adjacent to a surface anion dimer rather than a cation-cation backbond. By altering the orientation of adjacent α2(2x4) unit cells, three different configurations are possible: (1) adjacent surface Sb dimers on both sides, (2) adjacent Ga-Ga backbonds on both sides, or (3) a surface Sb dimer and a Ga backbond on opposite sides. This induces some significant changes in energy seen in Fig. 5.14(bottom-right). The solid curve corresponds to the configuration shown and the dotted curve represents the gray alternate configuration. From the energy curves, it is clear that the lowest energy configuration occurs when the dislocation sits between the trench dimer and a surface anion dimer, such as position 5.

Wherever it is placed, the dislocation greatly stretches the Sb-Ga bond because it increases the local spacing between the Sb atoms attached to the Ga-Ga terminating bond. This induces a tensile stress that stretches the local bonds above the dislocation. The presence of this tensile stress explains why the positions adjacent to the trench are the lowest energy positions within the (2x8) unit cell. At the trench edge, the relative 'height' of the reconstruction is lower which means there are fewer bonds that must be stretched in order to accommodate the dislocation. The Sb-Ga bond directly above the dislocation is greatly deformed and the local region adjacent to the dislocation shows some deformation. Examining this deformation allows an understanding of why the dislocation is lower in energy when placed between the trench and a surface dimer rather than the trench and a cation-cation backbond. As can be seen in the β2(2x4) and β(2x8) reconstructions, when the dislocation is placed adjacent to a surface dimer, the adjacent dimer tilts towards the trench, limiting the amount of deformation in the Sb-Ga bond directly above the dislocation. However, when

the dislocation is placed adjacent to a cation-cation backbond, as is shown for the α(2x8) and α2(2x4) reconstructions, the relative tension in the cation-cation backbond does not allow for relaxation of the surface reconstruction in the [110] direction and results in a significantly higher deformation in the Sb-Ga bond directly above the dislocation.

Similar analysis of the strain and bonding structure explains why the dislocation is not stable in other positions within the unit cell. The initial hypothesis for this work was that the lowest energy positions within the unit cell would be beneath the trench dimer (position 8 for the (2x8) and positions 4 and 8 for the (2x4)) or beneath the top-most anion dimers within the reconstructions (position 4 in the (2x8) or positions 2 and 6 in the (2x4) reconstructions). However, these positions are all significantly higher in energy than the position adjacent the trench dimer. Placing the dislocation underneath the $[1\bar{1}0]$ oriented trench dimer or underneath the $[1\bar{1}0]$ oriented surface dimers in the (2x4) reconstruction is high in energy due to the symmetry of these positions. The Sb atoms directly above the dislocation in these positions are four-fold coordinated, and any displacement of the atoms in any direction will stretch and compress one pair of bonds with little to relieve the induced strain. Placing the dislocation beneath the surface Sb dimer in the (2x8) reconstruction is high energy due to the relative orientations of the dislocation and the dimer bond. The dislocation Ga-Ga bond is oriented along the [110] and the topmost Sb-Sb dimer bonds are oriented along the [110] as well. A dimer forms by displacing two Sb inward to form a bond, and the bond energy increases as the bond is stretched outward because of the dislocation. Thus, placing the dislocation in position 4 in the (2x8) reconstruction, below the Sb-Sb surface bond, is high in energy because the bond cannot be stretched without greatly increasing the energy of the surface reconstruction.

The relative energies of the reconstructions to each other can be determined by normalizing the energy relative to a reference state. The surface energies can then be plotted as a function of chemical potential and compared. This was done in Chap. III and IV using the method described by Wixom *et al.*

[13]. Wixom shows that the surface energy of a reconstruction slab, such as this one, can be written as:

$$\sigma = E_{total}^{slab} - \Sigma n_i^{slab}\mu_i - N(E_{bulk}^{total} - \Sigma\mu_i^*) - \sigma_H^{surface} \quad (5.8)$$

where σ is the surface energy of the reconstruction, $\sigma_H^{surface}$ is the surface energy of the H-terminated surface, n_i and μ_i are the number and chemical potential of constituent species, μ_i^* is the chemical potential of the bulk reference species, N is the number of bulk units of the bulk reference state, and E_{total}^{bulk} is the reference state of binary, bulk material. In other words, equation 5.8 describes the energy of a surface taken with respect to a reservoir of bulk binary material described by the reference state E_{total}^{bulk}. Due to the fact that the reference state is a reservoir of material, N can be taken to be any number, including zero. Thus a plethora of different equations can be generated for σ by choosing different values of N, but all values of N predict the same relationship between reconstructions, i.e. the chemical potential at which a transition occurs between two different reconstructions is unaffected by the choice of N [13].

For the binary systems studied up to this point, the reference state is the binary bulk material and N is taken as n_{III}. In the GaSb/GaAs case described here, the most valid reference state is pure GaAs at the GaAs lattice parameter. Choosing this reference state means that the calculated surface energy includes the energy to form the Sb-Ga-As interface, the energy to create the dislocation, and the energy to create the GaSb film and surface. N is chosen to be $N = n_{As} - \frac{1}{4}n_H$ in order to cancel all As dependence resulting in a surface energy that is only a function of μ_{Ga} and μ_{Sb}.

The resulting graph is a set of planes, where the lowest plane at a specific μ_{Ga} and μ_{Sb} is the stable surface reconstruction. The bounds are defined as previously. For a reconstruction to be stable, it must have the lowest surface energy for a set of chemical potentials, μ_i, where the allowable range of μ_i is defined by the growth of bulk material. However, μ_{Ga} and μ_{Sb} are not independent variables. The requirement that the surface chemical potentials be in equilibrium with the bulk chemical potentials leads to the relationship:

$$\mu_{Ga} + \mu_{Sb} = \mu_{GaSb(bulk)} = E_{Ga(bulk)} + E_{Sb(bulk)} - \Delta H_f^{GaSb} \quad (5.9)$$

where $\mu_{GaSb(bulk)}$ is the energy of a GaSb pair at the defined lattice parameter [14]. Typically, this relation is simplified one step further to define bounds on a single chemical potential such that:

$$\mu_{Sb(bulk)} - \Delta H_f^{GaSb} \leq \mu \leq \mu_{Sb(bulk)} \qquad (5.10)$$

These values have been used to bound the graphs displayed in Chap. III and IV. In this case, these bounds are used, but the relation shown in eq. 5.9 is also used and it is this line that defines the accessible surface reconstructions.

In order to prove that the choice of N does not change the phase stability, the surface reconstruction phase stability diagram of the α2(2x4), β2(2x4), α(2x8), and β(2x8) reconstructions plotted in Fig. 4.15 with $N=n_{III}$ is replotted in Fig. 5.15 with N=0. Planes that are a function of both μ_{Ga} and μ_{Sb} replace the lines that plotted in Fig. 4.15 as a function of only μ_{Sb}. Fig. 5.15a displays the projection of these planes where the lowest energy plane at any given chemical potential pair is plotted. The horizontal axis is μ_{Sb}- $\mu_{Sb(bulk)}$ and the width of the graph is ΔH_f, as previously displayed in Fig. 4.15. The vertical axis is μ_{Ga}- $\mu_{Ga(bulk)}$. The dotted line in the graph is eq. 5.9, where $\mu_{GaSb(bulk)}$ is the bulk energy of GaSb at the GaAs lattice parameter. Following this line, it is clear that the stable reconstructions as a function of increasing μ_{Sb} remain the α2(2x4), α(2x8), and β(2x8), and the intersection points of -0.22 for the α2(2x4)-α(2x8), and -0.15 for the α(2x8)-β(2x8), are maintained.

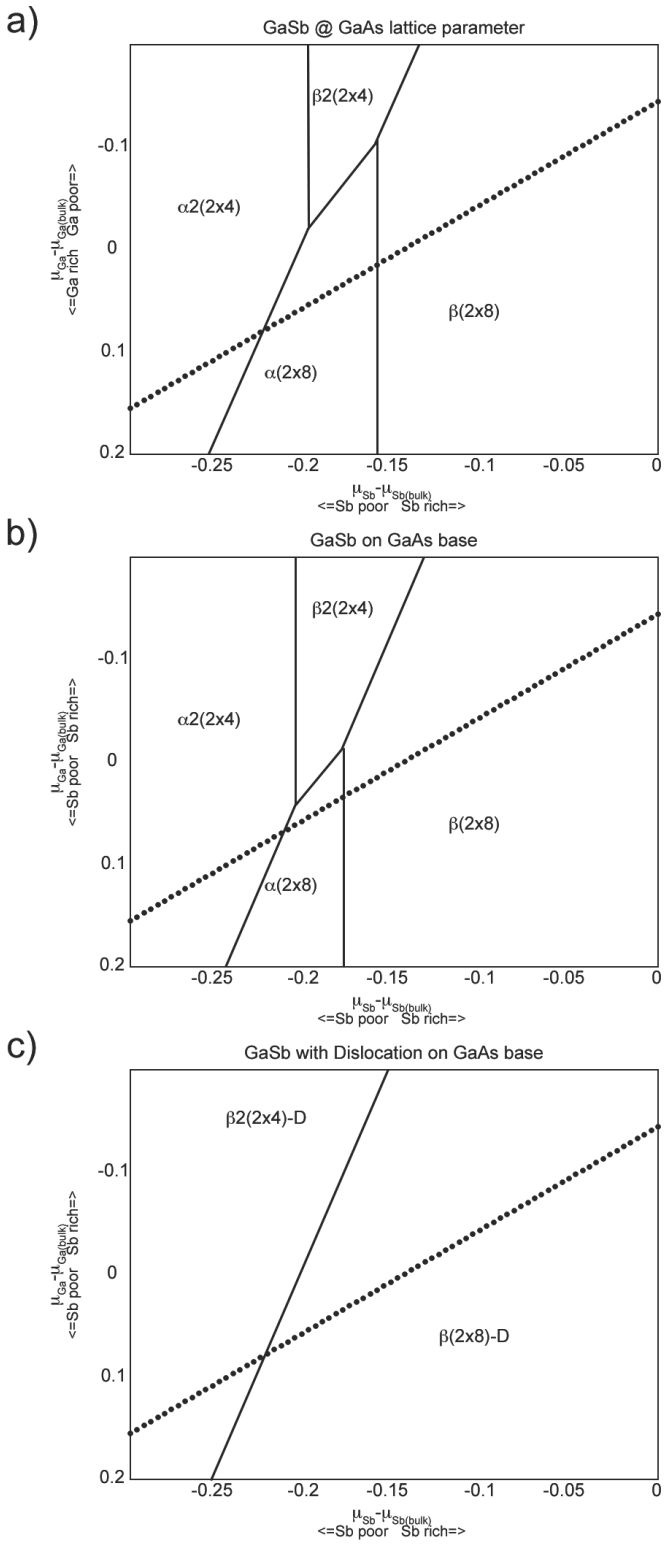

***Figure 5.15**: Lowest energy surfaces of (a) pure GaSb at the GaAs lattice parameter, (b) (2x4) and (2x8) surface reconstructions of GaSb on a GaAs base at the GaAs lattice parameter with (-D) and without an edge defect, and (c) (2x4) and (2x8) surface reconstructions of GaSb on a GaAs base at the GaAs lattice parameter with (-D) an edge defect.*

The positive values for μ_{Ga}- $\mu_{Ga(bulk)}$ must be addressed. The method for calculating bounds is determined as described above for binary homoepitaxially grown films. In that case, eq. 5.9 leads directly to eq. 5.10. The values of $\mu_{Sb(bulk)}$ and $\mu_{Ga(bulk)}$ are determined by relaxing bulk crystals of Sb and Ga under the same energy cut-off parameters of the examined slabs. The calculated energies can be used to determine the enthalphy of formation, ΔH_f, thus providing the complete bounds on chemical potential. There are some limitations to this in that Sb forms multiple crystal structures and Ga is liquid at just above room temperature, so it is necessary to confirm that the results obtained are reasonable based on experiment, as has been done in the previous chapters. As discussed in IV.ii.d, the calculated ΔH_f is small compared to the experimentally determined value but it reproduces experimental surface structures well. This may be due to slight inaccuracies in the bulk energies due to the fact that Ga may be a liquid rather than a crystal. If the value of bulk Ga is calculated using an enthalpy of formation that is closer to experiment, the calculated bulk energy is ~0.2eV higher, which shifts the bounds such that there are no positive values. This may be the cause of the error in the bounds, but there is a second possibility. When plotting versus two chemical potentials, each should be bounded as suggested by eq. 5.10. This equation does not take into account the change in bulk energy due to strain. Plotting equation 5.9 on these graphs at the GaSb and GaAs lattice parameters shows a shift towards positive μ_{Ga} values when strain is included. Thus the inclusion of strain in the bulk reference energy may also cause some shifts in the accuracies of the bounds. The stability of the 2x8 has been compared to experiment and the bounds accurately reproduce experimental values. Thus the positive value on the Ga bound can be attributed to these two affects.

Figure 5.15b shows the energies of GaSb (2x4) and (2x8) reconstructions on GaAs bases with (-D) and without dislocations. None of the surfaces with a dislocation have an energy below that of the surfaces without a dislocation. In general, the surfaces with dislocations are ~3eV higher in energy relative to those without. This shows that while there is a large interaction between the strain fields of the surface reconstruction, the dislocation has not sufficiently lowered the energy to be stable relative to the surfaces without dislocations. This

suggests a number of future experiments to determine the exact structure of the low-energy dislocation surface that will be discussed at length in the next section. It is interesting to note that the introduction of a GaAs-GaSb interface does appear to have an impact on the stability of the surface reconstruction. Comparison of Fig. 5.15a and 5.15b shows a shift in stability of the surface reconstructions relative to one another. The stable surface reconstructions do not change, remaining the α2(2x4), α(2x8), and β(2x8) with increasing μ_{Sb}. However, the relative crossover points compress and the α(2x8) is stable over a smaller range of growth conditions. The β2(2x4) reconstruction also comes closer to stability than for pure GaSb at the GaAs lattice parameter, though never quite becoming stable. This is interesting result because it suggests that there are some small chemical effects in alloying which alter the surface reconstruction stability. Generally, the Group III and Group V species are thought to be almost chemically identical because the similarities in their valence bands results in the same bonding structure. This change in stability due to the introduction of a GaAs/GaSb interface shows that changes in electro-negativity or other small differences between the two atoms may in fact impact the surface structure.

Figure 5.15c plots the lowest energy structures of the surfaces with dislocations in order to examine the relative energies of the reconstructions. It is clear from this graph that the beta structures are more stable than their alpha counterparts. This is probably due to the amount of deformation present in the Sb-Ga bond. The beta reconstructions were able to shift in order to better accommodate the strain in the surface, whereas the alpha reconstructions were less able to accommodate the strain due to the cation-cation backbond. This may be the determining factor that results in the beta structures being more stable.

iii. Conclusions and Future Work

This work shows that there is a strong correlation between the surface reconstruction and subsequent film growth. The experimental data presented shows that the reconstruction can impact strain relaxation, surface topography, and defect structures in this system. This has strong implications for the ability to engineer interfaces using different starting surface reconstructions. There is

some lack of agreement between the results shown here and those presented by other groups. Huffaker *et al*. achieved an array of misfit dislocations growing at high V:III ratios on a (2x8) surface [5, 7]. Kaspi *et al*. achieved an array of misfit dislocations on a (1x3) Sb-rich surface [10]. The results here indicate that an array of misfit dislocations are possible at low V:III ratios on a (2x4) substrate. Overall, the work here demonstrates that the surface reconstruction can have a dramatic impact on the development of dislocations and surface topography of grown films. Further refinement is required to determine the exact, reproducible, growth parameters to obtain particular defect structures.

The computational work shows that there is a large interaction between the surface reconstruction and a dislocation inserted into the film. The inserted dislocation sits in the lowest energy position within the unit cell, which, for these studies, is adjacent to the trench dimer and a surface anion dimer. This work examines a dislocation placed every 8 (or 9) bulk atomic positions for GaSb (or GaAs). The dislocation is at the interface between the GaAs 'substrate' and GaSb film, with the film reconstruction beginning immediately above the dislocation. There are some possibilities within this set-up which may account for the higher energy of the surfaces with dislocations vs. surfaces without dislcoations: (1) distance between dislocations, (2) 'height' of dislocation relative to the GaSb-GaAs interface, and (3) 'depth' of the dislocation relative to the surface reconstruction.

The placement of the dislocations at 8 atomic positions was chosen because of some of the limitations of DFT. The amount of time to relax slabs increases dramatically with increasing numbers of atoms. The cell is repeated infinitely in three dimensions in DFT, and so to examine a dislocation in the [110] in a (2x8) unit cell, the dislocation can be placed every 8 or 16 lattice positions. The initial choice to use 8 lattice positions was to minimize computational time, but this placement may result in an altered strain state for the dislocation. Experimentally, 90° edge dislocations are placed at ~14 bulk atomic positions [10] to fully relax the lattice mismatch strain between the GaSb and GaAs. Thus, when the dislocations are placed every 8 bulk positions, the lattice mismatch strain is *overcompensated* for and the resultant strain field, rather than relieving the compressive strain, introduces a slightly tensile strain into the film. This can

be seen in the way the dislocation is accommodated in Fig. 5.14, particularly in the alpha reconstructions. The high tensile strain causes the highly deformed Sb-Ga bond. While it is unclear from these results, this bond may be stretched to the point of no longer actually existing in these structures but rather introducing an As dangling bond and a Ga dangling bond. This tensile strain may also account for the higher energy of the slabs containing dislocations relative to those without dislocations. The correction is to re-run these calculations placing the dislocation every 16 lattice positions. This does not *quite* relieve all the induced compressive strain, but more accurately simulates the experimental results and the slightly compressive field may also alter where the dislocation sits relative to the surface reconstruction.

GaSb exhibits a SK type growth with $2.5 \leq h_c \leq 3.0$ML. After the introduction of 3D growth, there is some experimental evidence that the wetting layer is still partially present, as seen in Fig. 4.9f, though it was not conclusively seen in the TEM analysis of the two samples discussed in V.i. This suggests that the position of the dislocation may not be exactly at the GaAs-GaSb interface, but rather 1ML higher. Only 1ML is suggested due to the similarity of the GaSb/GaAs wetting layer in Fig. 4.9f to the h<0.8ML film shown in Fig. 4.1. Movement of the dislocation 1ML away from the interface may result in a slight increase in the strain energy over that 1ML, acting as a driving force to 'nucleate' the dislocation. The resultant release of energy may be enough to drop the energy of the entire slab relative to that of the slab without a dislocation.

The large deformation in the Sb-Ga bond due to the placement of the dislocation may increase the relative energy of the surface reconstruction. Insertion of 1ML of GaSb material between the dislocation and the surface reconstruction may mitigate the deformation seen as all the bonds above the dislocation will then be four-fold coordinated. Despite the fact that the lowest energy position is exactly adjacent to the trench dimer, the dramatic deformation of these bonds may be driving the surface energy higher, and addition of a ML of material may mitigate and balance this deformation.

The most likely reason for the high energy of the slabs with dislocations relative to the ones without dislocations is the fact that the dislocations are placed too close together and are overcompensating for the lattice mismatch

strain and introducing a tensile strain on the surface. As the strain field seen experimentally is either slightly compressive or neutral due to the dislocations, it is hypothesized that placing the dislocations at 16 bulk atomic units will bring the energy of the surfaces with dislocations below that of the ones without dislocations, which suggests the route of edge dislocation insertion in these films. Regardless of whether this postulation is correct, the work shown within this chapter demonstrates that there is a strong interplay between the strain fields of the surface reconstruction and that of the dislocation. The evidence of the impacts that surface reconstruction has on subsequent film topography and defect structure shows that understanding this relationship is important and may lead to interesting methods for engineering surfaces and defects within this system.

iv. References

1. I. G. Batyrev, A. G. Norman, S. B. Zhang, and S.-H. Wei, *Phys. Rev. Lett.* **90**, 026102 (2003).
2. S. Froyen, and A. Zunger, *Phys. Rev. B* **53**, 4570 (1996).
3. R. R. Wixom, L. W. Rieth, and G. B. Stringfellow, *J. Cryst. Growth* **265**, 367 (2004).
4. M. Rosini, M. C. Righi, P. Kratzer, and R. Magri, *Phys. Rev. B* **79**, 095302 (2009).
5. G. Balakrishnan, T. J. Rotter, A. Jallipalli, L. R. Dawson, and D. L. Huffaker, *Solid State Lasers XVII: Tech. and Devices* **6871**, 87111 (2008).
6. G. Balakrishnan, J. Tatebayashi, A. Khoshakhlagh, S. H. Huang, A. Jallipalli, L. R. Dawson, and D. L. Huffaker, *Appl. Phys. Lett.* **89**, 161104 (2006).
7. S. H. Huang, G. Balakrishnan, A. Khoshakhlagh, A. Jallipalli, L. R. Dawson, and D. L. Huffaker, *Appl. Phys. Lett.* **88**, 131911 (2006).
8. A. Jallipalli, G. Balakrishnan, S. H. Huang, A. Khoshakhlagh, L. R. Dawson, and D. L. Huffaker, *J. Cryst. Growth* **303**, 449 (2007).
9. J. Tatebayashi, A. Khoshakhlagh, S. H. Huang, L. R. Dawson, G. Balakrishnan, and D. L. Huffaker, *Appl. Phys. Lett.* **89**, 203116 (2006).
10. W. Qian, M. Skowronski, R. Kaspi, M. De Graef, and V. P. Dravid, *J. Appl. Phys.* **81**, 7268 (1997).
11. M. Mostoller, T. Kaplan, and M. Chisholm. "Edge Dislocations in Silicon" <http://www.ornl.gov/info/ornlreview/v30n3-4/edge.htm>
12. S. P. Beckman, and D. C. Chrzan, *Phys. Stat. Sol. (b)* **243**, 2122 (2006).
13. R. R. Wixom, N. Modine, and G. Stringfellow, *Phys. Rev. B* **16**, 115309 (2003).
14. G.-X. Qian, R. M. Martin, and D. J. Chadi, *Phys. Rev. Lett.* **60**, 1962 (1988).

Chapter VI

Conclusions and Future Work

As the length scale of devices continues to decrease, it becomes increasingly important to understand the fundamental physics governing surface interactions. This work examines the role of strain in the stability of alloyed surface reconstructions utilizing the III-V semiconductors as a model system for any covalently bonded system that exhibits a surface reconstruction. This chapter will summarize the major findings of this work, draw conclusions, and suggest future work to expand upon the findings presented here.

The mixed cation alloy $In_{0.27}Ga_{0.73}As/GaAs$ exhibits a coexistence of a two reconstructions, a (4x3) reconstruction and the z(4x4) reconstruction. The (4x3) reconstruction is new, and it is unique to the alloy system. The z(4x4) reconstruction is an ordering of the α2(2x4) reconstruction and isalso unique to the alloy. The ordering of the α2(2x4) was examined using DFT and was found to be stabilized by atomic size mismatch strain. The In atoms are 7% larger than the Ga atoms which results in a high compressive strain along the $[1\bar{1}0]$ unless the In atoms alternate, occupying positions on opposite sides of adjacent unit cells. Placement of the In in the 3-fold coordinated position of the cation-cation backbond opposite to the surface anion dimer further lowers the unit cell energy by relieving the tensile strain within the bond. Thus the alternating of In atoms in adjacent unit cells induces an alternating anion dimer configuration. This is in agreement with experimental evidence. The α2(2x4) reconstruction is common

to both the InAs and GaAs constituents of the alloy, but the ordering is only seen in the alloy system where the dimer alternates position with an 80% incidence.

The mixed anon alloy GaSb/GaAs exhibits multiple surface structures depending on growth conditions including a mixed (4x3)-(2x4) reconstruction and a (2x8) surface reconstruction. Both of these surface structures are stabilized by the lattice mismatch strain between the substrate and film. The (2x8) reconstruction is obtained experimentally under very Sb rich conditions and is terminated by a double layer of Sb. Four proposed (2x8) atomic structures were analyzed using DFT and the stable structure was determined to be the α(2x8) reconstruction, a variation on the β(2x8) reconstruction proposed for the InSb-(2x8) reconstruction [1]. The mixed α(4x3)-α2(2x4) surface reconstruction has not been previously reported for this system. It consists of 2D islands and terraces where the terrace center is composed of the α2(2x4) reconstruction common to GaAs and the step edges are composed of the α(4x3) reconstruction common to homoepitaxially grown GaSb. Elastic relaxation of the lattice parameter at the islands and terrace edges results in this 2D coexistence. The surface is robust across characterized film thicknesses and a surface incorporation model of atoms into the reconstruction and the role of Ga in the transformation between the α2(2x4) and α(4x3) has been examined.

Further analysis within the GaSb/GaAs system has demonstrated that the surface reconstruction has a dramatic impact on surface topography and defect insertion. Two samples grown under the same growth conditions but on different initial surface reconstructions result in a surface with large QDs surrounded by smaller islands of different shape and density. The resulting defect structures are also dramatically different with the sample grown on the (2x4) reconstruction demonstrating a stacking fault and misfit dislocation array while the sample grown on the (2x8) reconstruction resulted in a tilt boundary and unevenly spaced dislocations. DFT analysis demonstrates a strong interaction between the strain fields a surface reconstruction and a dislocation. The dislocation is shown to sit preferentially at the edge of the trench dimer adjacent to a surface anion dimer. This is due to the fact that the surface anion

dimer can displace slightly in the direction of the trench, relieving some of the strain due induced by the presence of the dislocation.

Some global conclusions can be drawn by comparing the surfaces of the mixed cation and mixed anion alloying systems examined within this dissertation. In both cases, a coexistence of two surface reconstructions can be obtained under a range of growth conditions. The fact that the coexisting reconstructions are stable and reproducible over a range of conditions suggests that this is a thermodynamic minimum rather than a metastable state. In binary, homoepitaxially grown films, the surface reconstruction consists of a single surface reconstruction across the entire surface of the film. The presence of multiple surface reconstructions in both of these systems demonstrates that it is not unique to a single alloy. It also suggests that reconstruction coexistence may be present across many alloy systems – both alloy films such as InGaAs/GaAs and alloy interfaces such as the GaSb/GaAs – due to the effects of elastic relaxation. Previous work on reconstruction coexistence show that coexistence is due to a combination of competing interactions including elastic relaxation at boundary edges [2, 3]. The work in GaSb/GaAs definitively shows that, in this case, elastic relaxation results in two lattice parameter domains within a single island resulting in two stable reconstructions on the surface. In the InGaAs/GaAs case, the results are not as clear due to uncertainty about the atomic structure of the (4x3) reconstruction, but the shifts in stability due to atomic size mismatch strain and lattice mismatch strain suggest that in this case, also, elastic relaxation will play a role in the stabilization of this reconstruction coexistence.

Some further work remains in order to fully understand surface reconstruction coexistence and the impact of the surface reconstruction on subsequent film growth. In the case of the (4x3) reconstruction in InGaAs, the atomic structure must still be determined. Both atomic size mismatch strain and lattice mismatch strain have been shown to affect the relative energies of the (4x3) reconstructions, however neither has resulted in stabilization of the proposed (4x3) reconstructions. Simulated STM images suggest that the stable reconstruction is similar to the proposed Mixed Dimer model. Further examination of the interaction of different alloying sites utilizing a method such

as Monte Carlo may elucidate specific atomic interactions which will explain the stability of this surface reconstruction. Further examination of different (nx3) unit cells is recommended due to the disordered nature of the (4x3) reconstruction, which may in fact be a combination of multiple (nx3) unit cells. A combination of DFT and Monte Carlo studies combining different (nx3) cells will explore the role of long-range order and disorder on this atomic structure. Once the atomic structure of the (4x3) is determined, a deeper understanding of reconstruction coexistence can be obtained by determining the thermodynamic factors in the coexistence equation developed by Tromp and revised by Sears [2, 3]. Little is known about boundary energies between reconstructions, and analysis of the energy of the two coexisting reconstructions vs. lattice parameter would lead to a deeper knowledge of the role of elastic relaxation in surface reconstruction coexistence.

The surface reconstructions which are experimentally reported for GaSb/GaAs, such as the (2x8) and the α(4x3)-α2(2x4), are now well understood. The results presented here demonstrate that there is a definite interaction between the surface reconstruction and the resulting film topography and defect structure but a more detailed understanding remains necessary. There remain inconsistencies between experiments presented here and those presented by different research groups [4, 5] that must be resolved. Further experiments should focus on using RHEED to optimize the growth conditions of free-mounted and In-mounted samples. In this way, a comparison could be developed between the MOS strain relaxation data and the exact surface reconstruction according to STM at any point during the film growth. This would be further correlated with additional TEM analysis of defects in order to develop a complete picture of the initial nucleation and development of defects within the system. Further computational work is also necessary in order to examine the effect of placing the defect at 16 atomic positions rather than 8. This defect placement more accurately represents the stress state seen experimentally. Examination of the energy change as the relative distance between the defect and GaSb/GaAs interface is altered will elucidate whether a wetting layer remains on the surface. Examination of the energy change as the relative distance between the dislocation and the surface reconstruction is altered may result in a more

physical surface where the bonds of atoms directly above the defect are not deformed to the extent that they are in this analysis. Understanding the energy change as the relative distance between the surface reconstruction, defect, and interface is altered will lead to a deeper understanding of *when* the dislocation is nucleated. This in turn would lead to a better knowledge of dislocation insertion in covalent crystals.

Overall, this work demonstrates the complexity of the alloy surface reconstructions. Previous work has demonstrated the importance of alloying on the surface in the development of bulk atomic ordering. This is the first work that examines the importance of alloying on the stability of the surface structure. It has done so by closely coupling experimental and computational research. The impacts of both atomic size mismatch strain and lattice mismatch strain have been examined and shown to dramatically impact the stability of surface reconstructions in III-V semiconductor systems. Further, the interactions between surface reconstructions and defects have been demonstrated and the effects of the surface structure on the surface topography and defect nucleation have been demonstrated. The results shown here will ultimately lead towards a deeper understanding of surface reconstructions in alloyed systems and even to the engineering of specific surface reconstructions which may result in more abrupt interfaces and inject specific types of defects for better device performance, or act as starting surfaces for self-assembly.

i. References

1. W. Barvosa-Carter, F. Grosse, J. H. G. Owen, and J. J. Zinck, *Mat. Res. Soc. Symp. Proc.* 692, H8.4 (2002).
2. L. E. Sears, J. M. Millunchick, and C. Pearson, *J. Vac. Sci. Techol. B* 26, 1948 (2008).
3. R. M. Tromp, and J. B. Hannon, *Surf. Rev. and Lett.* 9, 1565 (2002).
4. G. Balakrishnan, T. J. Rotter, A. Jallipalli, L. R. Dawson, and D. L. Huffaker, *Solid State Lasers XVII: Tech. and Devices* 6871, 87111 (2008).
5. W. Qian, M. Skowronski, R. Kaspi, M. De Graef, and V. P. Dravid, *J. Appl. Phys.* 81, 7268 (1997).

Appendix A

Simulation of STM Images

This is a walk through of how to simulate STM images using VASP on the thunderbird supercomputer at Sandia National Labs and the plotted using gnuplot. Many of the steps can be altered for a different computer or plotting program.

(1) Relax the slab as for a normal relaxation run and save the WAVECAR file.

(2) Generate the PARCHG file.

The PARCHG file describes the partial density of states. For simulated STM images a PARCHG must be generated for both the empty state and filled state images.

Resubmit the slab using using a modified INCAR

#LWAVE=.TRUE.
ISTART = 1
LPARD = .TRUE.
EINT = 1 (for empty state images, -1 for filled state)
*This is how far from the Fermi energy the integration takes place. I've used 1 for the most part, but higher values can be used for higher "voltages".
NBMOD = -3

Note: Be sure to use the same number of nodes to get the PARCHG as you used to get the original WAVECAR.

The PARCHG can be generated by submitting as normal, but it can also be generated by running as an interactive job. This is preferable as this job is rather quick.

On tbird:

qsub –A HertID –l nodes=16:ppn=2,walltime=4:00:00 –I

Mine is: FY092674 (090206)

You should see something like this. You might have to wait a little:

```
----------------------
Submitting job under project/task: 68239/01.10

qsub: waiting for job 54663.sadmin2 to start
qsub: job 54663.sadmin2 ready

NWCC Torque Scheduling System
Job Id: 54663.sadmin2
Username: jebicke

Setting up env for service node
--------------------

Then to run use:
mpiexec ./v46_mpi >output &
```

(3) Use a PERL code to generate isosurfaces

Code modified from original code by Ryan Wixom to analyze constant height slices in a CHGCAR file.

This code will generate isosurfaces, i.e. constant currant surfaces.

To run, use command:

./stm-images.pl V C C C C (as many as desired) X Y

V = position of vacuum in height.

Choose a vacuum between the H and the surface
Number of slices = 140 so choose V ~ 100 or so… Can check a few values to be sure you're comfortably in the vacuum.

C = current, = isosurface value

X = repetitions in the x-dir for the stm

Y = repetitions in the y-dir for the stm

IsoSurfaceCode:

```
\eval '(exit $?0)' && eval 'exec perl -S $0 ${1+"$@"}' && eval 'exec
perl -S $0 $argv:q' if 0;
#;-*- CPerl -*-

#  A script for processing PARCHG files
#  ~:crystal2cm.pl <list of z values>
#  The input z values are a number from the grid 0..NXZ ?
#  the output files are in gnuplot's pm3d format

@args=@ARGV;
@args>=1 || die "./crystal2cm.pl <list of z values>";
$vaccuum = shift @args;
```

```
$yrep = pop @args;
$xrep = pop @args;
print "\n";
print "For a vacuum beginning at slice = ";
print "$vaccuum\n";
print "I will output constant currant slices for ";
foreach $a (@args) {print "$a, ";}
print "\n";
print "And I will repeat the slab $xrep in the x-dir and $yrep in the
y-dir\n";

open (IN,"PARCHG");
@data=<IN>;
close (IN);

#$line = $data[0];
#$line =~ s/^\s+//;
#@broken = split(/\s+/,$line);
#$num_atoms = $broken[0];

#print "@broken\n";
#print "$num_atoms\n";

#Get the lattice vectors
$line=$data[2];
$line=~s/^\s+//;
@broken = split(/\s\s+/,$line);
$xvec1 = $broken[0];
$xvec2 = $broken[1];
$xvec3 = $broken[2];
$xvec = sqrt($xvec1**2 + $xvec2**2 + $xvec3**2);

$line=$data[3];
$line=~s/^\s+//;
@broken = split(/\s\s+/,$line);
$yvec1 = $broken[0];
$yvec2 = $broken[1];
$yvec3 = $broken[2];
$yvec = sqrt($yvec1**2 + $yvec2**2 + $yvec3**2);

$line=$data[4];
$line=~s/^\s+//;
@broken = split(/\s\s+/,$line);
$zvec1 = $broken[0];
$zvec2 = $broken[1];
$zvec3 = $broken[2];
$zvec = sqrt($zvec1**2 + $zvec2**2 + $zvec3**2);

$volume = $xvec * $yvec * $zvec;
```

```
print "The x vector is $xvec1 $xvec2 $xvec3 => $xvec\n";
print "The y vector is $yvec1 $yvec2 $yvec3 => $yvec\n";
print "The z vector is $zvec1 $zvec2 $zvec3 => $zvec\n";
print "The cell volume is $volume Angstroms\n\n";

#Get the number of atoms
$line = $data[5];
$line =~s/^\s+//;
@broken = split(/\s\s+/,$line);
$num_atoms = $broken[0]+$broken[1]+$broken[2]+$broken[3];
print "0-$broken[0] 1-$broken[1] 2-$broken[2] 3-$broken[3]\n";

#find the line with the grid dimensions
$row = $num_atoms+3+5;
$line = $data[$row];
$line =~s/^\s+//;
@broken = split(/\s\s+/,$line);
$gridx = $broken[0];
$gridy = $broken[1];
$gridz = $broken[2];
print "Grid is: $broken[0] x $broken[1] x $broken[2]\n";

#Read in the raw data into one long array
$row = $row+1;
for ($i=$row;$i<=$#data;$i++) {
  @line=split(/\s+/,$data[$i]);
  for ($j=1;$j<=$#line;$j++) {
    push(@raw,$line[$j]);
  }
}

#print "$raw[0] $raw[$#raw]\n";
#Split the array into the volume data (can divide by $volume if
want e-/A^3)
$i=0;
foreach $z (0..$gridz-1) {
  foreach $y (0..$gridy-1) {
    foreach $x (0..$gridx-1) {
      $density[$x][$y][$z] = $raw[$i];
      #print "$x $y $z: $raw[$i]\n";
      $i++;
    }
  }
}

#print "test: $density[83][41][149]\n";

foreach $current (@args)
```

```
{
   #print a 2d slice
   open(OUT,">chg$current.dat");

   foreach $m (1..$xrep)
   {
        foreach $x (0..$gridx-1)
        {
           foreach $n (1..$yrep)
           {
                foreach $y (0..$gridy-1)
                {
                   $z = $vaccuum;
                   while ($z>=0)
                   {
                        #print OUT "$x $y $z $density[$x][$y][$z]\n";
                        #$z--;

                        if ($density[$x][$y][$z] > $current)
                        {
                           $xtemp=$x*$xvec/$gridx+($m-1)*$xvec;
                           $ytemp=$y*$yvec/$gridy+($n-1)*$yvec;
                           $ztemp=$z*$zvec/$gridz;
                           print OUT "$xtemp $ytemp $ztemp\n";
                           $z=-1;
                        }
                        elsif ($z == 0)
                        {
                           $xtemp=$x*$xvec/$gridx+$m*$xvec;
                           $ytemp=$y*$yvec/$gridy+$n*$yvec;
                           print OUT "$xtemp $ytemp 0\n";
                           $z = -1;
                        }
                        else
                        {
                           $z--;
                        }
                   }
                }
           }
           print OUT "\n";
        }
   }
   close(OUT);
}
```

(4) Plot STM images using gnuplot

Note, some commands and shortcuts vary for different versions of gnuplot and different terminals.

General plot details are stored in ‘plot_stm.txt’ (see below).
To plot:

load ‘plot_stm.txt’
splot ‘file’
set title “”
set xrange [x1:x2]
etc.

Some gnuplot shortcuts.

\201 = Å
\265 = m
\242 = degree
\247 = kinda beta
\255 = does not equal
\260 = infinity
\261 = p/m
\262, 263 = greater and equal
\266 = del
\267 = Sigma
\270 = cap pi
\271 = pi
\275 = omega

plot_stm.txt

```
#!/sw/bin/gnuplot -persist
# set terminal aqua
# set output
set term aqua
unset clip points
set clip one
unset clip two
set bar 1.000000
set border 31 lt -1 lw 1.000
set xdata
set ydata
set zdata
set x2data
set y2data
set boxwidth
set style fill empty border
set dummy x,y
set format x "% g"
set format y "% g"
set format x2 "% g"
set format y2 "% g"
set format z "% g"
set angles radians
unset grid
```

```
set key title ""
set key right top Right noreverse enhanced box linetype -2
linewidth 1.000 samplen 4 spacing 1 width 0 height 0 autotitles
unset label
unset arrow
unset style line
unset style arrow
unset logscale
set offsets 0, 0, 0, 0
set pointsize 1
set encoding default
unset polar
unset parametric
unset decimalsign
set view map
set samples 100, 100
unset surface
unset contour
set clabel '%8.3g'
set mapping cartesian
set datafile separator whitespace
unset hidden3d
set cntrparam order 4
set cntrparam linear
set cntrparam levels auto 5
set cntrparam points 5
set size ratio 0 1,1
set origin 0,0
set style data pm3d
set style function pm3d
set xzeroaxis lt -2 lw 1.000
set yzeroaxis lt -2 lw 1.000
set x2zeroaxis lt -2 lw 1.000
set y2zeroaxis lt -2 lw 1.000
set tics in
set ticslevel 0.5
set ticscale 1 0.5
set mxtics default
set mytics default
set mztics default
set mx2tics default
set my2tics default
set mcbtics default
set xtics border mirror norotate autofreq
set ytics border mirror norotate autofreq
set ztics border nomirror norotate autofreq
set nox2tics
set noy2tics
set cbtics border mirror norotate autofreq
```

```
set title "Partial Charge Plot" 0.000000,0.000000  font ",30"
set timestamp "" bottom norotate 0.000000,0.000000  ""
set rrange [ * : * ] noreverse nowriteback  # (currently
[0.00000:10.0000] )
set trange [ * : * ] noreverse nowriteback  # (currently [-
5.00000:5.00000] )
set urange [ * : * ] noreverse nowriteback  # (currently [-
5.00000:5.00000] )
set vrange [ * : * ] noreverse nowriteback  # (currently [-
5.00000:5.00000] )
set timefmt x "%d/%m/%y,%H:%M"
set timefmt y "%d/%m/%y,%H:%M"
set timefmt z "%d/%m/%y,%H:%M"
set timefmt x2 "%d/%m/%y,%H:%M"
set timefmt y2 "%d/%m/%y,%H:%M"
set timefmt cb "%d/%m/%y,%H:%M"
set x2label "" 0.000000,0.000000  font ""
set xrange [ 0.00000 : 83.0000 ] noreverse nowriteback
set x2range [ * : * ] noreverse nowriteback  # (currently [-
10.0000:10.0000] )
set y2label "" 0.000000,0.000000  font ""
set yrange [ 0.00000 : 41.0000 ] noreverse nowriteback
set y2range [ * : * ] reverse nowriteback  # (currently [-
10.0000:10.0000] )
set zlabel "" 0.000000,0.000000  font ""
set zrange [ 0.00000 : 60.0000 ] noreverse nowriteback
set cblabel "" 0.500000,0.000000  font ",18"
set cbrange [ * : * ] noreverse nowriteback  # (currently [-
10.0000:10.0000] )
set zero 1e-08
set lmargin -1
set bmargin -1
set rmargin -1
set tmargin -1
set locale "C"
set pm3d at b
set pm3d scansautomatic flush begin noftriangles nohidden3d
transparent implicit corners2color mean
set palette positive nops_allcF maxcolors 0 gamma 1.5 color model
RGB
set palette rgbformulae 7, 5, 15
set colorbox default
set colorbox vertical origin 0.9,0.2 size 0.1,0.63 bdefault
set loadpath
set fontpath
set fit noerrorvariables
set autoscale x
set autoscale y
set autoscale z
```

```
set xlabel "[110] direction (\201)" 0.0,0.0 font",25"
set ylabel "[1-10] direction (\201)" 0.0,0.0 font",25"
set label "Height (\201)" font ",25" at graph 1.01, graph 0.05
set palette rgbformulae 7,5,0
#splot "chg66.dat"
#    EOF
```